TRANSPORT AND DIFFUSION ON THE SOUTHWESTERN PUERTO RICAN SHELF

SOTIRIS KIOROGLOU

TRANSPORT AND DIFFUSION ON THE SOUTHWESTERN PUERTO RICAN SHELF

by

©Sotiris Kioroglou

A Thesis submitted to the School of Graduate Studies
in partial fulfillment of the requirements
for the degree of Master of Science

Department of Physics
Memorial University of Newfoundland
June 29, 1992

St John's Newfoundland

ISBN 0-315-86672-1

Canada

I would like to dedicate this work to really patient graduate students who try to discover themselves and the meaning of life. I believe it is most important that they become supervisors of themselves before they become supervisors of others, as is unfortunately not always true.

Acknowledgements

I would like to thank my supervisor Dr Brian Sanderson for providing me the opportunity to work on an exciting project in the Carribbean. I would like to thank him for his financial support and his guidance. Great thanks to Mrs Jo Barron for her crucial encouragement during very difficult times of my project. I would also like to thank Marine Biologists of the University of Puerto Rico, Dr Douglas Shapiro, Dr Danny Hensley, and Dr Richard Appeldorn, for their financial assistance, help and encouragement during my field work at Puerto Rico. Great thanks also to all the Graduate students of the University of Puerto Rico, and to the staff of Isla Magueyes who helped substantially in the completion of my field work. I would also like to sincerely thank Allan Goulding, the Computer Scientist of the Physical Oceanography team, who helped me so much on my software problems. Finally I would also like to thank all my Instructors at Memorial, and all the reviewers of my Thesis.

ABSTRACT

In 1988 and 1989 drifter tracking experiments were conducted on the Southwestern Puerto Rican shelf. Surface drifters were used as surrogates for buoyant fish eggs, in order to determine the dependence of the egg trajectory on the spawning site and time. Data analysis of the drifters shows that the mean trajectory depends on the spawning time and the season of drifter release. Trajectories from adjacent spawning and nonspawning sites have no significant difference, however. Both the current and the wind tend to have an along-shore and westward direction. The high correlation between wind and current indicates that the wind drives the current in a direction parallel to the shore. Flow reversals (to the East) are common in periods of light winds, which occur most frequently in the wet season, from July to December. The data analysis agrees with the hypothesis that the flow reversals might be caused by an eastward pressure gradient opposing the wind. The predominant tidal harmonics on the reef are the diurnal K1 and the semidiurnal M2, that can be modelled as across-shelf standing waves. Scale analysis showed that the associated velocity amplitudes are insignificant on the reef. The seiche of occuring on the reef, is important for the currents in the area.

The flow is highly variable, especially in the along-shore direction. The flow variability can be modelled as a random walk for the cross-shore component. Statistical analysis of motion relative to the cluster centroid, indicates that a patch of drifters is elongated in a direction parallel to the coastline at all the times. This indicates that the horizontal shearing of the mean flow velocity plays a dominant role in the relative diffusion processes of the area. The data analysis also indicates that there is much more variability in the paths of the clusters, than in the paths of the drifters within a cluster.

Table of Contents

List of Figures

(approximately). The coast and the coral reefs are shaded. The positive x axis points towards the East (approximately), and the positive y axis points towards the North (approximately).

List of Tables

Chapter 1

Introduction

1.1. Physical and biological objectives

In the years 1988 and 1989, Lagrangian drifter tracking experiments were conducted on the Southwestern Puerto Rican shelf. The study had both biological and physical objectives. With regard to the physical aspect, it was the study of how the variability of diffusion and transport of particles on a reef depends on the position and time of the particles' release in the sea. From the biological viewpoint, we sought to interpret the spawning strategy followed by the reef dwelling fish *Thalassoma Bifasciatum*. The fish spawns clouds of positively buoyant eggs near the bottom substrate. It spawns only at midday, at specific sites of the reef. The biological question was whether or not these spawning sites and this spawning time results in more fish eggs surviving than if the fish were to spawn at different sites or times. Egg mortality can be caused by predation from reef-associated fishes and invertebrates (Shapiro et al., 1988). In order to avoid predation, the eggs must avoid trajectories in shallow water, and should disperse quickly.

1.2. Egg-Transport and Diffusion.

When a small patch of particles is released in the sea, they are usually subjected to a flow field that causes both an advective transport of the patch and a relative motion between particles in the patch. The transport is caused by the spatially averaged component of the flow field and can be deterministic (steady or oscillatory flows), nondeterministic, or a mixture of both. If the

transport is variable with time, it might result in the "meandering" (spatial undulation) of the patch trajectory. The relative motion of particles in the ocean is usually regarded as being nondeterministic. This however is not always the case. For example, the relative motion between the particles in a patch can be approximately deterministic if the patch is subjected to a steady but nonuniform flow field. Relative motion, whether deterministic or not, leads to the patch dispersal in space When the random movements are microscopic, then this dispersal is called molecular diffusion. When the random motions are caused by turbulent eddies, then we refer to dispersion as eddy diffusion. The eddies are fluid domains, within which, for some time interval τ' (eddy-lifetime) and over some eddy length scale l, velocity is coherent. This definition can be extended to any other kinematic properties such as vorticity, or deformation rates (Tennekes and Lumley, 1972). In a three-dimensional flow field, the smallest time and space scales are determined by the ability of molecular viscosity to smooth out small scale shears, at the rate at which they are being created by an energy cascade from the large to small scales, and are called the Kolmogorov time and space scales.

Any shear, rotation or divergence in the flow field can distort the cluster, rotate the cluster or change the cluster area. Shears in the deterministic flow interact with the random kinematics causing the enhancement of dispersal through the "shear diffusion effect" (Bowden, 1965, Sanderson and Okubo, 1987). It should be noted that the division between the eddy diffusion and the transport for the motion of a patch in a turbulent field would depend on the spatial scale of a patch (Csanady, 1973). The eddies of a size smaller than hat of the patch will have a different kinematic effect on each particle of the patch, and this results in the dispersal of the particles with respect to the patch centroid, whereas eddies of a scale that is much larger than that of the patch, will induce the same motion to all the patch units, and in this sense, these larger eddies should be regarded as part of the transport. As time progresses

however, the patch grows in size, and this division of the spectrum of the eddies into the transport and diffusion domains tends to bigger wavelengths and lower frequencies (Okubo and Ebbesmeyer, 1976).

Commonly diffusion experiments are done by either releasing a patch of particles instantaneously over a small area (instantaneous source) or by continuously releasing particles over a small area (continuous release). If the initial patch dimensions are very small compared to the patch dimensions at later times, experiments will approximate a point source release.

There are two different methods for measuring and two coordinate systems for describing the flow field, the Eulerian and the Lagrangian. In the Eulerian approach, one regards the velocity $\vec{u}_E(x,y,z,t)$ as a function of fixed space coordinates x,y,z and time t. A common Eulerian instrument that measures flow velocity in the ocean is the moored current meter. In the Lagrangian approach one regards the velocity $\vec{u}_L(a,b,c,t)$ of a particle that moves with the fluid, as a function of time t since some initial time t_0 when the particle position is (a,b,c), where $(x,y,z)=(a,b,c)$ at $t=t_0$. Tracking of drifters is a common Lagrangian method for measuring oceanic velocities. Eulerian and Lagrangian coordinates provide two ways of describing the same velocity field. The Eulerian and Lagrangian velocities are interrelated by the Euler-Lagrange transformation (Zimmerman, 1978), that is

$$\vec{u}_L(\vec{a},t)=\vec{u}_E\left(\vec{a}+\int_0^t \vec{u}_L(\vec{a},t')dt',t\right).$$

This is a nonlinear vector integral equation. In a turbulent flow field there is no hope of solving it analytically. Numerical techniques of solution would require that many measurements of $\vec{u}_E$ be made to calculate the trajectory of just one particle. Similarly the trajectories of many particles must be measured to obtain the Eulerian flow field as a function of time in even one position x.

Oceanic velocity fields are spatially and temporally variable. This variability

is usually modeled stochastically (Stommel, 1948). In either the Eulerian or the Lagrangian coordinate system, the usual way of determining the statistics of the velocity field consists of two steps. First, the evaluation of the first statistical moment of the velocity (mean motion), using a way of averaging which is pertinent to the problem. And second, the extraction of this mean (first done by Reynolds, 1895) and also of any other deterministic component, out of the velocity time series, to determine the turbulent fluctuations which are then fitted to stochastic models. We will use the following methods (Okubo, 1962) of averaging for estimating the first statistical moment of the drifter trajectories and velocities, on the Puerto Rican reef.

1: Cluster (or Patch) average. This is related to a cluster of drifters, that were all released at some initial time t_0. It is the averaging at some time t since release time, over all the drifters of the cluster. This is equivalent to averaging over the space $\Psi = \{\vec{a}\}$ that encompasses the Lagrangian coordinates of the drifters in the cluster.

2: Time average. This is the averaging of a drifter related quantity over some time period.

3: Ensemble average. This is the averaging over many experiments that are the same in a statistical sense. Assuming homogeneous and stationary statistics, the ensemble can be comprised of releases at different times and different places.

The above averaging modes depend on the length of the time series T, or the space Ψ averaged over.

1.2.1. The diffusion equation

Molecular diffusion obeys Fick's law so that if there is a concentration gradient ∇C there will also be a net molecular flux $\vec{g}$ down this gradient. The flux is given by

$$\vec{g} = -D\nabla C \ . \tag{1.1}$$

where D is a constant diffusion coefficient, that is a characteristic property of the fluid. Let us ignore all the macroscopic motion. The change of C within some elemental volume will be dependent upon the difference between the molecular flux (1.1) into that elemental volume and the molecular flux out of that elemental volume. Taking the limit that the volume is infinitesimal we obtain

$$\frac{\partial C}{\partial t} = -\nabla \cdot \vec{g} \ . \tag{1.2}$$

Substituting (1.1) into (1.2), gives the diffusion equation.

$$\frac{\partial C}{\partial t} = D\nabla^2 C \ . \tag{1.3}$$

Equation (1.3) can also be derived from a random walk. Consider a big number of particles, executing one-dimensional random steps of length λ over a time interval τ. Then the probability $p(x,t+\tau)$, that a particle is at the position x at time $t+\tau$, is given by

$$p(x,t+\tau) = \frac{1}{2}\left[p(x-\lambda,t) + p(x+\lambda,t)\right] \ . \tag{1.4}$$

Assuming that $\lambda \ll |x|$, and $\tau \ll t$, we can apply Taylor expansions for all the terms of (1.4), with respect to either t (left hand side term), or x (right hand side terms). This transforms (1.4) as follows.

$$\frac{\partial p}{\partial t} + \frac{\tau}{2}\frac{\partial^2 p}{\partial t^2} = \frac{\lambda^2}{2\tau}\frac{\partial^2 p}{\partial x^2} + \cdots O\left(\frac{\lambda^4}{\tau}\right) \ . \tag{1.5}$$

In the limit of very small time and space steps such that

$$\lim_{\tau,\lambda \to 0} \frac{\lambda^2}{2\tau} = D \ , \tag{1.6}$$

where D is constant, (1.5) tends to the diffusion equation.

$$\frac{\partial p}{\partial t}=D\frac{\partial^2 p}{\partial x^2}\ , \tag{1.7}$$

where D is a diffusivity. We now see that D can be interpreted in terms of λ, τ or $u=\lambda/\tau$ and λ, i.e., in terms of molecular motion, which is a property of the fluid and its state.

Equation (1.7) has, for an instantaneous point release (i.e., for $p(x,0)=\delta(x)$, where $\delta(x)$ is the delta function) the following solution (Okubo, 1962; p304).

$$p(x,t)=\frac{1}{\sqrt{4\pi Dt}}e^{-\frac{x^2}{4Dt}}\ . \tag{1.8}$$

This is a Gaussian probability function, with variance $\sigma^2=2Dt$. This indicates that in the diffusion limit (1.6) the variance of a cloud of diffusing material increases proportional to time.

In turbulent flows the diffusion limit may not be applicable and the dispersion of particles becomes a function of the flow field rather than a function of the fluid. Taylor's theory (1922) relates diffusion in stationary and homogeneous turbulent fields to the properties of turbulent motion. Consider an ensemble of instantaneous particle releases from a point, in such a one dimensional stationary and homogeneous turbulent field, that has no mean flow. One can express the position $x=x(t)$ of a particle at time t from its release, in terms of the particle velocity $u=u(t')$ at all previous times t' of the particle trajectory.

$$x(t)=\int_0^t u(t')dt'\ .$$

This implies that, at time t, the average (over the ensemble of the particles) rate of dispersion is

$$\frac{d\langle [x(t)]^2\rangle}{dt}=2\int_0^t \langle u(t)u(t')\rangle\, dt'\ . \tag{1.9}$$

where $\langle\ \rangle$ denotes the average over the ensemble of the particles. The velocity $u(t)$ was taken inside the integral since it is independent of t'. Introducing the variable $\tau=t-t'$ in equation (1.9), we derive

$$\frac{d\langle [x(t)]^2\rangle}{dt} = 2\int_0^t \langle u(t)u(t-\tau)\rangle\, d\tau = 2\langle |u(t)|^2\rangle \int_0^t R(\tau,t)d\tau \ . \tag{1.10}$$

where $R(\tau,t)$ is the autocorrelation function of the particle velocity, that is

$$R(\tau,t) = \frac{\langle u(t)u(t-\tau)\rangle}{\langle |u(t)|^2\rangle} \ . \tag{1.11}$$

Integrating (1.10) with respect to time and using the stationarity hypothesis, i.e., that average quantities over the ensemble of particles are independent of time, (for example, $R(\tau,t)=R(\tau)$) we derive the following expression for the variance.

$$\langle x^2\rangle = 2\langle u^2\rangle \int_0^t \int_0^{t'} R(\tau)\, d\tau\, dt' \ . \tag{1.12}$$

Wave motion will cause $R(\tau)$ to oscillate as τ increases. On the other hand we normally think of turbulent eddies as having random velocities that decorrelate as time progresses, so that $R(\tau)$ decreases as the lag time τ increases. If the integral $\int_0^t R(\tau)d\tau$ converges to an "integral time scale" τ^* as t tends to infinity, then, on the average, the velocity of the particle at a time t becomes completely uncorrelated with its velocity at $t+\tau$ if $\tau \gg \tau^*$. This implies that for times much larger than τ^*, diffusive particle motion can be treated as an uncorrelated random walk, and (1.12) becomes

$$\langle x^2\rangle = 2\langle u^2\rangle \tau^* t \ . \tag{1.13}$$

and by analogy with molecular diffusion, we obtain an "effective eddy diffusivity" K for the turbulent diffusion as follows

$$K = \frac{1}{2}\frac{d\langle x^2\rangle}{dt} = \langle u^2\rangle \tau^* \ . \tag{1.14}$$

The corresponding turbulent diffusion equation would then be

$$\frac{\partial C}{\partial t} = K\frac{\partial^2 C}{\partial x^2} \ , \tag{1.15}$$

in analogy to the molecular-random walk diffusion equation (1.7) (note that $K \gg D$ usually).

Stommel (1948) showed that, if the Fickian diffusion equation (1.15) were to describe the turbulent oceanic motion, then the probable change in separation between two particles floating in the ocean, would not depend upon the separation itself, something which is in contrast with the observations. He mentioned that the reason for the failure of the Fickian model to describe the turbulent diffusion, is that, as the separation of two particles increases, bigger and bigger eddies would contribute to diffusion, thereby increasing the eddy diffusivity. Richardson (1926) introduced the concept of the "neighbour concentration", $q(r)$, of pairs of particles with "neighbour separation" equal to r. He then postulated the following diffusion equation

$$\frac{\partial q}{\partial t}=\frac{\partial}{\partial r}\left|F(r)\frac{\partial q}{\partial r}\right|, \tag{1.16}$$

which is analogous to the Fickian equation (1.15), but with the neighbour separation replacing the position as an independent variable. In this equation, $F(r)$ is a "neighbour diffusivity". Richardson used a large number of atmospheric observations, to show that

$$F(r)=c_1 r^{4/3}, \tag{1.17}$$

where c_1 is a constant. This equation is referred to in literature as the ***4/3 power law***. Okubo (1971) similarly showed that patch diffusion is dependent on patch size. He also showed that the variance of patch dimensions grew much faster than t, at a rate $t^{2.3}$. Recently Sanderson and Booth (1991) measured the fractal dimension of drifter trajectories to be about 1.3. Thus a fractional Brownian motion with this dimension results in variance growing proportional to $t^{1.5}$. This is faster than ordinary Brownian motion that has fractal dimension 2 and results in variance growing proportional to t. To account for variance of relative positions growing faster than $t^{1.5}$ Sanderson and Booth (1991) postulate an accelerated fractional Brownian motion model. In this model, the relative velocity tends to increase with increasing separation. A fractional Brownian motion is a random walk that has fractal dimension (see Baker and Gollub, 1990; p:111-120 for the definition of fractal dimension and also Mandelbrot and

Van Ness, 1968, for a more detailed definition of the fractional Brownian motion).

1.2.2. Horizontal shear dispersion

Let us examine the dispersion resulting from the interaction of the horizontal velocity gradients of a spatially varying flow with the isotropic eddy diffusion. Okubo (1966) considers such an interaction, for which the velocity gradients, hereafter symbolized as $\Omega_a=\frac{\partial u}{\partial x}$, $\Omega_b=\frac{\partial u}{\partial y}$, $\Omega_c=\frac{\partial v}{\partial x}$, $\Omega_d=\frac{\partial v}{\partial y}$, are steady and homogeneous. He assumes a division of the eddy spectrum between large scale eddies that cause the velocity gradients, and very small scale eddies that cause an isotropic eddy diffusion.

Let us consider a simplified version of this problem, where a mean flow in the x direction $u=u_0+\Omega_b y$ is sheared in the y direction, i.e., $\Omega_a=\Omega_c=\Omega_d=0$, and $\Omega_b\neq 0$ but is constant and homogeneous. Let there also be a smaller scale turbulent motion that can be characterized as an isotropic eddy diffusivity K. Adding advective terms to the two dimensional version of equation (1.15) the equation describing dispersion of material of concentration C becomes

$$\frac{\partial C}{\partial t}+(u_0+\Omega_b y)\frac{\partial C}{\partial x}=K\left(\frac{\partial^2 C}{\partial x^2}+\frac{\partial^2 C}{\partial y^2}\right). \tag{1.18}$$

If we transform to a coordinate system that moves with the mean flow such that

$x=a+(u_0+\Omega_b y)t$,

$y=b$,

$C(x,y,t)=S(a,b,t)$,

then

$$\frac{\partial C}{\partial t}+(u_0+\Omega_b y)\frac{\partial C}{\partial x}=\frac{\partial S}{\partial t} ,$$

$$\frac{\partial}{\partial x}=\frac{\partial}{\partial a} ,$$

$$\frac{\partial}{\partial y}=\frac{\partial}{\partial b}-\Omega_b t\frac{\partial}{\partial a} ,$$

so that (1.18) becomes

$$\frac{\partial S}{\partial t}=(K+(\Omega_b)^2t^2K)\frac{\partial^2 S}{\partial a^2}-2\Omega_b tK\frac{\partial^2 S}{\partial a\partial b}+K\frac{\partial^2 S}{\partial b^2} . \tag{1.19}$$

Now let us use dimensional analysis to determine the spreading of a point source of material subject to the above diffusivity K and shearing field $(u_0+\Omega_b y)$. We will consider dispersion in an unbounded fluid. In some time t the diffusivity will spread the point source a distance $\Delta Y=\sqrt{Kt}$ in the y direction. Thus the shear field will advect it a distance ΔX in the x direction in this time given by

$$\Delta X=\Delta Y\Omega_b t=\sqrt{Kt}\,\Omega_b t . \tag{1.20}$$

Thus the effective Lagrangian diffusivity K_{ea} in the x direction is

$$K_{ea}=K+\frac{\Delta X^2}{t}=K+K(\Omega_b)^2t^2 ,$$

which is consistent with our earlier equation (1.19). For large t the elongation ε under shear diffusion is

$$\varepsilon=\frac{\Delta X}{\Delta Y}=\frac{\Omega_b t\sqrt{Kt}}{\sqrt{Kt}}=\Omega_b t , \tag{1.21}$$

i.e., it increases proportional to t if Ω_b is a constant. This analysis was performed for the case that there is only one nonnegligible velocity gradient, i.e., Ω_b. We can use the same type of scale analysis for the other velocity gradients too, i.e., for Ω_a, Ω_c, and Ω_d, and derive similar formulas, provided that only one of them is significant, i.e., different than zero, the one under consideration. In reality of course there might be more than one significant velocity gradient in

the flow field, and then the problem cannot be addressed any more with the above simple method, since this method does not consider the possible interaction between different velocity gradients. Okubo (1966) discussed the problem for the case that all velocity gradients are nonnegligible and steady. He formulated this problem in terms of some linear combinations of the velocity gradients, that are also called "differential kinematic properties" and are defined as follows in the literature.

1. The vorticity $\omega=\frac{\partial v}{\partial x}-\frac{\partial u}{\partial y}$ rotates the patch.

2. The shearing deformation $\eta=\frac{\partial v}{\partial x}+\frac{\partial u}{\partial y}$ and the stretching deformation $h=\frac{\partial u}{\partial x}-\frac{\partial v}{\partial y}$ are not independent and depend on the coordinate system's orientation, i.e., it is always possible to rotate the coordinate system, so that the shearing deformation becomes zero (Saucier, 1953). Shearing and stretching deformation result in patch elongation.

3. The divergence $d=\frac{\partial u}{\partial x}+\frac{\partial v}{\partial y}$, which is a measure of the material flux into a closed elemental area. The divergence changes the cluster area A according to $\frac{1}{A}\frac{dA}{dt}=d$.

In particular Okubo (1966) studied the diffusion of a point source in a nondivergent velocity field, characterized by steady vorticity, shearing and stretching deformations, and constant eddy diffusivity. He found that the shape of the patch will be an ellipse at all the times. Especially for the case that the stretching and shearing deformations are much larger than the vorticity, he concluded that the patch tends to elongate in a direction almost parallel to the mean flow, and that the elongation increases with time.

Chapter 2

Experimental methodology

2.1. Experimental objectives

The drifter experiments addressed the biological question mentioned in section 1.1 in a quantitative way (Shapiro et al., 1988). All drifter experiments were initiated on the San Cristobal plateau, a reef that is located at the Southwestern corner of Puerto Rico (Figure 2-1) and has approximate dimensions $300m$ by $200m$ (Figures 2-2, 2-3). The spawning time and spawning sites of *Thalassoma*, on San Cristobal reef, were identified by diving. The spawning occurs in the time interval between $1200h$ and $1400h$ local time. In each experiment, rhodamine-dye patches were simultaneously released at both a "spawning" and a "nonspawning" site (Figure 2-3). The dye patches were visually tracked by a diver. Every $10min$ the diver identified the centers of the two dye patches. He then "marked" each dye center with a buoy. The buoy was floating at the sea surface and was attached with a rope to a weight lying on the bottom. This ensured that the buoy did not drift with the currents. The biologists were based on the buoy positions to plot the dye trajectory. The dye patches were tracked this way until they became either too dilute to be seen with the naked eye, or until they reached the edge of the reef. At this time (usually 1 hour after release), each of the dye patches was replaced with a cluster of 5 drifters. The submerged part of the drifter consisted of 4 aluminum vanes perpendicular to each other, extending over a depth range from $0.4m$ to $1.1m$. The submerged part was attached to a buoy that supported a vertical lamp-stick above the sea surface (Figure 2-4). The drogues were released in such a way that ensured that the area and shape of the dye patch was well

represented by the area and the shape of the cluster of drogues. One drogue was released at the center of the dye patch, and the other four drogues were released in a cross-configuration around the patch. The eggs hatch after about 24 hours. Drifters were tracked for 24 hours using a Del Norte microwave trisponder. The trisponder system consisted of a "master" transceiver on the tracking boat, that communicated with two remote slave transceivers ("remotes") separated by $10\,km$ (Figure 2-2). The "master" consisted of a computer and an antenna that was connected to the computer, and was located at the edge of the boat. Each "remote" consisted of an antenna similar to the "master" antenna. Each of the "remote" antennas were designed to emit a microwave pulse as soon as they received a microwave pulse emitted from the "master". We approached the drogues with the boat, and we tried to ensure that the horizontal distance between the antenna of the "master" transceiver on the tracking boat and the drogue was as small as possible (typically $1\,m$ to $2\,m$). We then used the computer of the "master" transceiver (manual operation) to emit a microwave pulse. The two "ranges" to the "remotes", i.e., the distances from the "master" antenna to the "remote" antennas, were calculated from the time of flight of a microwave pulse from the "master" to the "remotes" and back to the "master". This time of flight of the pulse was measured by the time measuring system of the "master". A "triangulation algorithm" was then used by the computer of the "master" to convert the pair of ranges into x,y coordinates with axes defined so that the remotes lay on the x axis and remote 1 was at $x=0,y=0$. The screen of the "master" computer displayed the x,y coordinates of the "master antenna" and the time when this position occurred. These coordinates and also the time of their occurrence, were recorded as the coordinates and time of the drogue. This whole process was repeated for each of the ten drogues (two clusters). Each of the drogues had a different number on its lamp stick to distinguish it from the other drogues.

The accuracy of the ranges was $\Delta r=1\,m$ according to the manufacturer.

Checking the system against known distances however revealed values of Δr as high as $4m$. This might have happened because the tests were done on land, where the value of Δr becomes sometimes larger due to to the presence of objects that affect the path of the microwave rays. For a given error of the two ranges Δr, the real position x,y could be anywhere within an area that can be approximated by a rhombus, of which the parallel sides are $2\Delta r$ apart (Figure 2-5). The position of the center of this rhombus can be defined as the measured position, or the position fix, and the error of the position fix can be defined as $(\Delta s_1, \Delta s_2)$, where $\Delta s_1, \Delta s_2$ are equal to half the length of the diagonals of the rhombus. From the geometry in Figure 2-5 we see that $(\Delta s_1, \Delta s_2) \approx (\frac{\Delta r}{\sin(\phi/2)}, \frac{\Delta r}{\cos(\phi/2)})$, where ϕ is the angle that the center of rhombus subtends on the "baseline" (the segment joining the positions of the two remotes). The angle that is denoted as $\approx \phi$ in Figure 2-5 is approximately equal to ϕ, since the dimensions of the rhombus are much smaller than lengths of the ranges. From the above formula it is evident that, all the points for which ϕ is constant, have the same error in the position fix. It is also evident that, for very small values of ϕ (corresponding to positions very far from the baseline) Δs_1 is very large, whereas for values of ϕ near 180^0 it is Δs_2 that is very large. The recommended practice by the manufacturer was to keep the values of ϕ in a range such that $30^o \le \phi \le 150^o$, so that $\Delta s_{max} \le \frac{\Delta r}{\sin(15)}$, i.e., $\Delta s_{max} \le 4m$, for $\Delta r = 1m$ (where Δs_{max} is the maximum of Δs_1 and Δs_2). The locations of the two remotes were designed so that most of the drifter fixes result in values of ϕ within the above specified values. The locus of all points having a constant position fix error is the locus of all the points subtending a constant angle ϕ on the baseline. This locus is a circle whose radius (for a given baseline length b) is $r = b/2\sin(0.5\phi)$, and whose center is located at $(b/2, \pm\, b/2\tan(0.5\phi))$, in our working coordinate system. Figure 2-2, shows the positions of the "remotes", marked as "remote" 1 and "remote" 2, and the area within which the error of the position fix is less than $4m$, given that the range error is $1m$. The boundaries of

this area are circular and are the loci of all points subtending angles of 30^{o} and 150^{o} respectively on the baseline.

The position fixes on drifters were obtained at irregularly spaced times. The time interval between two subsequent position fixes of the same drifter ranged from 20 *minutes* to $6h$ on a few occasions, when we had to be very careful in maneuvering the boat in shallow areas that had many coral reefs, or when we lost sight of drifters in strong winds and big waves. The typical time interval between subsequent position fixes of one drifter was $1h$. In order to conveniently analyse the data we linearly interpolated the position fixes to half hourly intervals.

Figure 2-1: *The island of Puerto Rico. One can see the area of the experiments (enclosed in the hatched rectangle) and the locations of Isla Magueyes and Ponce.*

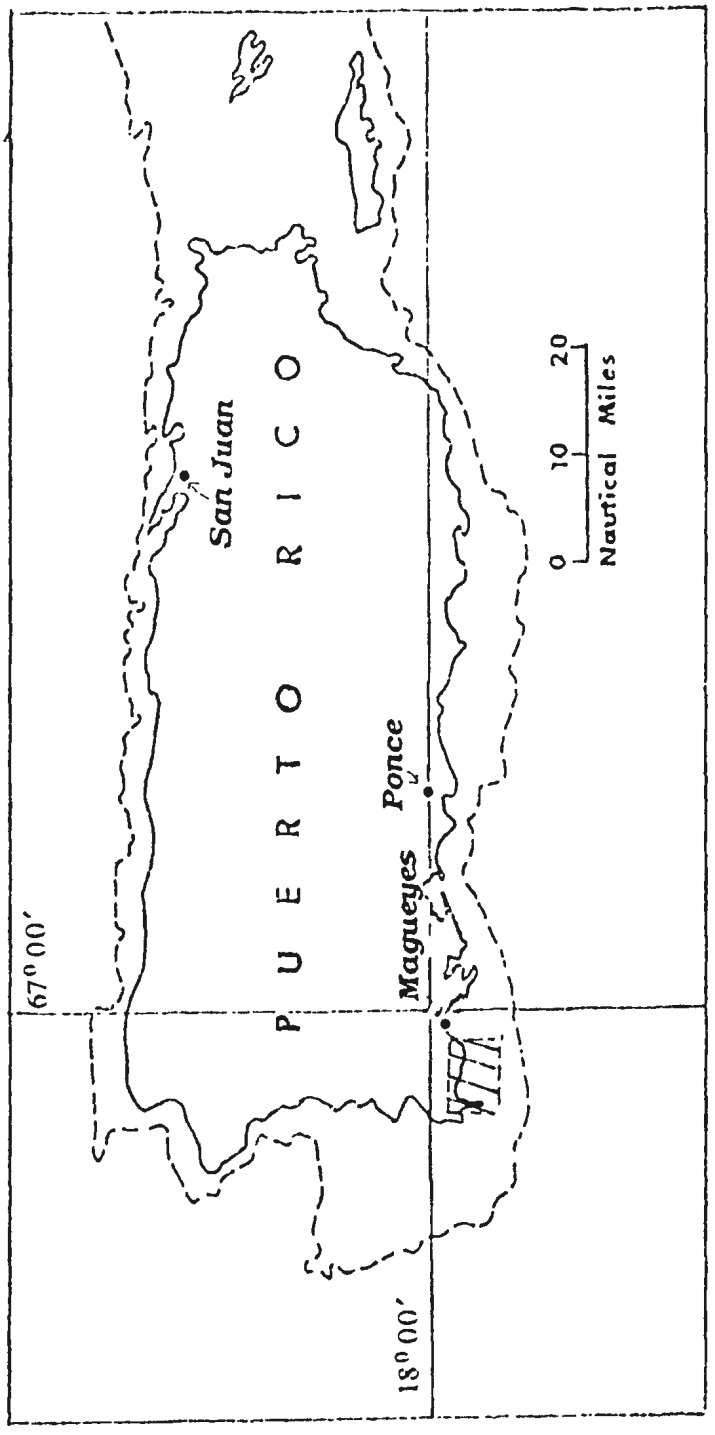

Figure 2-2: *The area of the experiment (land and reefs are shaded), with the location of the trisponder remotes. This map is an enlargement of the rectangular hatched area in Figure 2-1. The hatched area is the area within which the error of the position fix is larger than $4m$, for a range error equal to $1m$. The rectangle encloses the release site San Cristobal.*

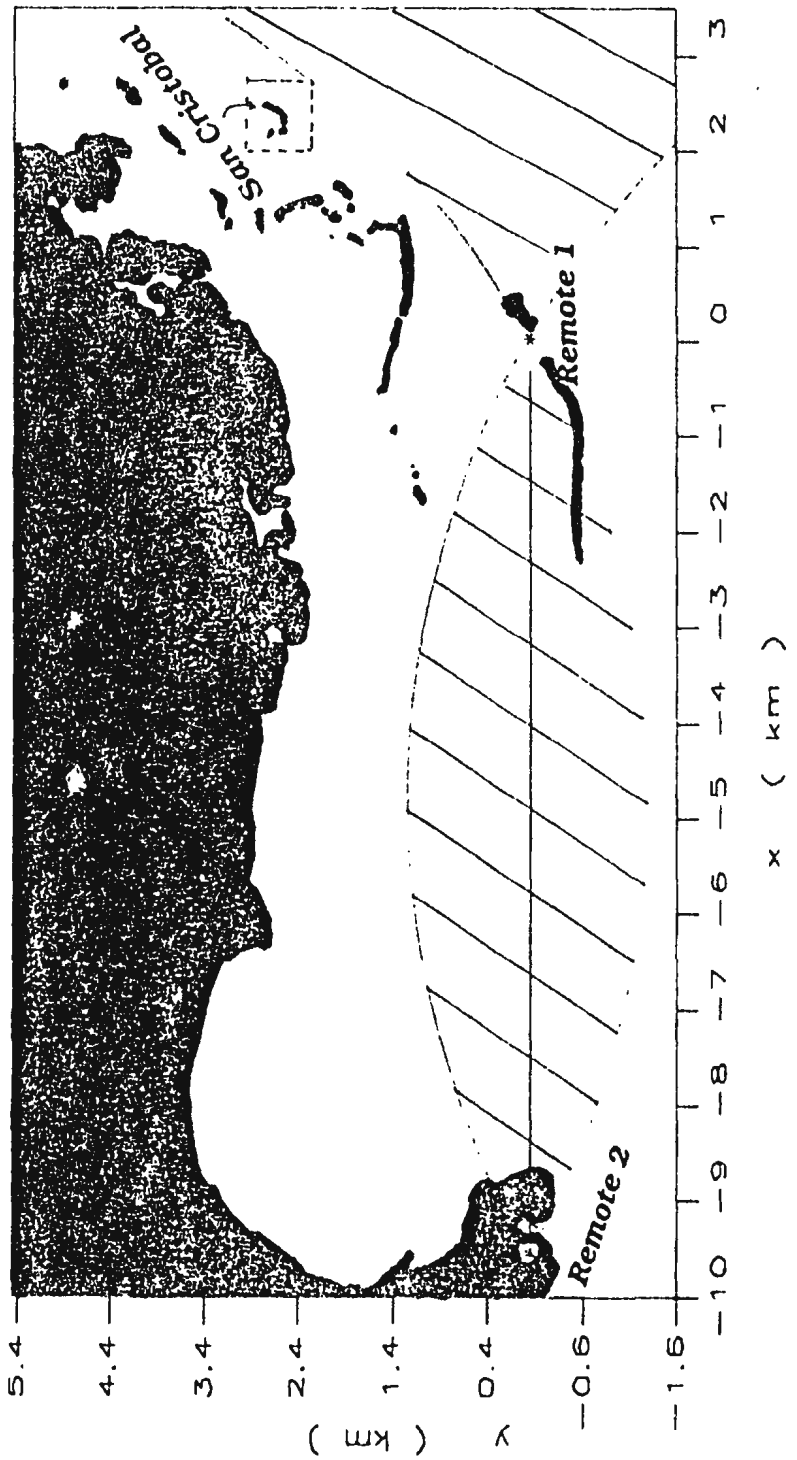

Figure 2-3: *The dye - drifter release method. The spawning S1, S2 and nonspawning NS1, NS2 release sites on San Cristobal reef.*

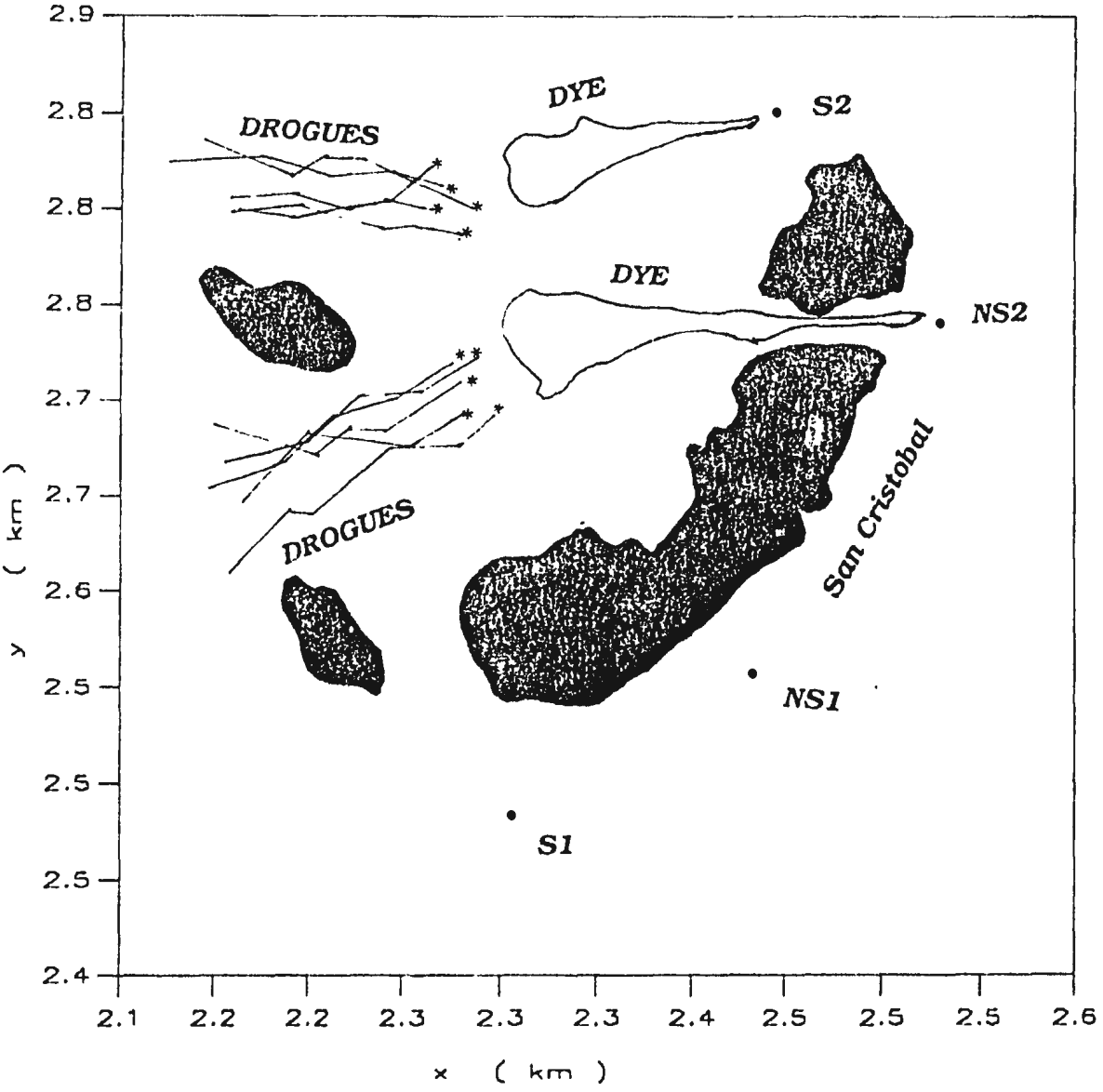

Figure 2-4: *A drogue diagram.*

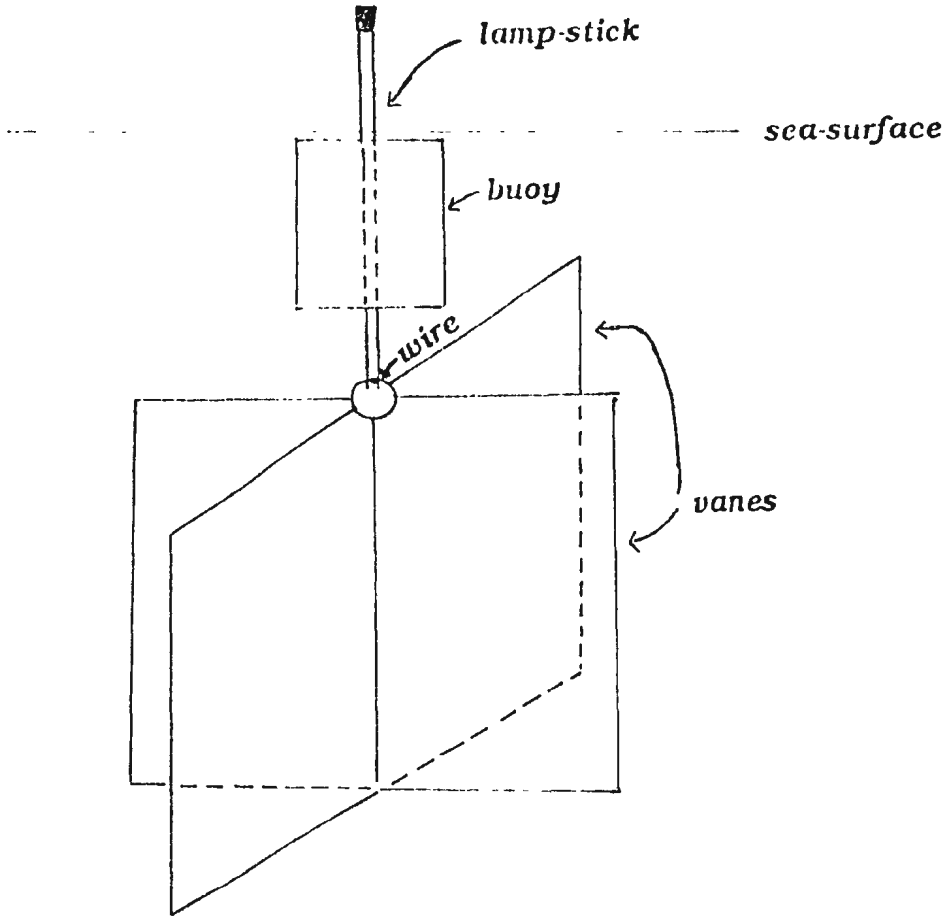

Figure 2-5: *The relation between the error* $(\Delta S_1, \Delta S_2)$ *of the position fix and the range error* Δr. *A and B indicate the positions of the two "remotes". The concentric circles have their centers at A and B respectively. The radii of the concentric circles are equal to* $r_1 \pm \Delta r$ *and* $r_2 \pm \Delta r$, *where* r_1, r_2 *are the two "ranges". The measured position could be anywhere within the area from which the arrow starts. The size of this area is exaggerated with respect to the "baseline" length, for the sake of clarity.*

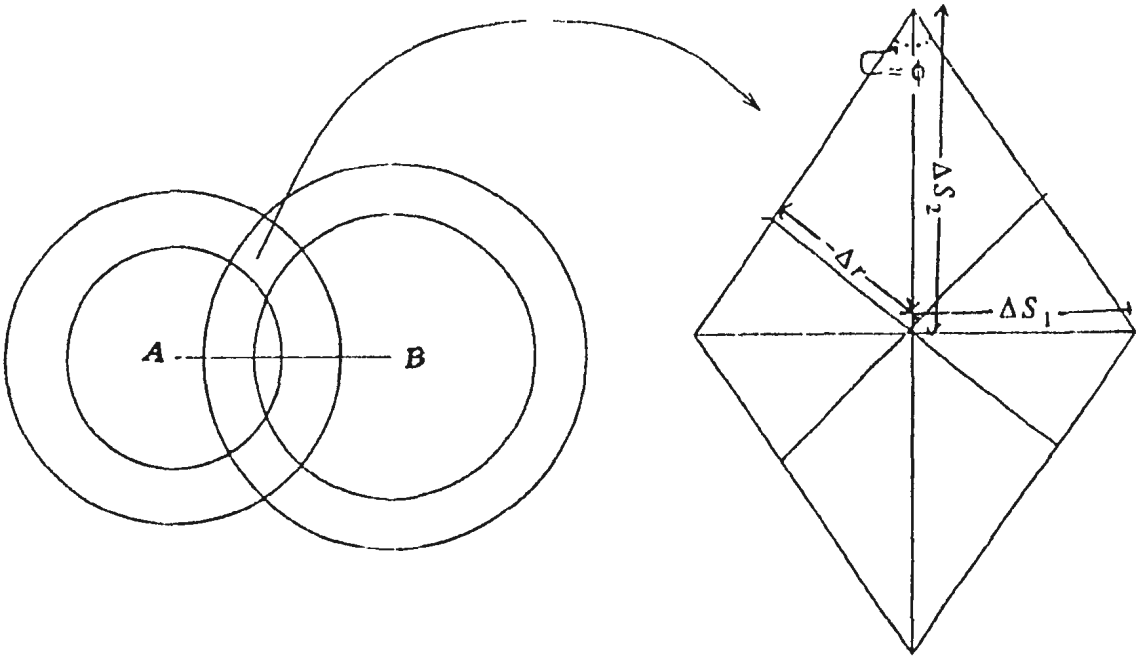

In each experiment, two drifter clusters were released at either a spawning time s (1300 *h*) or a nonspawning time n (0700 *h*). One of the two clusters replaced the dye patch released at a spawning site, and the other replaced the dye patch released at a nonspawning site. Two spawning sites S1, S2 and two nonspawning sites N1, N2 were used, yielding the following 4 pairs of experimental sites (S1, N1), (S1, N2), (S2, N1), (S2, N2) (Figure 2-3). The objective was to see if there is any significant difference in the mean and the variability of S1s, S2s drifter trajectories, from S1n, S2n, N1s, N2s, S1s, N1s, S2s, N2s trajectories. If such a difference could be identified, one could then further examine if the spawning site and spawning time trajectories, are more survival favoring than the nonspawning combinations.

The set of experiments consisted of four combinations of sites each with two different release times. Each of these experiments was replicated. Thus a complete set of experiments consisted of sixteen pairs of cluster releases.

A semi-complete set (i.e., no replicates) of eight pairs of cluster releases was conducted from June 88 until September 88.

Sixteen experiments were carried out from September 1988 to the beginning of December 1988. Another sixteen experiments were carried out at a different season of the year, from the beginning of April until mid-June 1989, to examine if there is seasonal variability in the drifter trajectories. Finally, four experiments were conducted from October to December 1989. All of the above experiments, except for the ones from June to September 1988 were biologically useful, i.e., useful for determining the dependence of the mean drifter-egg trajectories on the initial conditions of their release. In the experiments from June to September 1988, mistakes were made in the identification of the spawning sites, i.e., different sites were used that were not the real ones. For this reason, these experiments are only useful for the estimation of physical parameters of diffusion.

Each of the four inshore pairs of cluster releases, in the period from October to December 1989, was coupled with a single-cluster release at a shelf edge spawning site. We sought to compare trajectories of eggs spawned at the shelf edge with trajectories of eggs spawned at the inshore sites, on San Cristobal reef. In that period we only had six drogues. We used three drogues per cluster for the inshore pairs of cluster releases and all six drogues for the single cluster releases at the shelf edge. We lacked the resources to track inshore and shelf edge clusters simultaneously. The time interval between the end of an inshore experiment and the beginning of a shelf edge experiment, with which the inshore experiment was coupled, was typically three days. In three of the four pairs of experiments, either the inshore or the shelf edge data quality was poor due to trisponder malfunction. Even in days of trisponder malfunction however, we were able to record the general course of the drifters and the wind conditions.

The shelf edge spawning happens at a depth of approximately $21m$. The eggs will move upwards from the spawning site with a buoyancy velocity of $0.00157m/s$ (the buoyancy velocity of fertilized eggs was measured in the lab by the biologists in a column of seawater $11cm$ long and $2.6cm$ in diameter, at $25^{o}C$). Thus it takes about $21m/0.00157m/s = 3.7h$ for the eggs to reach the surface. This was simulated using a number of drogues set at successively lesser depths. A drogue, released at the deep spawning site and set at the spawning depth was later replaced by one, set at an intermediate depth, and so on, until surface drifters were used, after about $3.7h$. A listing of information about all the experiments is given in the following Table 2-1.

Table 2-1: *Experiment Information.*

The columns have the following information (from left to right).

Date: The date of the experiment; L1: A character variable that takes the values "in" or "sh", corresponding to an inshore or a shelf edge experiment respectively; L2: A character variable that takes values "S1" (i.e., inshore spawning site one) and "S2" (i.e., inshore spawning site two). These two values correspond to the inshore release sites of dye on San Cristobal reef (Figure 2-3) where egg spawning occurs; L3: A character variable that takes values "NS1" (i.e., inshore nonspawning site one) and "NS2" (i.e., inshore nonspawning site two). These two values correspond to the inshore release sites of dye on San Cristobal reef (Figure 2-3) where egg spawning never occurs; L4: A character value that takes the values "s" (i.e., spawning time) and "n" (i.e., "nonspawning time"). These values characterize the time of dye release that occurred either at the time of egg spawning (around noon), or at a time when egg spawning never happens (around dawn). If instead of a value of L2, L3, we have - this happens because the release sites used in that experiment were not correct (Summer 1988 experiments), or because the experiment was a shelf edge one, in which case the inshore release sites are not relevant.

Experiment dates and release sites and times				
Date	*L1*	*L2*	*L3*	*L4*
3 August 1988	in	-	-	s
7 August 1988	in	-	-	s
12 August 1988	in	-	-	s
19 August 1988	in	-	-	s
21 August 1988	in	-	-	n
26 August 1988	in	-	-	s
29 August 1988	in	-	-	n

Experiment dates and release sites and times				
Date	*L1*	*L2*	*L3*	*L4*
16 September 1988	in	-	-	s
23 September 1988	in	S2	NS2	s
25 September 1988	in	S2	NS2	n
30 September 1988	in	S1	NS1	s
14 October 1988	in	S2	NS1	s
16 October 1988	in	S1	NS1	n
21 October 1988	in	S1	NS2	s
23 October 1988	in	S2	NS1	n
28 October 1988	in	S1	NS1	s
30 October 1988	in	S1	NS2	n
4 November 1988	in	S2	NS1	s
6 November 1988	in	S1	NS1	n
11 November 1988	in	S2	NS2	s
13 November 1988	in	S2	NS1	n
18 November 1988	in	S1	NS2	s
20 November 1988	in	S2	NS2	n
3 December 1988	in	S1	NS2	n
7 April 1989	in	S1	NS1	s
10 April 1989	in	S1	NS1	n
14 April 1989	in	S2	NS1	s
17 April 1989	in	S2	NS1	n
21 April 1989	in	S2	NS2	s
24 April 1989	in	S2	NS2	n
28 April 1989	in	S1	NS2	s
1 May 1989	in	S1	NS2	n
5 May 1989	in	S1	NS1	s
8 May 1989	in	S1	NS1	n
14 May 1989	in	S2	NS1	n
19 May 1989	in	S2	NS1	s
26 May 1989	in	S2	NS2	s
26 May 1989	in	S2	NS2	s

Experiment dates and release sites and times				
Date	*L1*	*L2*	*L3*	*L4*
29 May 1989	in	S2	NS2	n
2 June 1989	in	S1	NS2	s
5 June 1989	in	S1	NS2	n
23 October 1989	sh	-	-	s
26 October 1989	in	S2	NS2	s
30 October 1989	sh	-	-	s
2 November 1989	in	-	NS2	s
30 November 1989	in	S2	NS2	s
4 December 1989	sh	-	-	s
7 December 1989	in	S2	NS1	s
11 December 1989	sh	-	-	s

Wind speed and direction are available from three sources. (I). Hourly wind direction and speed were measured from the tracking boat (at a height of $2.5m$ above the sea level) with a portable "Dwyer" wind anemometer and compass. These wind measurements (hereafter labelled "O" wind data) are available for all but the Summer 88 experiments, and only exist for the periods when drifters were being tracked. (II). Wind velocity was measured using a weather station at the crest of Isla Magueyes (shown in Figure 2-1), at a height of $27m$ above the sea level. The weather station was a Climet model CI-26, which included a Climet Model 026-1 translator, a Climet 011-2B transmitter, and an Esterline Angus portable analog recorder. These data, hereafter labelled "M" wind data, are digitized at half hour intervals. This island is separated from the mainland by a $80m$ wide channel and is about $10km$ from the centre of the study site. The measurement of wind velocity at Isla Magueyes was started 1 day before drogue releases, to allow for possible lagged correlations between wind and currents. The Isla Magueyes weather station was only operated during the experiments from October to December 1989. (III). Wind data were obtained for all of the experimental days, (and also the days before), from the Ponce Airport (shown in

Figure 2-1), at a height of $10m$ above the sea level. These data (hereafter referred to as "P" wind data) give hourly records for the period $0700\,h$ to $2000\,h$ every day. The Ponce Airport is located approximately $50\,km$ away from the experimental site but still on the same coast (South). It is located approximately $4.5\,km$ away from the coast.

The positive x axis of our coordinate system is tilted $8.7°$ anticlockwise from the meridian. The x axis lies almost parallel to the longer part of local coastline. Thus we can identify the x and y components of the wind as the along-shore one and the across-shore one respectively. The 3 series of wind were correlated to each other, and Table 2-2 shows these correlations. The along-shore component of the "P" wind was highly correlated with the along-shore component of the "O" wind. The along-shore component of the "M" wind was less well correlated with both the "O" and the "P" measurements. This may have been due to mountains on the mainland adjacent to Magueyes. Nevertheless, for the along-shore direction, all wind data series are useful. The order of usefulness is "O", "P", "M", and was based on the correlations in Table 2-2. In particular, the criterion that we used for ranking a wind data source referred to the question of how well a data source is correlated to the two others. In the on/offshore direction, only the correlation of "M" with "P" data is good. This could be due to the fact that, both the "M" and "P" weather stations were near the land-ocean boundary, and therefore, most strongly affected by land-sea breezes, caused by differentials in temperatures over land and sea. The "O" and "P" wind speeds were similar whereas the "M" wind speeds were a factor of two greater than "O" and "P". This is probably due to incorrect instrument calibration at the "M" station.

Table 2-2: ***Correlations between the three wind time series*** *w^x, w^y* ***are the components of the wind along the*** *x* ***and*** *y* ***axes respectively.***

correlations between the 3 wind data sources			
variable	**correl P and M**	**correl P and O**	**correl O and M**
w^x	0.53	0.84	0.66
w^y	0.43	0.09	-0.03
Degrees of freedom	923	478	283

Sea level measurements at Magueyes Island were available for the total study period, August 88 to December 89. These data (hourly time resolution), were the records of a tide gauge on Magueyes Island (Figure 2-1).

In order to examine the effect of the bathymetry on the currents, depth recording was also undertaken for many experiments, using an acoustic depth-sounder mounted at the bow of the boat. A depth measurement was taken along with each drogue fix measurement. We spatially averaged the depth data over $50m \times 50m$ grids and Figure 2-6 shows the depth contours based on the grid averaged data.

Finally we used our trisponder system to digitize the position of the coastline and exposed coral boundaries (Figure 2-2). This was done in order to plot the drifter trajectories on a realistic map, and thus to examine the topography's influence on the mean current and the mixing processes.

Figure 2-6: *The bathymetry of the area of the experiment. The scale is the same as that of Figure 2-2. The land and the coral reefs are shaded. The contours are labelled in m. The contour interval is 1 m.*

2.2. A comparison of the eggs with the drogues.

The fish eggs under study have a radius of $r_e = 2.7 \times 10^{-4} m$ and density $\rho_e = 1013 Kg/m^3$. They are positively buoyant, but turbulence will mix them away from the surface. The eggs are, therefore, expected to be distributed over the top $0.6m$ of the surface layer of the water (see page 36 where we use equation (2.14) to estimate this value). The drifters were drogued over a depth range $0.4 m$ to $1.1 m$. The drifters' motion might differ from the egg motion, due to the drag of the wind on the portions of the drifter above the sea surface (section 2.2.1). Both the eggs and the drogues are very small compared to the typical length scale of horizontal diffusion (i.e., the typical value of the standard deviation of the drifter position with respect to the cluster centroid which is $\approx 100m$) and therefore their diffusivities are expected to be reasonably similar. However, the egg and drogue diffusivities are expected to differ through the vertical shear diffusion effect (section 2.2.2).

2.2.1. The effect of the wind on the motion of the drogues.

The wind drag on the part of a drogue above the sea surface diverts the drogue from the water motion. In this section we provide some estimates of the magnitude of this effect, following the methodology of Kirwan et al., (1975). The drag force $\vec{f}$ of a moving fluid of density ρ_f, on a body exposing an area $A_\perp$ to the fluid, is given by the following formula.

$$\vec{f} = \frac{1}{2} c_d \rho_f A_\perp | \vec{v}_f - \vec{c} | (\vec{v}_f - \vec{c}) \qquad (2.1)$$

Here c_d is a drag coefficient and $\vec{v}_f$ and $\vec{c}$ are the velocity of the fluid far from the body and the velocity of the body respectively. Thus $\vec{v}_f - \vec{c}$ and $| \vec{v}_f - \vec{c} |$ are the fluid velocity and speed relative to the body (at positions far from the body) respectively. We assumed that $\vec{v}_f - \vec{c}$ is normal to the area $A_\perp$. The only significant part of the drogue above the sea surface is the lamp-stick, which can be regarded as an upright cylinder with the horizontal wind

perpendicular to its axis. The most important subsurface part of the drogue will be considered to be a plate immersed in a fluid, with its surface normal to the relative fluid motion. We ignore the drag on the submerged buoy, since its surface is much smaller than the surface of the vanes.

Assuming that the wind and the ocean surface currents are steady, there will be a balance between the drag force $\vec{f}_a$ of the air on the drifter part above the sea surface and the drag force $\vec{f}_w$ of the water on the immersed part of the drifter

$$\vec{f}_a + \vec{f}_w = 0 \,. \tag{2.2}$$

Both of these forces can be expressed by a drag law of the form of (2.1), i.e.,

$$\vec{f}_a = \frac{1}{2} c_a \rho_a A_{a\perp} |\vec{w} - \vec{c}| (\vec{w} - \vec{c}) \,, \tag{2.3}$$

$$\vec{f}_w = \frac{1}{2} c_w \rho_w A_{w\perp} |\vec{u} - \vec{c}| (\vec{u} - \vec{c}) \,, \tag{2.4}$$

where $\vec{u}$, $\vec{w}$ and $\vec{c}$ are the velocities of the water, the air and the drogue respectively. Substituting (2.3), (2.4) in (2.2), and solving the resulting equation for $\vec{c}$, we derive

$$\vec{c} = (\vec{u} + J^{1/2} \vec{w}) / (1 + J^{1/2}) \,, \tag{2.5}$$

where

$$J = \frac{c_a \rho_a A_a}{c_w \rho_w A_w} \,. \tag{2.6}$$

Hence the head of the drogue's velocity vector defines a circle, for a wind speed w as the wind direction changes through 360^o. This circle is centered at $\vec{u}/(1+J^{1/2})$ and has a radius of $(wJ^{1/2})/(1+J^{1/2})$.

The drag coefficients $c_a = 1.2$ and $c_w = 1.1$, correspond to values obtained by Hoerner (1958) for a cylinder and a flat plate respectively (see also Vachon (1975)). The density of the air is taken to be $\rho_a = 1.2\ kg/m^3$ and that of water $\rho_w = 1025\ kg/m^3$. The area of the cylinder above the surface is $A_a \approx 0.6 \times 10^{-2} m^2$ and that of the vane beneath the surface is $A_w \approx 36 \times 10^{-2} m^2$. Substituting these values into (2.6) gives $J^{1/2} = 4.6 \times 10^{-3} \approx 1$. We can therefore approximate (2.5) by

$$\vec{c} = \vec{u} + J^{1/2}\vec{w} \quad . \tag{2.7}$$

Thus the slippage of the drogue through the water, is 0.5% of the wind velocity at the height of the lamp stick ($0cm$ to $30cm$). Our "O" wind measurements were done at a height of $2.5m$ from the sea surface, and so they give an over estimate of the wind drag on the lamp stick. We can however use the $2.5m$ wind to calculate the average wind stress over the vertical extent of the lamp-stick, by means of a suitable boundary layer flow model. In particular, if we neglect such factors as air stability and boundary layer flow of the air around the boat, we can model the wind near the sea surface by a turbulent shear flow near a rigid wall. In such a model the wind speed $w(z)$ varies logarithmically with z (Tennekes and Lumley, 1972; p54). This approximation

$$w(z) = \frac{u^*}{\kappa} \ln z + e \quad . \tag{2.8}$$

where e is an additive constant, κ=0.4 is von Karman's constant and u^* is a friction velocity, that is

$$u^* = \left(\frac{\tau}{\rho_a}\right)^{\frac{1}{2}} = \left(\frac{C_w \rho_a w^2}{\rho_a}\right)^{\frac{1}{2}} = w(C_w)^{\frac{1}{2}} \tag{2.9}$$

where we used a quadratic law for the wind stress τ. The drag coefficient of the sea surface is C_w. A value for w was estimated by taking the root mean square value of the "O" wind speed. This was $5.1m/s$ at $z=2.5m$. C_w was taken to be 1.2×10^{-3} (Amorocho De-Vries, 1980). Substituting these values into (2.9) we derive $u^*=0.17m/s$. Substituting for u^*, $w=5.1m/s$, $z=2.5m$ in (2.8) we derive that the value of the additive constant is $e=4.7m/s$. Equation (2.8) is valid over the range of the turbulent atmospheric boundary layer which typically extends $1000m$ above the sea surface (Tennekes and Lumley, 1972; p12). Equation (2.8) also breaks down in a very small layer right next to the sea surface, where the viscous effects become important (this layer is mentioned as "viscous sublayer" in the literature). The vertical range of the viscous sublayer can be defined as the area in which the Reynolds number is equal to, or less than unity, corresponding to the viscocity terms being equal to, or larger than

the inertia terms in the equations of motion. The Reynolds number characterizing the flow of a wind layer extending a distance z upwards from the sea surface, can be defined as $Re=wz/\nu$, where w is the typical horizontal velocity of the wind inside the layer and ν the kinematic viscosity of the air. Typically in the area of the experiment $w=5.1 m/s$ (root mean square value of the "O" wind). Also $\nu=1.4\times 10^{-5} m^2/s$ (Gill, 1982; p75). For $Re=1$ one gets that $z=0.0003 m$. Summarizing, equation (2.8) is valid for the vertical range from approximately $z=10^{-5} m$ to approximately $z=1000 m$.

We will consider the root mean square value of $w(z)$ over the vertical extent of the lamp stick as the typical value of the wind speed responsible for the drifter slippage. The mean square value $\langle w^2\rangle$ of $w(z)$ over a vertical extent from z_1 to z_2 is.

$$w_{rms}=\frac{\int_{z_1}^{z_2} w^2 dz}{\int_{z_1}^{z_2} dz} \tag{2.10}$$

Substituting (2.8) in (2.10) we derive

$$w_{rms}=\frac{A}{z_2-z_1} \tag{2.11}$$

where

$$A=\frac{(u^*)^2}{k^2}\{z\{(\ln z)^2-2\ln z+2\}\}\Big|_{z_1}^{z_2}+e^2 z\Big|_{z_1}^{z_2}+ \tag{2.12}$$
$$\frac{(2u^* e)}{k}\{z\{\ln z-1\}\}\Big|_{z_1}^{z_2}$$

Taking as $z_1=0.0003 m$, corresponding to the height over which the viscous sublayer extends, and $z_2=0.30 m$, corresponding to the top of the lamp stick, we derive from (2.11) that $w_{rms}=3.8 m/s$, where the subscript rms denotes the root mean square value, i.e., the square root of $\langle w^2\rangle$. Substituting this value into (2.7) we derive that the wind-induced slippage velocity of the drifter is 0.5% of w_{rms} or $\frac{w_{rms}}{w}0.5\% = 0.4\%$ of the observed "O" wind velocity w (where $w=5.1 m/s$). We derive thus that the slippage velocity is $0.019 m/s$. This value is

approximately 20% of the root mean square drifter velocity and generally less than the variability of the mean velocities from one experiment to the next. The wind is nearly parallel to the current. Thus the principal effect of the wind drag would be to cause the mean currents and along-shore egg displacement to be overestimated by about 20%. One should note here that, the wave induced drag on the buoy might also introduce a deviation of the egg motion from the drogue motion, since any drag on the buoy would be partly transmitted on the vanes. This would happen because the buoy and the vanes were not totally decoupled (see Figure 2-4). Wave induced drag on the vanes might also be important, especially in windy days.

2.2.2. Vertical shear diffusion of fish eggs

The drifters can move only in the horizontal plane, whereas the eggs can move both in the horizontal and vertical planes. Shear diffusion results from the interaction of the vertical turbulent diffusion with the vertical gradients in horizontal velocity and increases the horizontal dispersion of eggs relative to drogues. The additional horizontal diffusion of the eggs, induced by shear diffusion can be estimated by using dimensional arguments as follows.

A simple model of the vertical motion of the eggs is to assume a balance between the eggs' upwards buoyant flux, $w_b S$, and the eggs' downwards turbulent flux, $K_z \frac{\partial S}{\partial z}$, according to the following equation

$$w_b S = K_z \frac{\partial S}{\partial z} . \tag{2.13}$$

Here w_b and $S=S(z)$ are the eggs' buoyant velocity and concentration. The vertical eddy diffusivity is K_z. Scale analysis of (2.13) reveals a length scale Z, of the vertical diffusion of the eggs

$$Z = \frac{K_z}{w_b} . \tag{2.14}$$

The eggs' time scale T, for diffusion (or advection) over the distance Z is

$$T=\frac{Z}{w_b}=\frac{K_z}{w_b^2}\ . \tag{2.15}$$

The time scale T is the period required for the near steady state, described by (2.13) to develop. Eggs will be distributed over a vertical length scale Z, over which there will be a vertical gradient Ω of the mean horizontal velocity, due to the friction boundary layer that is created when wind blows over shallow water. Eggs at different depths will therefore be moving with different velocities. In a time T, a point source of eggs near the surface will diffuse over a vertical distance Z, in which case the shear Ω will disperse them over a horizontal distance

$$X=\Omega Z T\ . \tag{2.16}$$

The difference between the velocity of eggs at the surface and eggs at Z is ΩZ. Thus the "apparent diffusivity" due to shear diffusion K_a, would have a scale equal to

$$K_a=\frac{X^2}{T}=\Omega^2 Z^2 T\ . \tag{2.17}$$

Using (2.14), (2.15) to express Z and T in terms of w_b and K_z gives the apparent eddy-diffusivity

$$K_a=\frac{\Omega^2 K_z^3}{w_b^4}\ . \tag{2.18}$$

Three experiments were conducted to measure Ω_i $(i=1,2)$ the vertical shear in the x and y components of velocity. In each experiment drifters were drogued at each of the depths $0m$, $2m$ and $4m$. Each experiment had a duration of $0.5h$. This duration ensured that the horizontal distances between the drifters remained small enough to avoid aliasing by horizontal shears. The three experiments were conducted inside the experimental area, under similar wind conditions, (wind speed $3m/s$ to $5m/s$, wind direction $\approx 100^o$).

The velocities of drifters at different levels, enabled us calculate the vertical

gradients of the horizontal velocity Ω_i. For the calculation of Ω_i, drifter velocities over $0.5h$ intervals were used, i.e., average velocities over the duration of an experiment. This was done in order to minimize the error of Ω_i, induced by the trisponder position fix error. In fact, this last error was estimated in the field to be of the order of $5m$. This error was estimated by taking two subsequent Trisponder measurements at the sea. This process was repeated many times, in days when the wind was completely calm. In calm days the boat did not drift substantially during the time (typically a few seconds) over which the two measurements were conducted. The pair of two subsequent Trisponder measurements therefore corresponded to the same position. If the two fixes were not identical, the distance between them was considered as error of the position fix. The value of $5m$ is the root mean square over the all the distances between between the two position fixes (20 degrees of freedom). The error of Ω_i is of the order of $\frac{5m}{1800s \times 2m} \approx 10^{-3}s^{-1}$.

The results of the calculations for Ω_i can be seen in Table 2-3. In the Table we can see that the gradients of the top level ($0m$ to $2m$) tend to be slightly larger than the bottom level ones ($2m$ to $4m$). At the top level the average vertical shear in along-shore current is $\Omega_1 = 9 \times 10^{-3}s^{-1}$ and the average vertical shear in across-shore current is $\Omega_2 = 2 \times 10^{-3}s^{-1}$. The vertical shear in along-shore current is larger than the vertical shear in across-shore current at both levels because the mean flow is predominantly in the along-shore direction.

An approximate formula for the vertical diffusivity K_z in a shallow water area is (Csanady, 1982; p13)

$$K_z = \frac{u^* h}{Re}. \tag{2.19}$$

where Re is the Reynolds number that for a shallow area is approximately 20, $h = O(10m)$ is the width of the wind mixed layer (i.e., the Ekman depth, which is calculated in page 59) and $u^* = 0.17m/s$ a friction velocity corresponding to the

wind stress at the sea surface, given by equation (2.9). Substitution of the above mentioned values into (2.19) gives $K_z = 0.085 m^2/s$. This value gives an order of magnitude of the vertical eddy diffusivity within the domain of the water column far from the top and bottom layers each of approximate thickness of $1m$. In these "wall" layers the horizontal current varies logarithmically with depth, and the vertical eddy diffusivity varies rapidly with the vertical coordinate (Csanady, 1982; p13). A large percentage of the egg patch is expected to be within the surface "wall" layer due to their buoyancy (within the top $60cm$, as will be shown later in this paragraph). A value of $K_z = 10^{-3} m^2/s$ is pertinent to the top layer of the water (Okubo pers.com.). The buoyancy velocity (rate of ascent) of the eggs was measured in the lab and was $w_b = 1.6 \times 10^{-3} m/s$. A good estimate of the vertical shear of the mean current at the top $2m$ of the water column is $\Omega = 10^{-2} s^{-1}$ (see Table 2-3). Substituting these values in (2.14), (2.15), we get $Z = 0.6m$ and $T = 6.5 min$ respectively. Substitution of the values into (2.18) gives $K_a = 1.5 \times 10^{-2} m^2/s$. This is 2 orders of magnitude smaller than the along-shore diffusivity ($=8.9 m^2/s$) and across-shore diffusivity ($=2.4 m^2/s$) of the cluster dispersion (see section 4.3.2). But there is considerable uncertainty in K_z and a factor of 4 increase in K_z could make the apparent diffusivity comparable in magnitude to the cluster diffusivity. K_a is even more sensitive to variability of w_b.

Table 2-3: ***Vertical gradients of the horizontal velocity of the current***

Ω_1 is the vertical shear of the horizontal along-shore (x) current. Ω_2 is the vertical shear of the horizontal across-shore (y) current.

Vertical gradients of the horiz. velocity (s^{-1})				
exp.	$\Omega_1 (0m-2m)$	$\Omega_1 (2m-4m)$	$\Omega_2 (0m-2m)$	$\Omega_2 (2m-4m)$
exp.1	8×10^{-3}	6×10^{-3}	2×10^{-3}	1×10^{-3}
exp.2	9×10^{-3}	6.5×10^{-3}	2.6×10^{-3}	1.8×10^{-3}

Vertical gradients of the horiz. velocity (s^{-1})				
exp.	$\Omega_1(0m-2m)$	$\Omega_1(2m-4m)$	$\Omega_2(0m-2m)$	$\Omega_2(2m-4m)$
exp.3	8.7×10^{-3}	6.7×10^{-3}	2.3×10^{-3}	1.9×10^{-3}

Chapter 3

Dynamical processes driving the currents on the reef

3.1. General circulation characteristics

The small depth (typically $20m$ on the shelf and $5-10m$ in the area of the experiment) and the negligible stratification (see Faucher, 1971) result in the surface and bottom Ekman layers overlapping (see section 3.3, page 59 for the calculation of the depths of the two Ekman layers). Therefore, it is realistic to assume that the surface wind stress and the bottom frictional stress are transmitted throughout the water column on the reef. Along-shore pressure gradients will also be transmitted from offshore onto the shelf because the shelf is narrow (see section 3.4, page 65). In the steady state the wind stress will be approximately balanced by bottom stress and the along-shore pressure gradients throughout the water column. This flow is locally modified by both the topography and the bathymetry. Figure 3-1 shows the mean Eulerian velocity field. The mean Eulerian velocity field was calculated by dividing the area into grid boxes of $500m$ by $500m$, and averaging all drifter velocities that fell within a box over the duration of the experimental program. In Figure 3-1, the mean velocities are drawn as arrows, whereas the standard deviations about the mean velocity components are in the form of crosses, centered at the origins of the arrows. The number at each grid box indicates the number of drifters averaged over at this box. The hatched area in Figure 3-1 shows where drifter fixes are unreliable (i.e., with fix errors bigger than $4m$, for a range error equal to $1m$) due to trisponder triangulation errors. The Figure also shows the mean vector of the wind (averaged over the "O" wind data). We see that the wind is westwards, and that the mean current tends to be parallel to the wind to the

extent that the orientation of the coast and channels permits. We also see that the standard deviation of velocity is larger in amongst the shallow reefs, indicating a larger velocity variability as the mean wind-driven flow is diverted around obstacles. The effect of the bathymetry on the mean current can be examined if we compare Figure 3-1 with Figure 2-6 of the bathymetry. The comparison shows that in some places (in the area around $x=-2000m$, $y=1500m$ for example) the mean current flow tends to orient parallel with the isobaths. In such areas the bathymetry might be important for the currents. In some other areas however (in amongst the reefs especially) the flow was across the isobaths.

In eighteen out of the forty eight experiments the flow has been observed to reverse and temporarily follow an eastwards direction. When this happened, the wind was weak westwards, or completely calm (only in one case was the wind eastwards).

The flow reversals might be caused by along-shore pressure gradients opposing the wind, and dominating the along-shore current when the wind relaxes (Tyler, 1992).

Figure 3-1: *The Eulerian mean velocity field. The hatched area is the area of large trisponder error of the position fix (more than 4m, for a range error equal to 1m). The scale is the same as that of Figures 2-2, 2-6.*

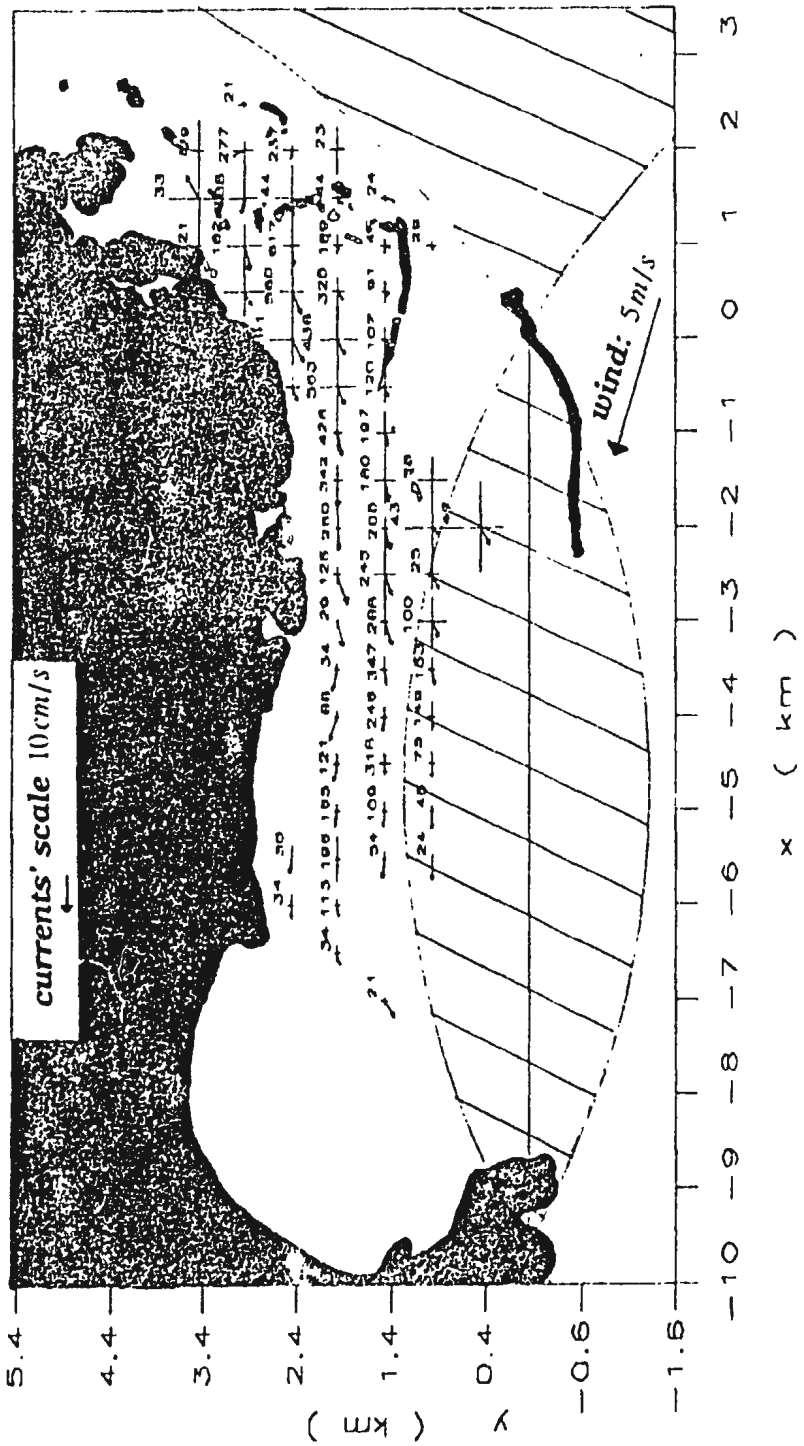

3.2. Tides and Seiches

Spectral analysis of the sea surface elevation time series reveals a strong diurnal tidal component with period $T=23.93h$, and amplitude of about $\eta_0=0.10m$, and a weaker semidiurnal component with $T=12.42h$ and $\eta_0=0.02m$, as can be seen in Figure 3-2 of the spectral density function of the sea surface elevation $S(f)df$, where f is the frequency in cycles per day. In Figure 3-3 we have plotted the time series of the sea surface elevation. The series spans over the period of the experiments (approximately 333 days), and the mean surface elevation over this time period has been extracted. We see in this Figure that the amplitude of the neaptide is approximately $3cm$, whereas the amplitude of the springtide is approximately $16cm$, and that there is a seasonal sea level change with amplitude $15cm-20cm$. Each of the temperature, salinity and atmospheric pressure seasonal variations, contribute almost equally to the seasonal variation of the sea level (Fancher, 1971). According to Kjerfve (1981) the most important tidal harmonics for the South coast of Puerto Rico, where our experiments took place, are the diurnal components K1, O1, P1 with sea surface elevation amplitudes of $0.07m$, $0.05m$ and $0.02m$ respectively, and the semidiurnals M2, S2, N2 with sea surface elevation amplitudes of $0.01m$, $0.007m$ and $0.003m$ respectively. These values are in reasonable agreement with the values for the semidiurnal and diurnal tide of our spectral density function. The Greenwich phase of the diurnal harmonics is constant along the South coast of Puerto Rico, which is approximately parallel to our x axis. Thus, on the shelf, we can model the diurnal tidal harmonics as one-dimensional (across-shelf, i.e., along the y axis) standing waves forced at the shelf edge by the diurnal sea surface elevation, as follows.

Consider the one-dimensional (across-shore) shallow water equations, i.e.,

$$\frac{\partial u^y}{\partial t}=-g\frac{\partial \eta}{\partial y}, \tag{3.1}$$

$$\frac{\partial \eta}{\partial t}+H\frac{\partial u^y}{\partial y}=0,$$

where H is the constant depth on the shelf, y is the cross-shelf coordinate, u^y is the cross-shelf velocity and η is the sea surface elevation. Equations (3.1) are subject to two boundary conditions. First, to the diurnal sea surface elevation at the shelf edge, i.e., $\eta=\eta_0\cos(\omega t)$ at $(y=0)$, where $\omega=2\pi/T_d$ is the diurnal frequency and η_0 is the surface elevation amplitude of the diurnal harmonic. Second, to zero across-shelf flow at the coast, i.e., $u^y=0$ at $y=L$. The solution to (3.1), subject to the above boundary conditions is

$$u^y=-\frac{\eta_0\omega}{lH\cos(lL)}\sin(l(y-L))\sin(\omega t), \tag{3.2}$$

$$\eta=\frac{\eta_0}{\cos(lL)}\cos(l(y-L))\cos(\omega t),$$

where $l=\frac{\omega}{c}=\frac{\omega}{\sqrt{gH}}$, the across-shelf wavenumber of the standing wave. For our case $H=20m$ and $\omega=2\pi/86400s$, yielding $l\approx 5\times 10^{-6}m^{-1}$. The shelf width is $L\approx 2\times 10^4 m$, thus $lL\approx 10^{-1}\ll 1$. Thus the diurnal tidal elevation and velocity on the shelf can be approximated by

$$\eta\approx\eta_0\cos(\omega t), \tag{3.3}$$

$$u^y\approx\gamma(L-y)\sin(\omega t), \tag{3.4}$$

where $\gamma=\eta_0\omega/H$ and the cross-shore velocity amplitude is $u_0^y(y)=\gamma(L-y)$. Taking as $\eta_0=0.07m$, i.e., the largest diurnal surface elevation amplitude in the area, corresponding to the tidal harmonic K1 (Kjerfve, 1981), we derive that the velocity amplitude ranges from $u_0^y(y)=0$ at $y=L$ (coast), to $u_0^y(y)=5\times 10^{-3}m/s$ at $y=0$ (shelf-edge). In particular, for the location of the experiments, $y=15km$, and the corresponding velocity amplitude is $u_0^y(y)=\gamma(L-y)=12\times 10^{-4}m/s$. The root mean square value of the y component of the current was $3\times 10^{-2}m/s$

(Table 3-1), which is one order of magnitude larger than the across-shore tidal current of K1 (the across-shore velocities of the other diurnal harmonics will be even smaller than K1 since they have smaller surface elevation amplitudes). The diurnal tidal current is therefore insignificant on the reef.

From Kjerfve's tidal charts (1981) we see that, the Greenwich phase of the semidiurnal harmonics changes 30^{o} as we progress from the Southeastern to the Southwestern corner of Puerto Rico, over an along-shore distance $S=2\times10^{5}m$, and this indicates that the semidiurnal harmonics are progressive waves propagating along the South coast. The wavelength λ of these waves is the distance required for a 360^{o} phase change, i.e., $\lambda=\frac{360\times S}{30}=24\times10^{5}m$. This wavelength is much larger than the typical depth $H'=4\times10^{3}m$ of the ocean basin South from Puerto Rico and the typical shelf depth $H=20m$. We can therefore model the semidiurnal tidal harmonics as shallow water waves. The phase speed of these harmonics is $c=\frac{\lambda}{T_s}=\frac{24\times10^{5}m}{43200s}=55m/s$, where T_s indicates the semidiurnal period. This value is four times larger than the phase speed $\sqrt{gH}=14m/s$ of the shallow water waves on the shelf, and four times smaller than the phase speed $\sqrt{gH'}=200m/s$ of the shallow water waves offshore from the South coast. It is therefore reasonable to assume that the semidiurnal tidal harmonics propagate along-shore in an area between the shelf and offshore, for example at the shelf edge. Their phase speed c is relatively large and it would take them $\frac{S}{c}=1h$ to propagate along the South coast and $\frac{S'}{c}=6min$ to propagate along the area of the experiment that has an along-shore length $S'=2\times10^{4}m$. One can therefore assume that the semidiurnal harmonics force on the shelf (and especially in the area of the experiments) standing across-shelf waves. In this case, one can substitute the amplitude of the sea surface elevation and the frequency of the semidiurnal tidal harmonics into equation (3.4) to derive the corresponding across-shore velocity amplitudes. Taking as $\eta_0=0.01m$, the amplitude of the sea surface elevation of M2, which is the semidiurnal

harmonic with the highest surface elevation amplitude for our area (Kjerfve, 1981), we derive a velocity amplitude $u_0^y(y) = \gamma(L-y) = 36 \times 10^{-5} m/s$ at the area of the experiment, where $y \approx 15 km$. Thus, the semidiurnal tide is insignificant compared with the measured across-shore currents of $3 \times 10^{-2} m/s$.

No significant correlation was found between the drifter velocities and sea level measurements. This supports the above theoretical results, which indicate that tidal currents are very weak on the reef.

Another phenomenon related to the area is the seiche. Seiches are standing waves observed at embayments or shelfs. They are excited by pressure disturbances reaching the mouth of a bay or the shelf edge. They usually are characterized by small periods. In our case the seiche period was $T = 50 min$ and the seiche amplitude of sea surface elevation was $\eta_0 = 3 \times 10^{-2} m$, as was estimated by spectral analysis of sea surface elevation data, performed by Giese et al., (1982). The seiche is not resolved by our spectral density function (Figure 3-2). This is because its period of $T = 50 min$ is smaller than the time resolution of $1 h$ of our sea surface elevation time series.

We will again use the standing wave theory developed in the discussion about the diurnal tide earlier in this chapter. Substituting the above values of seiche period and amplitude of sea surface elevation into equation (3.2) (equation (3.4) does not hold here, since the approximation that $l/L \ll 1$ is no longer valid for the seiche) we derive a seiche (across-shore) velocity amplitude at the area of the experiment of approximately $u_0^y(y) = 2.3 \times 10^{-2} m/s$, which is similar to the root mean square value of the measured across-shore current speed of $3 \times 10^{-2} m/s$. The seiche is therefore important for the currents in the area. This seiche is presumably excited at the shelf edge, by traveling internal solitary waves (Giese et al., (1982)). The maximum seiche activity occurs approximately 7 days after the full and new moon. This correlation of the maximum seiche activity with the phase of the moon, as well as the fact that

the seiche normally occurs in fortnightly groups, can be explained as follows according to (Giese et al., (1982)). The internal solitons that seemingly excite the seiches at the shelf edge, are created at the Southern portion of the Carribbean sea. There, the dominant tide is the semidiurnal, that has maxima (spring tide) and minima (neap tide) at the full and new moon respectively. The internal solitons result from the interaction of the spring and neap tides with bottom irregularities, and it takes them seven days to reach the South coast of Puerto Rico from the Southern Carribbean.

Table 3-1: *The mean wind and the mean current.*

w^x, w^y are the components along the x and y axes, of the velocity of the wind. We averaged over the "O" wind data; u^x, u^y are the components along the x and y axes of the velocity of the surface current. We averaged over our drifter velocity data; w, u are the wind speed and current speed respectively; (-) in the column of mean values corresponds to nearly southwards direction for the y axis and to nearly westwards direction for the x axis (the angular deviation of our y axis from the axis of latitude is only 8.7° anticlockwise).

Variable	Mean	rms
$w^x(m/s)$	-3.4	4.3
$w^y(m/s)$	0.5	1.5
$w(m/s)$	3.9	5.1
$u^x(m/s)$	-0.05	0.09
$u^y(m/s)$	-0.01	0.03
$u(m/s)$	0.05	0.12

Figure 3-2: ***The spectral density function of the sea surface elevation, $S(f)df$. The error bars indicate 80% confidence limits, and the estimation of $S(f)df$ has 30 degrees of freedom.***

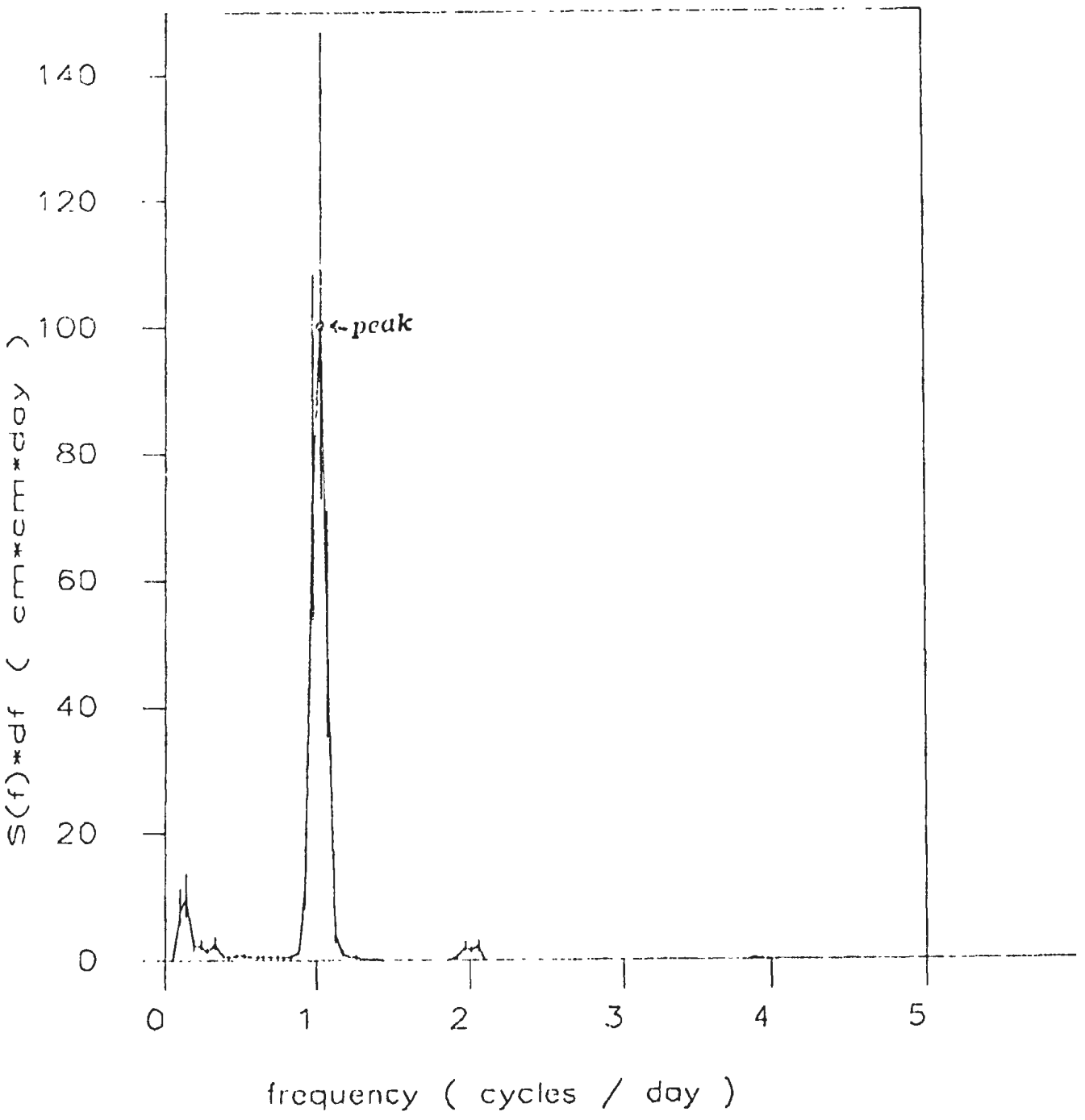

Figure 3-3: *The time series of the sea surface elevation. The mean value over the duration of the time series has been extracted.*

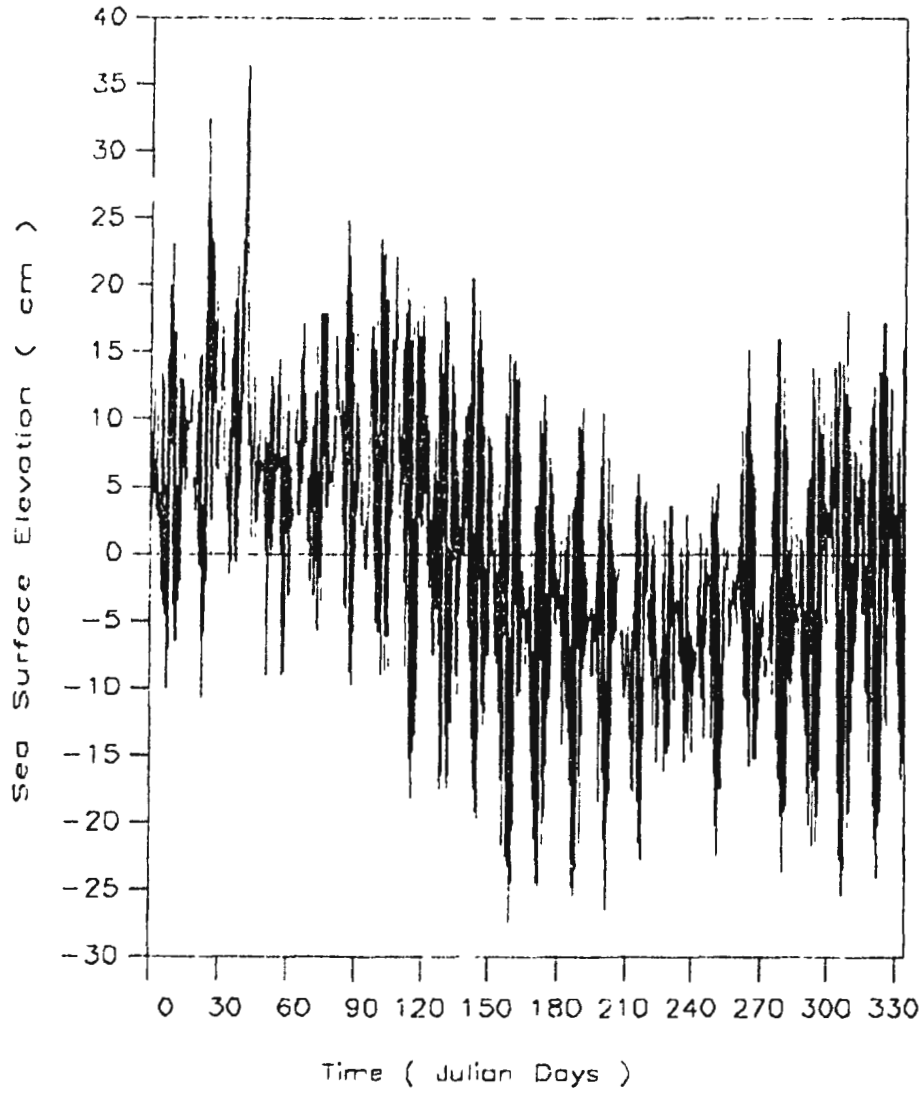

3.3. The effect of the wind on the currents

We calculated the mean wind vector $(\langle w^x\rangle(t),\langle w^y\rangle(t))$ as a function of the time of the day t as follows.

$$(\langle w^x\rangle(t),\langle w^y\rangle(t))=(\sum_{n=1}^{N} w^x(t)/N,\sum_{n=1}^{N} w^y(t)/N)\ ,$$

where $(w^x(t),w^y(t))$ is a measurement of the wind at the time t of the day $(0h\le t\le 24h)$, and N is the total number of wind measurements that were conducted at t, throughout the one and half years of the experimental program. The calculations were separately performed over each of the "O", "P", "M" wind time series, and were performed at half hourly intervals from $0000h$ to $2400h$. At this point one should note that our positive x axis is tilted anticklockwise from the meridian by only 8.7^o. Thus we will henceforth identify the positive x and y directions as East-West and North-South respectively, on the understanding that there is a small deviation between the true East and the positive x direction.

In Figures 3-4, 3-5 we have plotted $\langle w^x\rangle(t)$ and $\langle w^y\rangle(t)$. In each of them there are three curves corresponding to the "O", "P" and "M" time series of wind velocity. The three curves are different due to the fact that they correspond to wind data taken at different heights from the sea level and at different distances from the coast. We will base our conclusions for the North-South component of the mean wind vector only on the "O" data, since they were the only ones taken at the sea and in the area of the experiment (see page 26 for detailed explanation). Our conclusions for the East-West component of the mean wind vector will be based on all three sets of wind data, but again more weight will be given to "O" data. It is clear from all three curves of Figure 3-4, that there are 2 distinct time regimes for the x component. The "O" data especially give a westwards (negative) wind component from $2100h$ to $0900h$ (night/morning regime) of typical absolute values from 2 to $3m/s$, whereas from $0900h$ to $2100h$ the "O" westwards wind has larger absolute values (4 to $5m/s$). We can also

see that the westward "O" wind reaches its largest value of about $5 m/s$ between $1200\,h$ and $1600\,h$. The mean westward component of the "O" wind at the time interval from $0900\,h$ to $2100\,h$ has an absolute value that is four to five times larger than the absolute value of the mean northward component of the "O" wind at that time interval, but both components have similarly small magnitudes (up to $2 m/s$) during the remaining portion of the day.

The mean current vector $(\langle u^x \rangle(t), \langle u^y \rangle(t))$ is plotted as function of the time t of the day in Figures 3-6 (x component) and 3-7 (y component). The calculation technique was similar to that of the mean wind as function of the time of the day. The calculations were based on our drifter velocity data and give the surface currents. In Figure 3-6 we can see that $\langle u^x \rangle(t)$ tends to be negative, corresponding to a westwards direction. The positive spike at around $0800h$ corresponds to the flow reversals towards the East, that were observed in some of our experiments, when the wind was very light (see section 3.4). The mean westwards surface current varies with the time of the day in a way similar to the way that the mean westwards wind does. It has small magnitude in the night/morning regime ($4 cm/s$), and larger magnitude in the day regime (8 to $12 cm/s$). In Figure 3-7 we see that $\langle u^y \rangle(t)$ does not vary with time in a similar manner to $\langle w^y \rangle(t)$. These observations agree with the correlations between the currents (drifter velocity averaged over the cluster) and each of the three wind time series. These correlations were calculated as functions of the lag τ, the current lagging. In the x direction the highest correlation coefficients are 0.85 at $\tau=0\,h$ for the "O" wind, 0.80 at $\tau=0\,h$ for the "P" wind, and 0.70 at $\tau=3\,h$ for the "M" wind. The fact that the highest correlation occurs at $\tau=0$ for the "O" wind data, does not necessarily imply that the current responds to the wind immediately, since correlation at zero lag might also be caused by such factors as the along-shore "O" wind being autocorrelated for a few hours (lagged autocorrelation). There is no significant correlation between currents and wind in the y direction.

Based on the above, and also on the fact that the x axis lies almost parallel to the longer part of the local coastline (see Figure 2-2), we conclude that the wind tends to drive an along-shore flow, and that both the transient and the steady state of the response of the current to the wind can be modelled by one dimensional (x axis) barotropic equations of motion to a good approximation. Deviations from the one dimensional equations might be due to the variability of bathymetry and topography, i.e., variability of the curvature at the coast, presence of coral reefs.

Figure 3-4: *The x component $\langle w' \rangle(t)$ of the mean wind vector as function of the time of day t. The error bars indicate ± 1 standard deviation of the mean. The angular deviation of our x axis from the meridian is 8.7° anticlockwise. The negative values indicate an approximately westwards direction.*

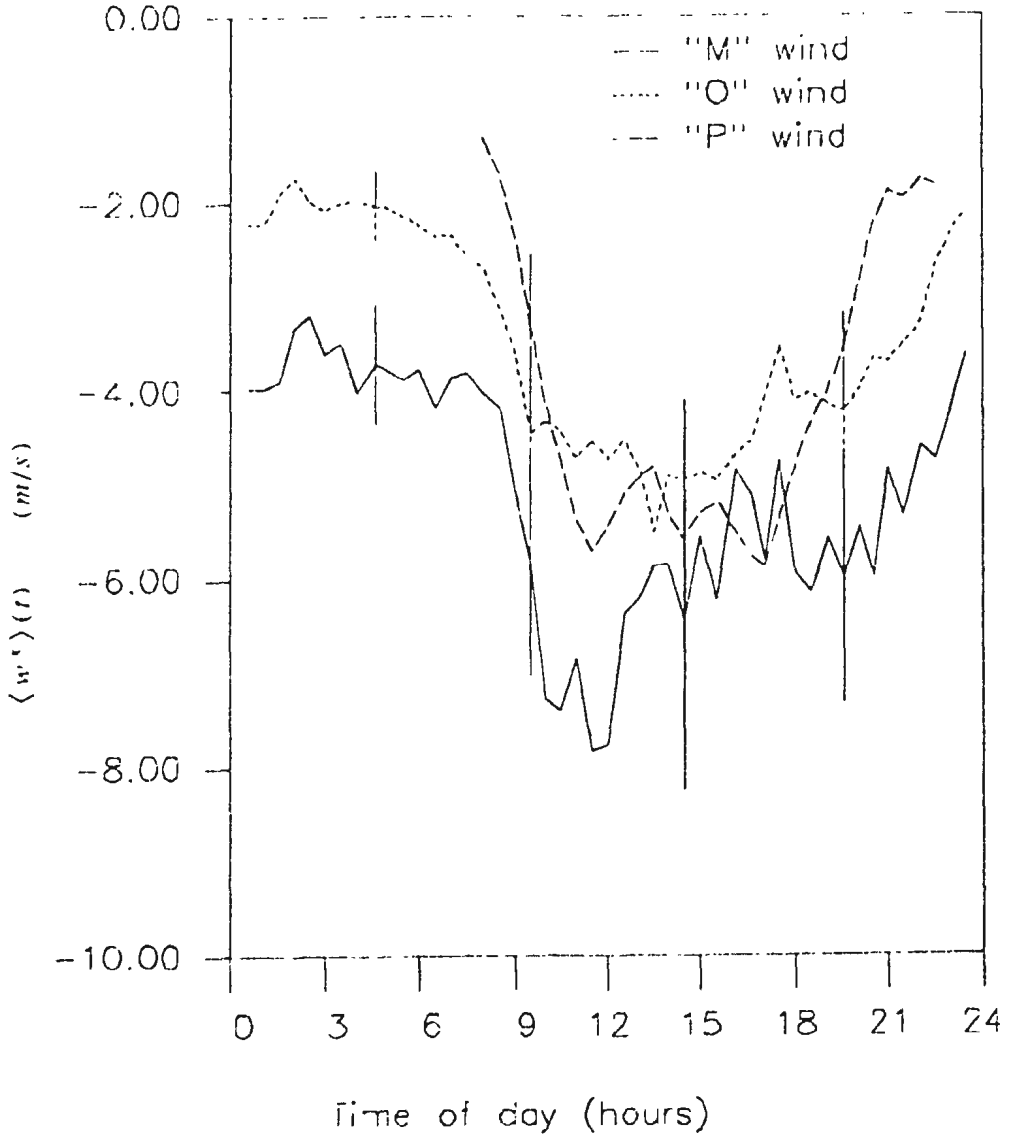

Figure 3-5: ***The y component $\langle w^y \rangle(t)$ of the mean wind vector as function of the time of day t. The error bars indicate ± 1 standard deviation of the mean. The angular deviation of our y axis from the axis of latitude is 8.7° anticlockwise. Positive values indicate an approximately northwards (towards the shore) direction.***

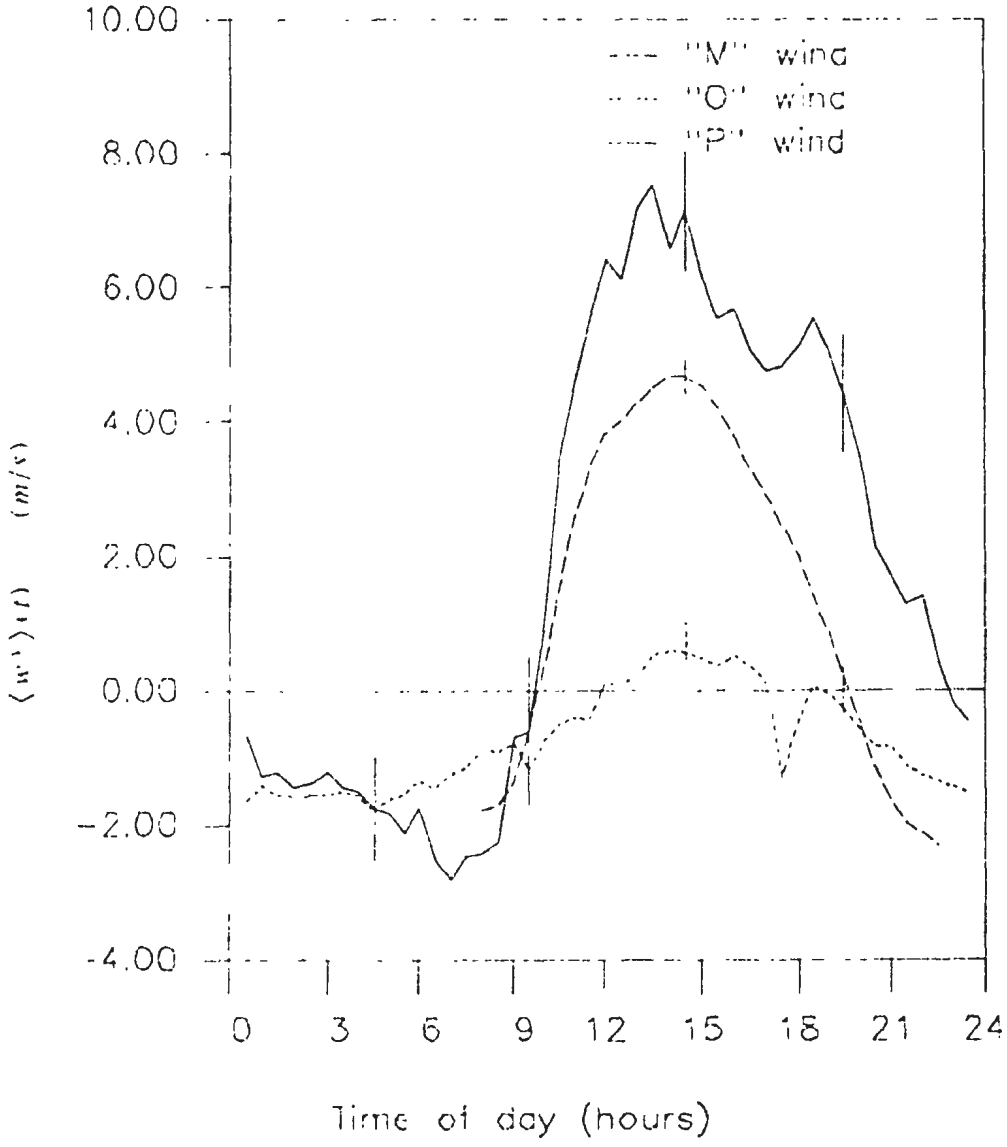

Figure 3-6: ***The x component $\langle u^1 \rangle(t)$ of the mean surface current vector as function of the time of day t. The error bars indicate ± 1 standard deviation of the mean. The angular deviation of our x axis from the meridian is 8.7° anticlockwise. The negative values indicate an approximately westwards direction.***

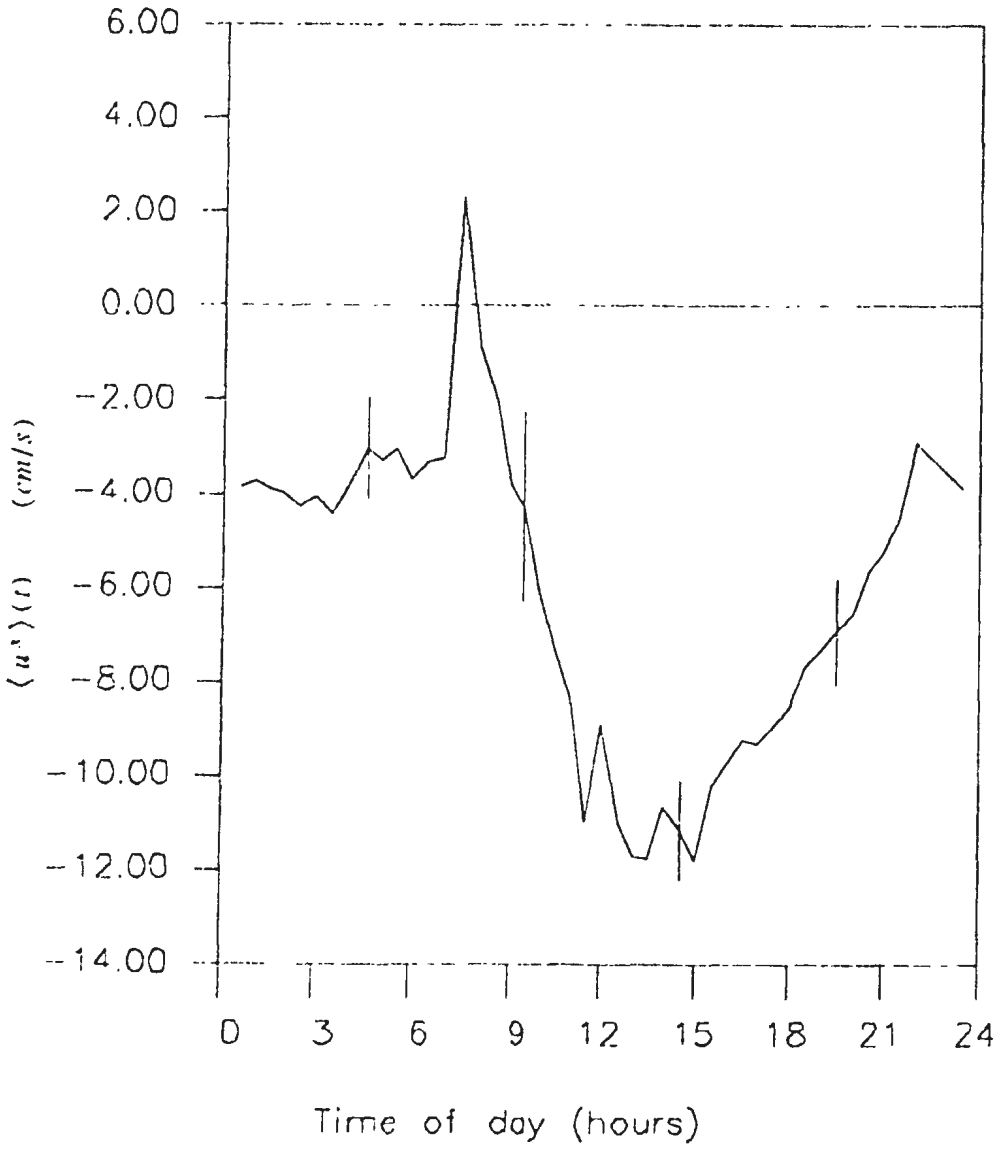

Figure 3-7: *The y component $\langle u^s \rangle(t)$ of the mean surface current vector as function of the time of day t. The error bars indicate ± 1 standard deviation of the mean. The angular deviation of our y axis from the axis of latitude is 8.7° anticlockwise. Positive values indicate an approximately northwards (towards the shore) direction.*

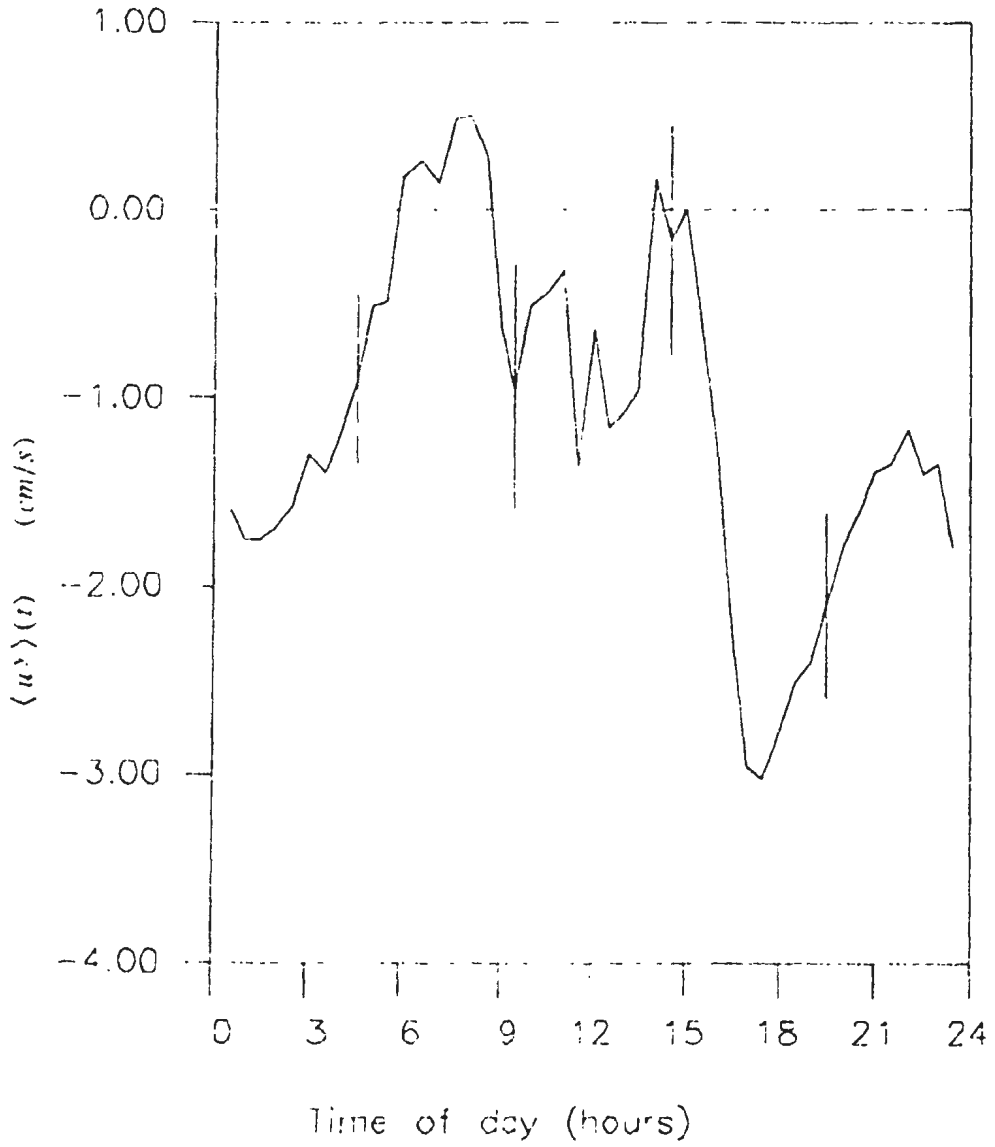

The transient response

The southwestern coast of Puerto Rico, where our experiments took place, is nearly parallel to our x axis (Figure 2-2). Therefore we will assume hereafter in our estimations an idealized coast, that is a straight line parallel to the x axis. As a consequence, the along-shore (x) Coriolis force can be assumed to be equal to zero, since the presence of the coast imposes zero across-shore (y) velocity of the current. Finally we will assume that the wind blows in a direction parallel to the coast, along the x axis. This assumption is reasonable, since the x component of the mean wind is seven times larger than its y component (see Table 3-1). These simplifications result in the following transport equation, derived by integrating the along-shore momentum equation over the constant depth H

$$\rho_w \frac{\partial U^x}{\partial t} = \tau^x - B^x - H\frac{\partial P}{\partial x}. \tag{3.5}$$

Here U^x is the along-shore transport, B^x is the along-shore bottom stress, τ^x is the along-shore wind stress, ρ_w the density of water and $\frac{\partial P}{\partial x}$ an along-shore pressure gradient, opposing the wind stress, assumed to be independent of depth (Tyler, 1992).

We shall assume that the along-shore bottom stress is given in terms of the along-shore depth averaged velocity by a quadratic law (Csanady, 1982; p179)

$$B^x = \rho_w c_b \left|\frac{U^x}{H}\right| \frac{U^x}{H}, \tag{3.6}$$

where c_b is the bottom friction coefficient. We shall also use a quadratic law for expressing the along-shore wind stress in terms of the along-shore wind velocity w^x, that is

$$\tau^x = \rho_a c_w (w^x)^2, \tag{3.7}$$

where c_w is a wind stress coefficient, and ρ_a is the density of the air.

Also we shall ignore the effect of a possible pressure gradient $\frac{\partial P}{\partial x}$ momentarily. Substituting equations (3.7), (3.6) into (3.5) we derive

$$\rho_w \frac{\partial U^A}{\partial t} = \rho_a c_w (w^A)^2 - \rho_w c_b \left| \frac{U^A}{H} \right| \frac{U^A}{H} . \tag{3.8}$$

Assume that a constant along-shore wind stress $\tau^A = \rho_w (u^*)^2$ starts at $t=0$. For this case the bottom friction has a known direction, i.e., it will be opposing the wind-driven flow. We can therefore drop the absolute value in (3.8) to derive

$$\rho_w \frac{\partial U^A}{\partial t} = \rho_a c_w (w^A)^2 - \rho_w c_b \left(\frac{U^A}{H} \right)^2 . \tag{3.9}$$

Csanady (1982; p.176) solved (3.9) and derived the following time scale t_f for adjustment of the current to the wind

$$t_f = \frac{H}{2 u_* c_b^{1/2}} . \tag{3.10}$$

For the area of the experiment, $H \approx 5m$ (see Figure 2-6 of the bathymetry); $\rho_w \approx 10^3 kg/m^3$; $\rho_a \approx 1.2 kg/m^3$; $c_b = 1.1 \times 10^{-3}$ (Csanady, 1982; p179); $c_w = 1.2 \times 10^{-3}$. Note that c_w is dependent upon the wind speed, (Large and Pond, 1980; Amorocho Devries, 1980); $u^* = \left(\frac{\tau^A}{\rho_w}\right)^{1/2} = \left(\frac{\rho_a c_w (w^A)^2}{\rho_w}\right)^{1/2} \approx 0.005 m/s$, where $w^A \approx 4.3 m/s$ is the root mean square value of the x-component of the "O" wind (see Table 3-1). Substituting these values into (3.10) we derive a frictional time scale t_f, of about $4.1h$. This value of t_f can be interpreted as the lag time of highest correlation between the wind and the current, since it represents the time scale after which the approximate steady state of the along-shore current is reached, provided the wind is steady. It agrees with the high correlations between wind and currents for current lags in the range $0h$ to $3h$.

The steady state

The value of t_f is approximately three times smaller than the time scale of change of the along-shore (x) wind as can be seen in Figure 3-4 of the mean x component of the wind as a function of the hour of the day. Thus it is not appropriate to assume steady state at all the times. In Figure 3-6 however we also see that it is reasonable to assume that the along-shore current is in a near-steady state for the periods of the day from $0000h$ to $0700h$ and from $1200h$ to $1800h$, when both the along-shore wind and the along-shore current

remain constant to a good approximation. A "near-steady state" assumption would be improper for the remaining portions of the day, since both the along-shore current and the along-shore wind are in a transitional state. The steady state equation can be obtained by eliminating the time dependence in (3.9), as follows

$$\rho_a c_w (w^x)^2 = \rho_w c_b (\frac{U^x}{H})^2 , \tag{3.11}$$

from which we obtain the following steady state solution for the along-shore depth averaged current velocity u^x

$$u^x = \frac{U^x}{H} = w^x (\frac{\rho_a c_w}{\rho_w c_b})^{1/2} . \tag{3.12}$$

Substituting into (3.12) the values of w^x, ρ_a, ρ_w, c_b, and c_w, that were specified in our discussion about the transient response of the current to the wind, we derive that the depth averaged current is equal to $u^x = 0.14 m/s$. This is only slightly larger than the root mean square value of the along-shore surface current u'^x measured by our drifters (which is equal to $0.09 m/s$ as can be seen in Table 3-1). The slight difference between u'^x and u^x can be attributed to uncertainties in the bottom and the wind stress coefficients, and to the fact that the assumptions of steadiness ($\frac{\partial}{\partial t} = 0$) and linearity of flow ($\frac{\partial}{\partial x} = 0$) implied in (3.11) are not completely valid.

Note that u'^x is expected to have similar magnitude with u^x. This is a consequence of the fact that the surface and bottom Ekman boundary layers are overlapping, i.e., the wind stress and the bottom stress are transmitted throughout the water column. In a much deeper shelf there would be a layer between the two Ekman boundary layers, controlled by the inertial motions, and this layer might introduce a substantial deviation of the depth averaged velocity from the near surface velocity.

Let us now perform some calculations that prove that the two boundary

Ekman layers are indeed overlapping. The turbulent Ekman layer extending from the water surface downwards (forced by the wind stress) has a typical depth D_s that is given by the following empirical formula (Csanady, 1982; p12)

$$D_s = 0.1\frac{u^*}{f}. \tag{3.13}$$

Here $u^* = (\frac{\tau^x}{\rho_w})^{\frac{1}{2}}$ is a friction velocity, τ^x, ρ_w being the along-shore wind stress and the water density respectively, and f is the Coriolis parameter. For the area of the experiment $u^* = 0.005 m/s$ as already calculated in page 57 and $f = 5 \times 10^{-5} s^{-1}$. Substituting these values into (3.13) we derive that $D_s = 10m$, which is similar to the depth of the area. Regarding the Ekman layer extending from the bottom upwards (forced by bottom friction), we again can use (3.13) for calculating the typical layer width D_b. However, now u^* is the bottom friction velocity, i.e., $u^* = (\frac{B^x}{\rho_w})^{1/2} = (\frac{\rho_w c_b (u^x)^2}{\rho_w})^{1/2} = u^x c_b^{1/2}$, where B^x is the along-shore stress, expressed in terms of the water density ρ_w, the bottom stress coefficient c_b and the depth averaged velocity u^x. Taking $c_b = 1.1 \times 10^{-3}$ and $u^x = 0.14 m/s$ as estimated above (see page 58) we derive $u^* = 0.005 m/s$. Inverting this value and the value of Coriolis parameter $f = 5 \times 10^{-5} s^{-1}$ into (3.13) we derive a typical bottom boundary layer width $D_b = 10m$, which again is similar to the depth in the area of the experiment.

3.4. The flow reversals

The westwards wind drives a westwards current. Sometimes however, the current reverses and flows eastwards. All but one of the reversals happened during the wet season from July to December. Reversals have been observed during both the inshore and the shelf edge experiments. Both the wind and the current were plotted as functions of time for each of the "reversal" experiments, and the observations based on these plots are summarized in Table 3-2, which lists the dates of "reversal" experiments, the maximum eastwards velocity of the current u_{max}, and the time averaged (over the period of the eastwards flow)

along-shore "O" wind w. The hours of the day over which the flow is eastwards are given in the T_{occur} column. The duration of the eastwards flow has a mean value of $6.5h$ and ranges from $2h$, to $12h$. The maximum eastwards (positive) current velocity ranges from $0.02m/s$ to $0.10m/s$ with a mean value of $0.06m/s$. The time averaged along-shore "O" wind over the period of the eastwards flow ranges from $-2m/s$ to $+2m/s$ with a mean value of $-1m/s$. The negative sign indicates a westwards direction of wind, and the values of the Table confirm the fact that during the eastwards flow the wind is typically westwards and light (except for the experiment on October 21, 1988, when the wind during the eastwards flow of the current has also an eastwards direction).

Table 3-2: ***Dates and information about flow reversals.***

The first column indicates the date of initiation of the experiment and whether it was conducted inshore or at the shelf edge; u_{max} ***is the maximum eastwards (positive) current.*** w ***is the time averaged value of the along-shore "O" wind over the period of the eastwards flow. The negative values indicate westwards direction;*** T_{occur} ***indicates the time intervals of the day over which the eastwards flow occurred.***

Dates and info about reversal			
Exp.Date	$u_{max}\ (cm/s)$	$w(m/s)$	$T_{occur}\ (h)$
16 Sep 88 / inshore	0.04	-1	2130 - 0200
23 Sep 88 / inshore	0.06	-0.5	1900 - 0600
25 Sep 88 / inshore	0.02	-1.5	1830 - 2130
30 Sep 88 / inshore	0.05	-0.5	1900 - 0700
16 Oct 88 / inshore	0.04	-1	0800 - 1100
21 Oct 88 / inshore	0.04	2	0000 - 1200

Dates and info about reversal			
Exp.Date	$u_{max}\ (cm/s)$	$w(m/s)$	$T_{accum}\ (h)$
23 Oct 88 / inshore	0.03	-0.5	1300 - 1600 and 2200 - 0400
28 Oct 88 / inshore	0.08	-1	1900 - 0330
30 Oct 88 / inshore	0.10	-1.5	1330 - 1930
4 Nov 88 / inshore	0.08	-2	1300 - 2300
13 Nov 88 / inshore	0.10	-1	0830 - 1230
20 Nov 88 / inshore	0.08	-1	0900 - 1000 and 2030 - 2230
3 Dec 88 / inshore	0.08	-2	1600 - 0030
7 Apr 89 / inshore	0.03	-2	1230 - 1830
2 June 89 / inshore	0.05	-1	2230 - 0600
23 Oct 89 / shelf - edge	0.08	-1	1430 - 1200
4 Dec 89 / shelf-edge	0.09	-1	1430 -1730 and 0230 - 1030
7 Dec 89 / inshore	0.06	-2	0130 - 0600

We hypothesize that the eastwards reversals of the currents, that happen when the wind is light or completely calm, are caused by an along-shore pressure gradient $\frac{\partial P}{\partial x}$, opposing the wind, transmitted onto the shelf from the offshore (see the discussion in page 65). We estimated the approximate value of this gradient, using our drifter velocity and wind data, as follows.

In a nonstratified shelf as ours, we can assume that $\frac{\partial P}{\partial x}$ is independent of depth (shallow water equations, see also Tyler, 1992). We hypothesized that the along-shore wind stress τ^A is balanced by the along-shore bottom stress B^A and the integrated over depth along-shore pressure gradient $H\frac{\partial P}{\partial x}$, according to the following equation

$$\tau^x = B^x + H\frac{\partial P}{\partial x}. \tag{3.14}$$

This equation neglects accelerations and so is strictly appropriate for only the "near-steady state" periods of the day, mentioned in the first paragraph of the discussion about the steady state. Assuming that both the along-shore wind stress and the along-shore bottom stress are quadratic functions of the x component of the wind velocity w^x and the depth averaged current velocity $u^x = \frac{U^x}{H}$ respectively, equation (3.14) gives

$$\rho_a c_w (w^x)^2 = \rho_w c_b (u^x)^2 + H\frac{\partial P}{\partial x}, \tag{3.15}$$

or

$$(w^x)^2 = \frac{\rho_w c_b}{\rho_a c_w}(u^x)^2 + \frac{H\frac{\partial P}{\partial x}}{\rho_a c_w}. \tag{3.16}$$

Equation (3.16) uses the along-shore depth averaged current u^x, whereas our along-shore drifter velocities u'^x are near surface velocities. Let $q = \frac{u^x}{u'^x}$. Equation (3.16) can then be expressed in terms of u'^x and q as follows

$$(w^x)^2 = \frac{\rho_w c_b q^2}{\rho_a c_w}(u'^x)^2 + \frac{H\frac{\partial P}{\partial x}}{\rho_a c_w}. \tag{3.17}$$

Were the pressure gradient a constant, then (3.14) would represent a linear relation between the wind stress and the bottom stress, and also (3.17) would represent a linear relation between $(w^x)^2$ and $(u'^x)^2$.

Assuming a constant pressure gradient, we could regress linearly the time series of $(w^x)^2$ versus the time series of $(u'^x)^2$. In this regression we only used values of $(w^x)^2$ and $(u'^x)^2$ that occurred in the "near-steady state" periods of the day. According to equation (3.17) the intercept and the slope of the regressed line are equal to $\frac{H\frac{\partial P}{\partial x}}{\rho_a c_w}$ and $\frac{\rho_w c_b q^2}{\rho_a c_w}$ respectively. From the value of the intercept we could estimate the value of $\frac{\partial P}{\partial x}$, whereas from the value of slope we

could estimate a value for q. We applied the regression separately for each of the three time series of wind "M", "O", "P". Table 3-3 lists the estimates of $\frac{\partial P}{\partial x}$ (from intercept) and of q (from the slope). We can see that $\frac{\partial P}{\partial x}$ is of the order of $0.01 \pm 0.001\,Pa$ eastwards (positive). Figure 3-8 shows the along-shore component of the wind stress τ^x ("O" wind data) versus the bottom stress B^x, where the value of the wind stress at some time is plotted against the value of the bottom stress at the same time, and a pair of wind and bottom stress values has only been plotted if it occurred in a "near-steady state" period of the day (note that positive values of the wind stress and of the bottom stress correspond to an eastwards stress direction). We see in this plot that the relation between the two stresses is not strictly linear, since there is considerable scattering of points about the line of best fit, which is also included in the plot. This scattering might be caused by a variety of reasons, such as experimental errors of the measurements of the wind and the current, lack of a completely steady state even in the "near-steady" periods of the day, and the fact that the pressure gradient might by varying from experiment to experiment, since it probably is proportional to the wind stress, that is also variable (Tyler, 1992). The pressure gradient, that has a value equal to the intercept of the line of best fit in Figure 3-8, would drive an eastwards (x axis) flow when the wind pauses. In the steady state, the pressure gradient would be balanced by the bottom stress according to the following equation

$$H\frac{\partial P}{\partial x}=\rho_w c_b (u^x)^2 \,. \tag{3.18}$$

Substituting for $\frac{\partial P}{\partial x}=0.001\,Pa$ and $c_b=1.1\times10^{-3}$ in (3.18), we derive that $u^x \approx 10\,cm/s$. This value is of the same order of magnitude as the measured maximum eastwards velocities of Table 3-2.

In Table 3-3 we also see that $q=0.83$ for the "O" data, $q=0.70$ for the "P"

data, and $q=0.88$ for the "M" data. These values of q are near unity, a fact that is in agreement with our hypothesis that the wind and bottom stress are transmitted throughout the water column (ideally this would result in $q=1$, since the along-shore current would be independent of depth).

Table 3-3: ***Estimate of the adverse pressure gradient by linear regression of the wind stress versus the bottom stress.***

$w-s$ is the wind source ("P", "O", "M"); $\frac{\partial P}{\partial x}$ is the estimate of the along-shore pressure gradient; std is the standard deviation of $\frac{\partial P}{\partial x}$; $corr$ is the correlation coefficient between the wind stress and the bottom stress; q is the ratio of the depth averaged along-shore current to the along-shore drifter current.

$w-s$	$\frac{\partial P}{\partial x}(Pa)$	$std\,(Pa)$	$corr$	q
"P"	2.1×10^{-2}	1.9×10^{-3}	0.52	0.70
"O"	1.2×10^{-2}	1.2×10^{-3}	0.56	0.83
"M"	1.6×10^{-2}	2.0×10^{-3}	0.42	0.44

Tyler (1992) explains how along-shore pressure gradients can arise offshore from a circular island, in the presence of a constant wind stress. Note that the shape of Puerto Rico can be approximated reasonably well by a circle, especially from the point of view of offshore dynamics. He uses a 1.5 layer model for the ocean, in which the ocean consists of a thin surface layer of light water and an infinitely deep layer of denser water lying under the first layer, both layers having uniform water density. Such a model is appropriate for the oceanic area offshore from Puerto Rico, since the depth of the thermocline is only $100m$ whereas the typical depth of the ocean basin is $4000m$. The offshore pressure gradient is the result of the adjustment of the ocean to the wind and the Coriolis forces in the presence of the coast. Far from the coast, there is an Ekman balance between the Coriolis force, the wind stress and a linearized friction. As we approach the coast, the along-shore Coriolis force becomes weaker since the presence of the coastal boundary does not permit across-shore flow, and an interfacial gradient arises as a response. This interfacial gradient

is associated with a pressure gradient of equal magnitude but opposite sign in the thermocline. This pressure gradient is a dipole field around the island, and the positions of its maximum values depend on the relative importance of the Coriolis force and the linearized friction. Any along-shore pressure gradient, generated by the above or other mechanisms will be transmitted onto the shelf from the offshore, as Tyler (1992) shows, by solving the barotropic equations of motion on a flat circular shelf, forced by offshore pressure gradients at the shelf edge. His theoretical calculations agree with his experimental data which indicate that in the area of our experiments, there will be a pressure gradient opposing the wind stress, having a magnitude proportional to the magnitude of the wind stress. This "adverse" pressure gradient would take over and reverse the currents when the wind pauses.

Figure 3-8: *The along-shore component of the wind stress ("O" wind data) versus the along-shore component of the bottom stress. Positive values of wind stress and bottom stress indicate that the stresses have an eastwards direction. Plotted is also the straight line that best fits the data. Its intercept is equal to* $H\frac{\partial P}{\partial x}$.

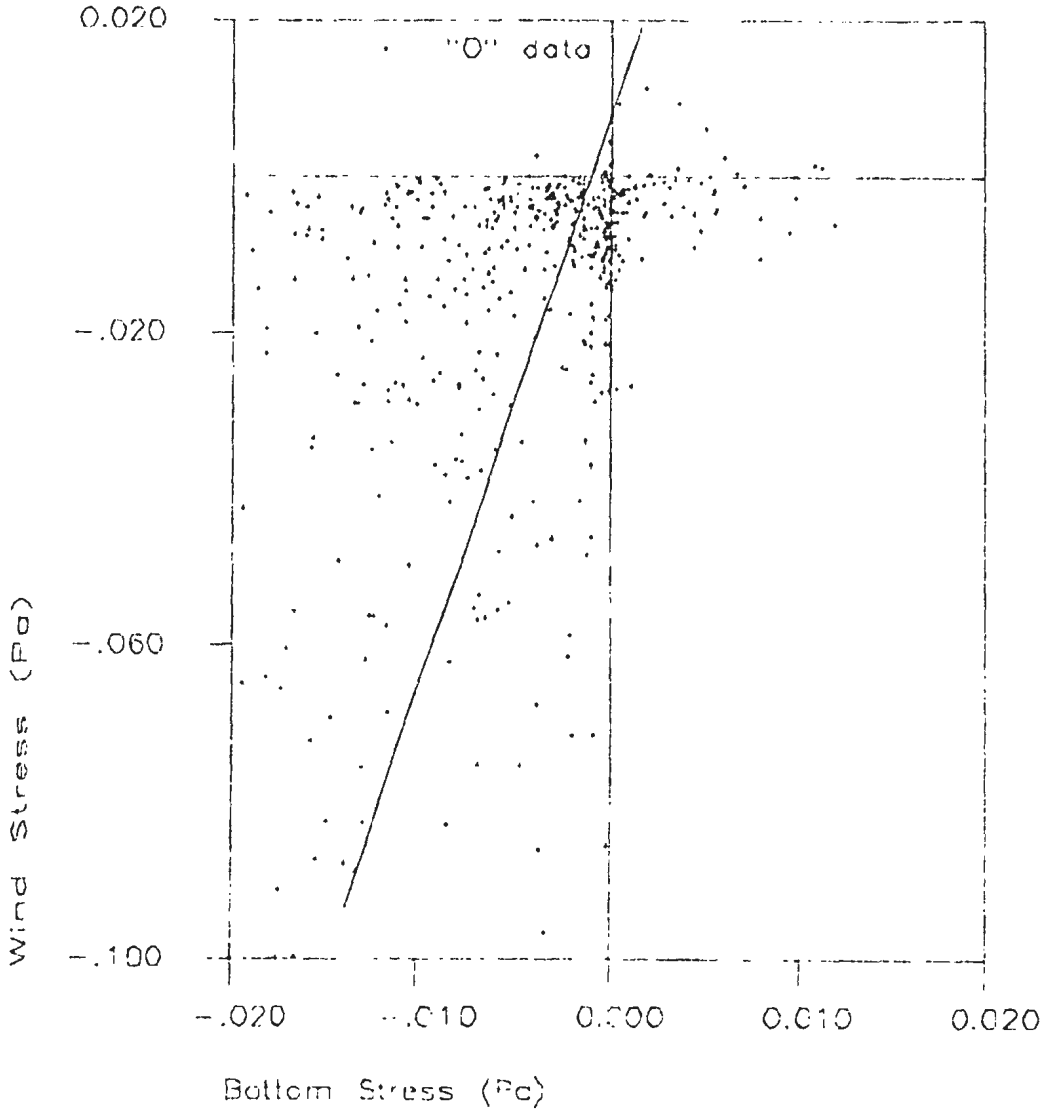

Chapter 4

Analysis of transport and diffusion on the reef

4.1. Introduction

Three types of statistical analyses are commonly employed to study drifter trajectories: the single particle, two particle and cluster statistics (Okubo, 1962). The single particle analysis gives the statistics of the absolute motion of an ensemble of individual particles. The two particle analysis gives the statistics of the relative motion of a pair of particles. Finally, cluster analysis gives the statistics of the motion of a cloud of particles relative to its centroid. The present project is particularly concerned with the dispersion of clouds of fish eggs and the variability of the centroid motion of these clouds. In this thesis, therefore, only single particle and cluster statistics will be analyzed.

The statistical analysis is performed on such cluster characteristics as area (A) of a cluster, elongation (ε) of a cluster, and orientation (θ) of the principal axes of dispersion. The principal axes of dispersion (X,Y) are defined at any time as the major and minor axes along which the variance of drogue positions is a maximum and minimum respectively. These axes may be thought of as the major and minor axes of the ellipse that best represents the cluster's shape. Standard deviations of the drogue positions along the major and minor axes σ_X,σ_Y can be expressed as the following functions of variance (σ_x^2,σ_y^2) and covariance (σ_{xy}) in the working coordinate system, t,x,y

$$\sigma_X=[\cos^2\theta\sigma_x^2+\sin^2\theta\sigma_y^2+\sin 2\theta\sigma_{xy}]^{1/2}\ ,$$
$$\sigma_Y=[\sin^2\theta\sigma_x^2+\cos^2\theta\sigma_y^2-\sin 2\theta\sigma_{xy}]^{1/2}\ . \tag{4.1}$$

The angular deviation (θ), in an anticlockwise sense, of the principal axes (X,Y) from the chosen working coordinates is

$$\theta=\frac{1}{2}\tan^{-1}\frac{2\sigma_{xy}}{\sigma_x^2-\sigma_y^2}\ . \tag{4.2}$$

Equations (4.1), (4.2) arise from an orthogonal transformation from the working coordinate system x,y into such a coordinate system X,Y, for which the covariance σ_{XY} of the drifter position is zero. Cluster area and elongation are defined as

$$A(t)=4\pi\sigma_X(t)\sigma_Y(t)\ , \tag{4.3}$$
$$\varepsilon(t)=\frac{\sigma_X(t)}{\sigma_Y(t)}\ .$$

4.2. The single particle statistics.

4.2.1. Introduction

The time since a drifter was released will subsequently be referred to as Lagrangian time. The averaging was performed over all drifters released throughout the experimental period to obtain single-particle statistics. This form of ensemble averaging is independent of the release time and therefore assumes statistical stationarity. The drifter release sites varied from experiment to experiment (within an area of approximately $500\,m$ radius), so the above averaging also assumes spatial homogeneity. Examining the diffusion with respect to the average trajectory of the drifters as a function of Lagrangian time, is referred to in literature as "absolute diffusion" or "single particle diffusion" (Csanady, 1973). To ensure that the number of degrees of freedom (i.e.,

number of drifters) remained constant as the Lagrangian time progressed, we used only drifters with trajectories that lasted at least 15 hours, and the statistics were calculated for only the first 15 hours since release time. The resulting single particle ensemble consists of 239 drifter trajectories.

We also calculated the single particle statistics for subsamples of the total ensemble. For example we compared the ensemble of releases from spawning sites with the ensemble of releases from nonspawning sites. We also compared the ensemble of trajectories from spawning time releases with the ensemble of trajectories from nonspawning time releases. There are two distinct seasons in Puerto Rico that have different winds. During the wet season, from July to December, the winds are often (but not always) calm (the mean "O" wind speed corresponding to this period is $2.4 \pm 1.9 m/s$). In the dry season the winds blow more strongly and steadily to the West (the mean "O" wind speed corresponding to this period is $5.4 \pm 1.5 m/s$). The ensemble of trajectories obtained during the wet season was compared with the ensemble of trajectories obtained during the dry season. The experiments performed during the summer of 1988 were not included in the single particle statistics for drifters with specified initial release conditions, but were included in the single particle statistics for all drifters (see page 21 for the reason).

4.2.2. The single particle statistics for all the drifter trajectories.

The variance of the single particle position is connected with the autocorrelation function $R(\tau)$, of the residual drifter velocity $u_r = u_r(t)$ (that is the velocity of the drifter at Lagrangian time t with respect to the average drifter velocity over all (here 239) drifter velocities at time t), via *Taylor's theorem* (equation (1.12)). Calculating $R(\tau)$ enables us to see the temporal structure of the turbulent velocities that cause cluster dispersion, in order to link the variance of the drifter position to flow kinematics. We only used the first 15 h of each of trajectory, giving $N = 30$ half hour time steps per

trajectory. In order to calculate the autocorrelation function $R(j)$ at the j^{th} lag we implemented the following discrete form of (1.11)

$$R(j)=[\sum_{m=1}^{M}\sum_{i=1}^{N-j} u_r(i,m)\,u_r(i+j,m)\,]/MN\,, \tag{4.4}$$

where $u_r(i,m)$ is the residual velocity at the i^{th} time step since release, of the m^{th} trajectory, and we average over M trajectories, and $N-j$ time steps. The type of averaging described by (4.4) is a form of time average, since we average over both trajectories of drifters released at different times and over the duration of a trajectory, and is based on the hypothesis that the turbulent field is stationary. The residual velocity was calculated by subtracting the average velocity $\langle u(i)\rangle$

$$u_r(i,m)=u(i,m)-\langle u(i)\rangle\,, \tag{4.5}$$

where

$$\langle u(i)\rangle = [\sum_{m=1}^{M} u(i,m)\,]/M\,, \tag{4.6}$$

and $u(i,m)$ is the velocity at the i^{th} time step of the m^{th} drifter. In formula (4.4), we divided by MN, instead of $M(N-j)$, in order to correct for the bias at large lags (Beauchamp and Yuen, 1979; p 186).

The autocorrelation function R along the x axis (along-shore) is plotted in Figure 4-1. Dashed lines in this Figure represent the best fit exponential function. An exponential autocorrelation function arises from a first order Markov process, for which $u(t)$ at time intervals Δt is given by

$$u(t+\Delta t)=e^{-\gamma\Delta t}\,u(t)+\xi(t)\,. \tag{4.7}$$

where $\xi(t)$ is a random variable uncorrelated with $u(t)$ and earlier values of u. For a first order Markovian process $R(\tau)=e^{-\gamma\tau}$. The integral $\int_0^\infty R(\tau)d\tau$ converges to a time scale $\tau^*=\frac{1}{\gamma}$ and the single particle diffusivity grows as

$$\frac{1}{2}\frac{d\langle x^2\rangle}{dt}(t)=\langle u_r^2\rangle\int_0^t R(\tau)d\tau=\frac{\langle u_r^2\rangle}{\gamma}(1-e^{-\gamma t})\,. \tag{4.8}$$

For $t\gg\frac{1}{\gamma}$ this approximately reduces to Fickian diffusion and the variance $\langle x^2\rangle$ grows approximately proportional to time. Fickian diffusion corresponds to

$R(\tau)$ becoming equal to zero after some short time. Integrating the area under R for the x component of motion (this area being equal to the rate of growth of variance along the x axis, as can be seen by equation (1.10)) gives an integral time scale of $\tau_x^* = 2.5\,h$, whereas the area under the exponential fit is $\frac{1}{\gamma} = 2.3\,h$, which is smaller. Clearly, the variance along x axis grows faster than time raised to the power of 1, as happens in the Fickian case of an exponentially dropping autocorrelation. We can indeed see in Figure 4-3, where the variance along the x axis is plotted as a function of time since release on a log-log scale, that the variance along the x axis grows proportional to time raised to a power of 1.5 (a line of slope 1.5 is included in the plot). Thus the dispersion along the x direction is faster than either Fickian or first order Markov process. Sanderson and Booth (1991) show that variance can grow proportional to $t^{1.5}$ for fractional Brownian motion. The integral time scale is undefined for fractional Brownian motion because the integral of the autocorrelation function does not converge. However, the autocorrelation functions in Figures 4-1, 4-2 do drop rapidly with increasing lag, and so we can locally define an integral time scale and eddy diffusivity (calculated by equation (1.14)) that applies over the experiment's duration (but not for longer time scales). On this basis the eddy diffusivity for the single particle motion in the x direction is $K_x^* = 61\ m^2/s$.

The autocorrelation function along the y axis (across-shore) is plotted together with its best fit exponential function in Figure 4-2. The autocorrelation function for the y component of single particle velocity falls off faster than for a first order Markov process, and actually becomes slightly negative at large lags. Thus the variance in the cross-shore (y) direction grows as t raised to a power of 1 or perhaps slightly less than 1 (see Figure 4-4 of the variance along the y axis as function of time since release on a log-log scale). It would appear that dispersion in the y direction may be characterized as being approximately Fickian with some slight convergent process tending to oppose dispersion. The Eulerian correlation R_E of the turbulent velocity component along the y axis,

for a two dimensional isotropic turbulent flow field having a mean motion along the x axis, has also been reported to achieve negative values by many authors (Monin and Yaglom, 1975; p118). Monin and Yaglom (1975) indicate that the Eulerian correlation functions of the turbulent velocity components along the two axes are related via the continuity equation. This type of argument might be extended in the case of our Lagrangian autocorrelation function as follows. The turbulent flow along the x axis is probably divergent, as implied by the above mentioned 1.5 power low for the growth of the variance with time. This results in the turbulent flow along the y axis being convergent, if the continuity equation for our two-dimensional incompressible turbulent velocity field is to be valid. The diffusion along the y axis (with respect to the absolute motion) is not continuous; it is being interrupted by convergences, and this results in the turbulent velocity component of a particle along the y axis at some time being on average opposite to the turbulent velocity component of the same particle at a later time, i.e., to negative autocorrelation. Integrating the area under the experimentally obtained autocorrelation function gives an integral time scale $\tau_y^* = 1.1\ h$, whereas the best fit exponential function gives $\frac{1}{\gamma} = 1.2\ h$.

The single particle eddy diffusivity for dispersion in the y direction is $K_y^* = 5.4\, m^2/s$. At this point, before speculating about the eddy diffusivities along the two axes, we will compare them with the gross diffusivities G^*. The gross diffusivities can be defined from changes in variance (σ_x^*, σ_y^*) of the single particle position over the duration T of the experiment

$$G_x^* = \frac{1}{2}\frac{(\sigma_x^*)^2(t=T) - (\sigma_x^*)^2(t=0)}{T} \qquad (4.9)$$

$$G_y^* = \frac{1}{2}\frac{(\sigma_y^*)^2(t=T) - (\sigma_y^*)^2(t=0)}{T}$$

From the values in Figures 4-3, 4-4 these diffusivities are $G_x^* = 111\, m^2/s$ and $G_y^* = 5\, m^2/s$ (note that the values $(\sigma_x^*)^2(t=0) = 122000 m^2$, $(\sigma_y^*)^2(t=0) = 32810 m^2$,

are substantially larger than zero, due to the variability (from experiment to experiment) of the drifter release positions). The gross diffusivities G^* are of the same order of magnitude as the eddy diffusivities K^* of the single particle motion. The difference in the along-shore direction by a factor of 2 between K^* and G^* can be attributed to partial lack of stationarity and homogeneity for the single particle statistics in the area of the experiment. The single particle eddy diffusivity for dispersion in the y direction is an order of magnitude less than the eddy diffusivity in the along-shore direction. Partly the greater eddy-diffusivity in the along-shore direction is caused by the integral time scale being longer for the x component of motion than for the y component of motion. But mostly the increased dispersion in the along-shore direction is caused by residual single particle kinetic energy in the along-shore direction $\langle u_r^2 \rangle = 0.0066\, m^2/s^2$ being much greater than that $\langle v_r^2 \rangle = 0.0014\, m^2/s^2$ in the across shore direction.

In the previous chapter we saw that the currents were largely driven by along-shore wind stress and opposing along-shore pressure gradients. The mean current is, therefore, predominantly in the along-shore direction. Fluctuations in the wind stress cause the along-shore current to vary, and sometimes to reverse. This in turn, results in the x component of residual single particle kinetic energy $\langle u_r^2 \rangle$ being much greater than the y component of the single particle kinetic energy $\langle v_r^2 \rangle$.

The residual single particle motion in the along-shore direction u_r is largely associated with fluctuations in the wind forced motion. Since the wind fluctuates with a wide range of time scales and has most of its energy in the diurnal band, it is not surprising that $R_x(\tau)$ for the along-shore motion (Figure 4-1) is substantially above zero at large lags. The relatively rapid rate at which $R_x(\tau)$ falls initially can be ascribed mostly to fluctuations of along-shore particle velocity associated with the variable bathymetry and flow around

exposed and semi-exposed reefs. The variability of the across-shore single particle motion is more attributable to the variable bathymetry and reefs. For example if reefs and bumps in the bottom have length scales of $\approx 300m$ and the typical along-shore current is $0.08m/s$ then the time scale for the across-shore current variability would be $300/0.08 \approx 1\,h$. The across-shore current has no long time scale process driving it. Thus the integral time scale of the across-shore velocity is less than that of the along-shore velocity. The angle of orientation of the principal axis of the single particle dispersion (anticlockwise from the x-axis), along with the mean velocities along the two axes are all plotted as a function of time since release in Figure 4-5. Clearly the major and minor axes of dispersion approximately coincide with the x and y axes respectively and there is a tendency for the flow and the principle axis of dispersion to orient parallel to the coastline as can be seen in Figure 4-6 of the mean trajectory. From the ensemble averaged velocity plots of 4-5 we see that the along-shore component of velocity decreases with increasing time since release as can be seen in Figure 4-5. This probably is because the along-shore wind reduces after having reached its peak at around noon, as can be seen in Figure 3-4.

Figure 4-1: *The autocorrelation of the x-component of the single particle velocity as a function of lag (solid line), and its best fit exponentially dropping function (dashed line).*

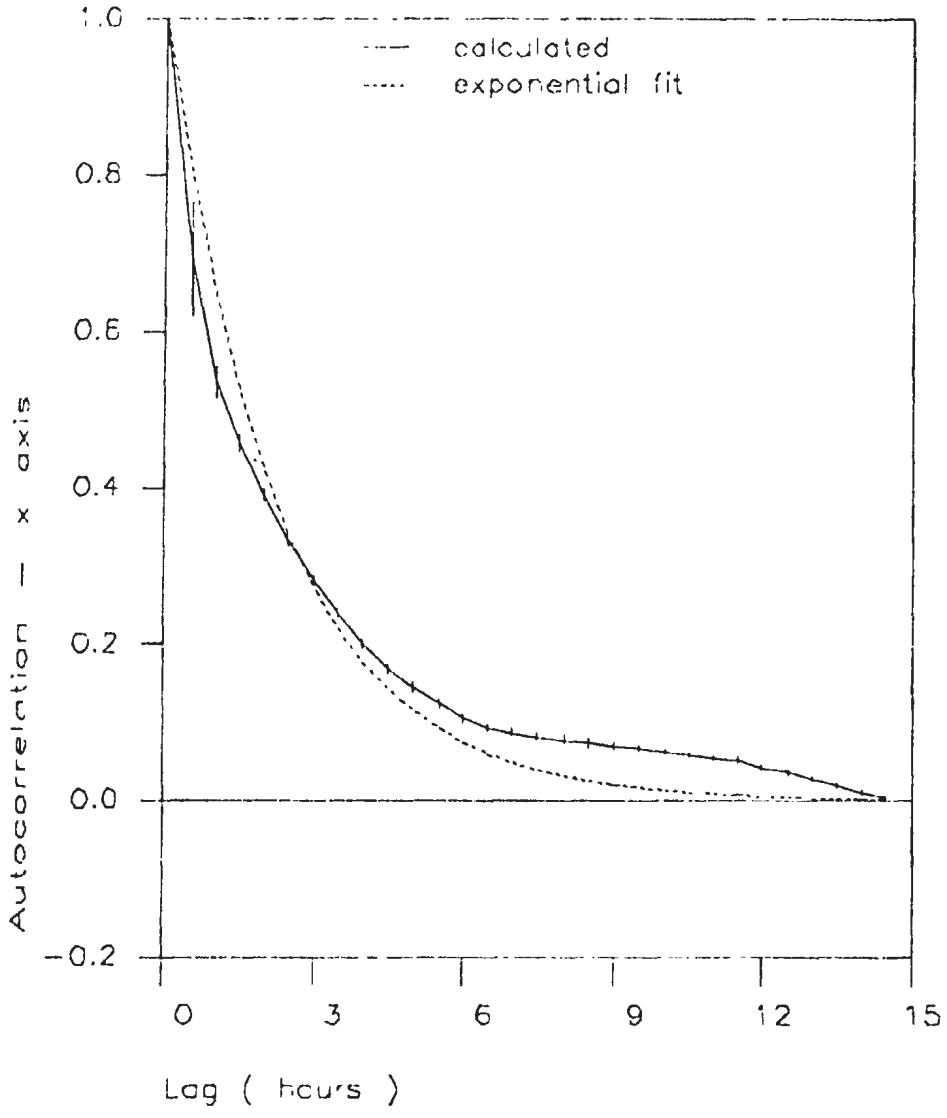

Figure 4-2: *The autocorrelation of the y-component of the single particle velocity as a function of lag (solid line), and its best fit exponentially dropping function (dashed line).*

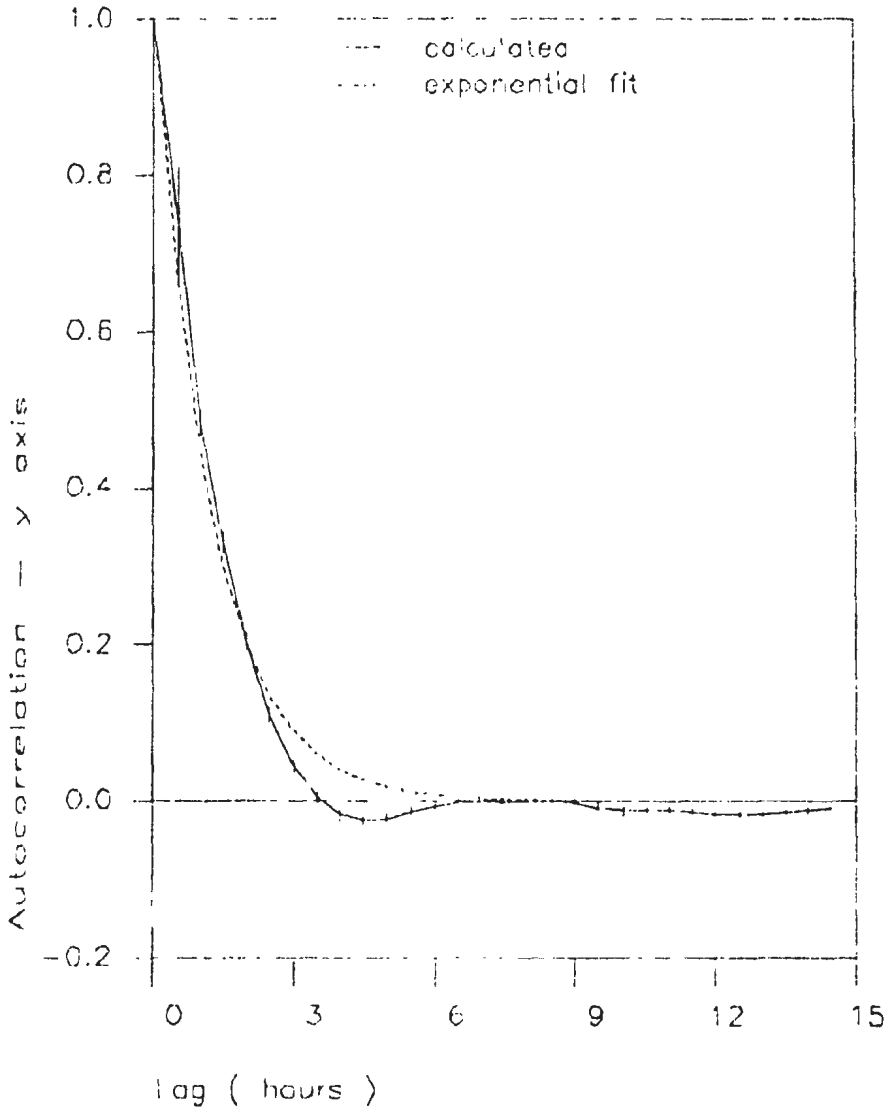

Figure 4-3: *The variance (stars) of the x-coordinate of the single particle position as a function of time since release on a log-log scale. The solid straight line of slope* 1.5 *is the one that best fits the variance, and indicates that the variance grows as time raised to the power of* 1.5.

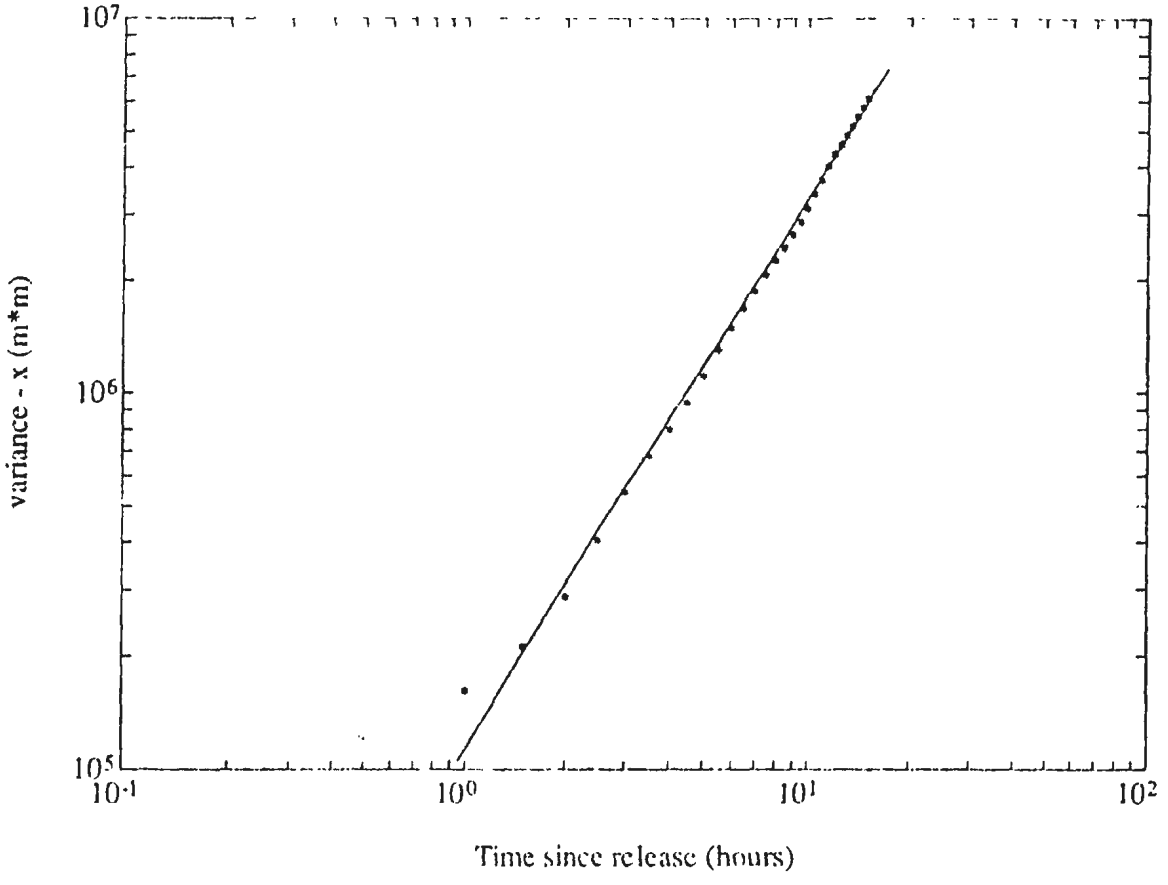

Figure 4-4: *The variance (stars) of the y-coordinate of the single particle position as a function of time since release on a log-log scale. The solid straight line of slope 1 is the one that best fits the variance, and indicates that the variance grows as time raised to the power of 1.*

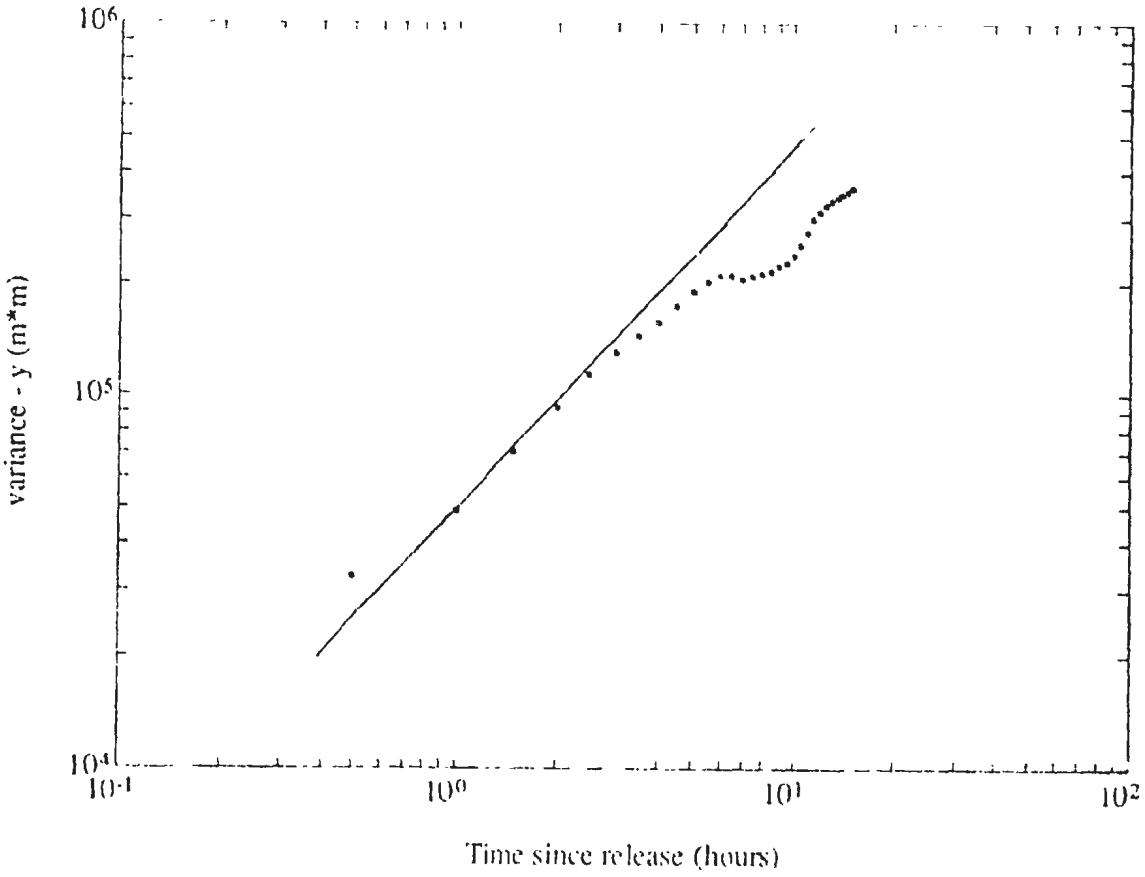

Figure 4-5: *The ensemble averaged (over all drifters) velocity and orientation of the principal axis of dispersion as functions of time since release.*

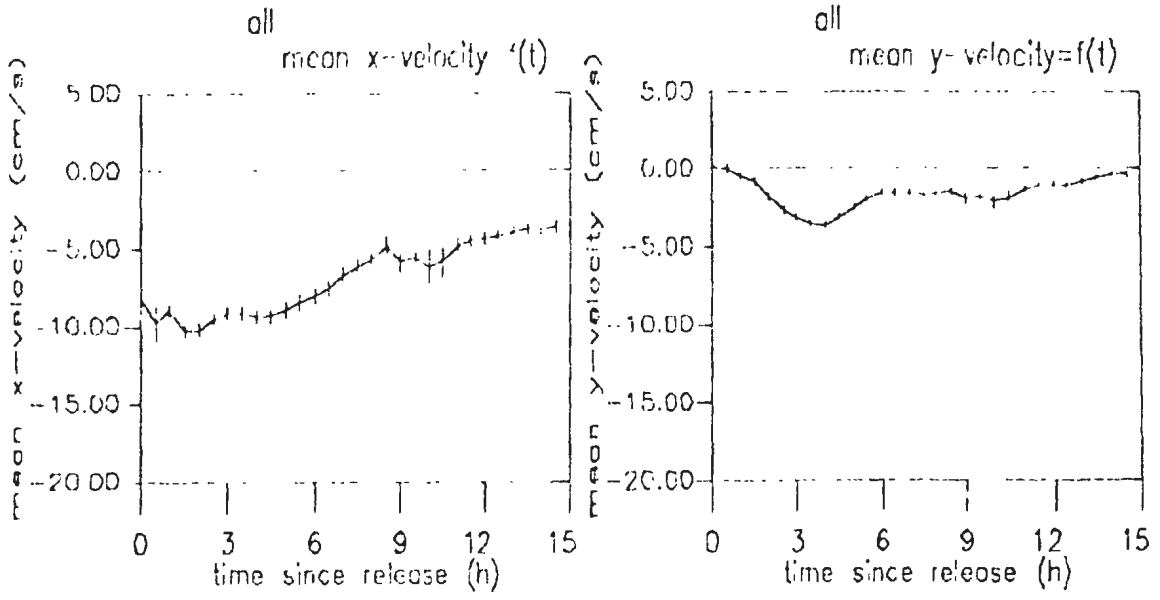

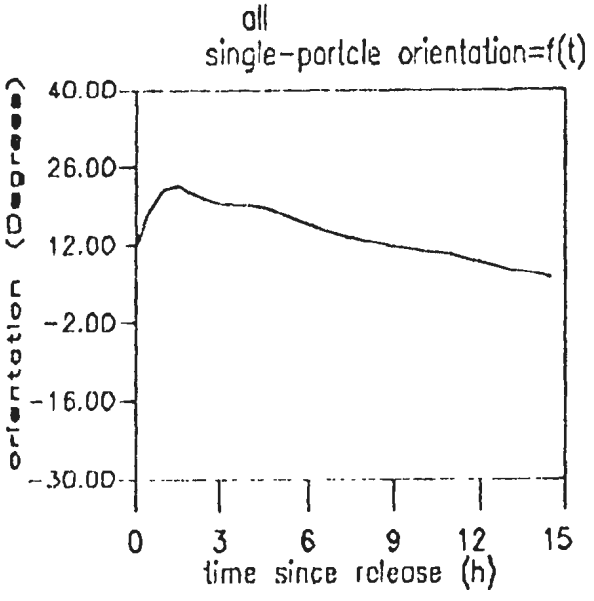

Figure 4-6: *The ensemble averaged (over all drifters) drifter trajectory. The standard deviations about the mean drifter position are plotted for every 2.5 hours since release. They are in the form of crosses centered at the mean position.*

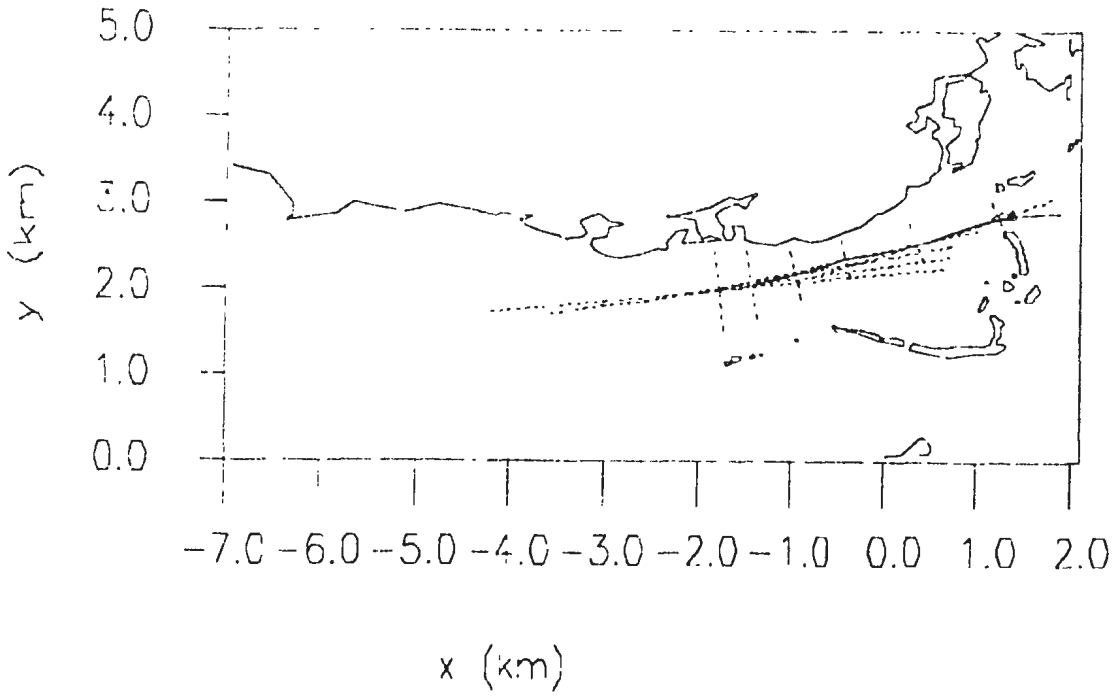

4.2.3. Comparing the single particle statistics during wet and dry seasons.

The wet season lasts from July to December and the dry season lasts from January to June. The winds tend to be stronger and towards the West during the dry season. In the wet season the wind is still usually westwards, but is generally weaker and sometimes becomes calm or reverses to the East.

In Figure 4-7 we have plotted the along-shore (x-axis) and across-shore (y-axis) ensemble averaged velocities, as functions of Lagrangian time for the wet season and the dry season. Here we see that value of the dry season along-shore velocity ranges from $-15cm/s$ to $-7cm/s$ whereas the wet season along-shore velocity ranges from $-6cm/s$ to $+0cm/s$. Negative along-shore components of velocity correspond to westwards flow, and the fact that we don't have positive (eastwards) mean along shore velocities during the wet season, when most of the (eastwards) reversals happened, is because the times (since release) of eastwards flow episodes are randomly distributed throughout the duration of an experiment (see T_{accum} column of Table 3-2). Thus the positive along-shore velocities are not all concentrated in a narrow time (since release) band, and thus they cannot prevail in the mean value. The particle speed is less during the wet season than during the dry season. This is in accordance with weaker winds during the wet season than during the dry season. Neither the wind nor the current are exactly parallel to the along-shore (x) axis. Thus the cross-shore velocity is also larger during the dry season than during the wet season. The cross-shore velocities during the wet season ($-6cm/s$ to $-1cm/s$) and dry season ($-2cm/s$ to $-1cm/s$) are smaller than the corresponding along-shore velocities due to the mostly along-shore orientation of the mean flow. In Figure 4-8 we see that trajectories during the dry season reach much further West than during the wet season. Consequently eggs will spend much more time in shallow reefs during the wet season than during the dry season. Predation is likely to be greater in shallow reef areas.

The single particle dispersion for each of the two cases, is depicted in Figure 4-9. Here we can see that the variance along both the major and minor axes of dispersion grows faster with time during the wet season than during the dry season. The orientation of the major axis of dispersion is more along-shore during the dry season than during the wet season. In the dry season the wind is strong, oriented close to the along-shore direction and generally westwards. In contrast, during the wet season the wind is generally weaker and very variable. It can be westwards, calm, and sometimes even eastwards. This results in the current variability (from experiment to experiment), and therefore also in the single particle dispersion being larger for the wet season than for the dry season.

Figure 4-7: ***The ensemble averaged drifter velocity as a function of time since release during the wet season (left) and the dry season (right).***

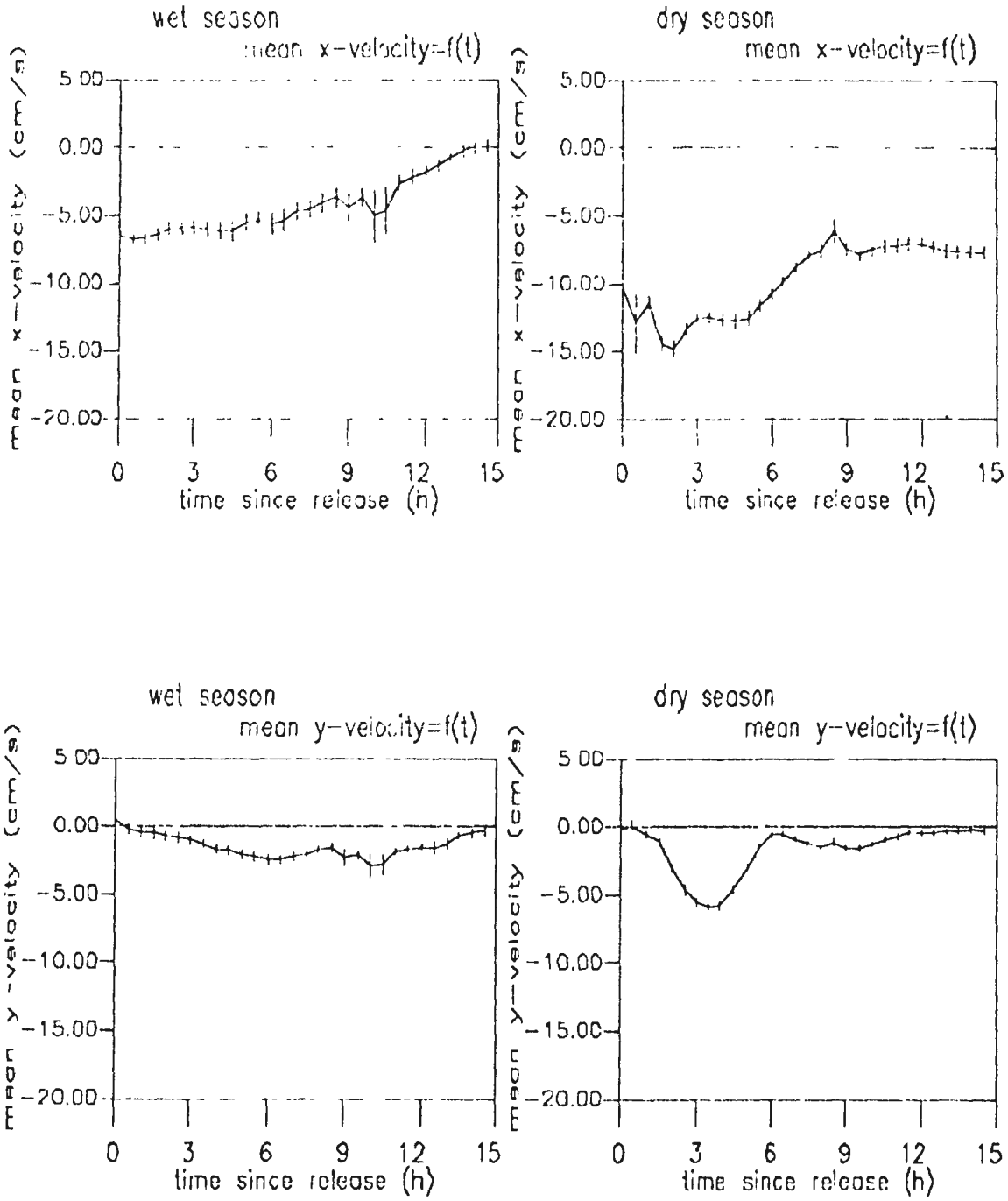

Figure 4-8: *The ensemble averaged drifter trajectory during the dry season (top) and the wet season (bottom). The standard deviations about the mean drifter position along the major and minor axes of dispersion are plotted every 2.5 hours since release. They are in the form of crosses centered at the mean position.*

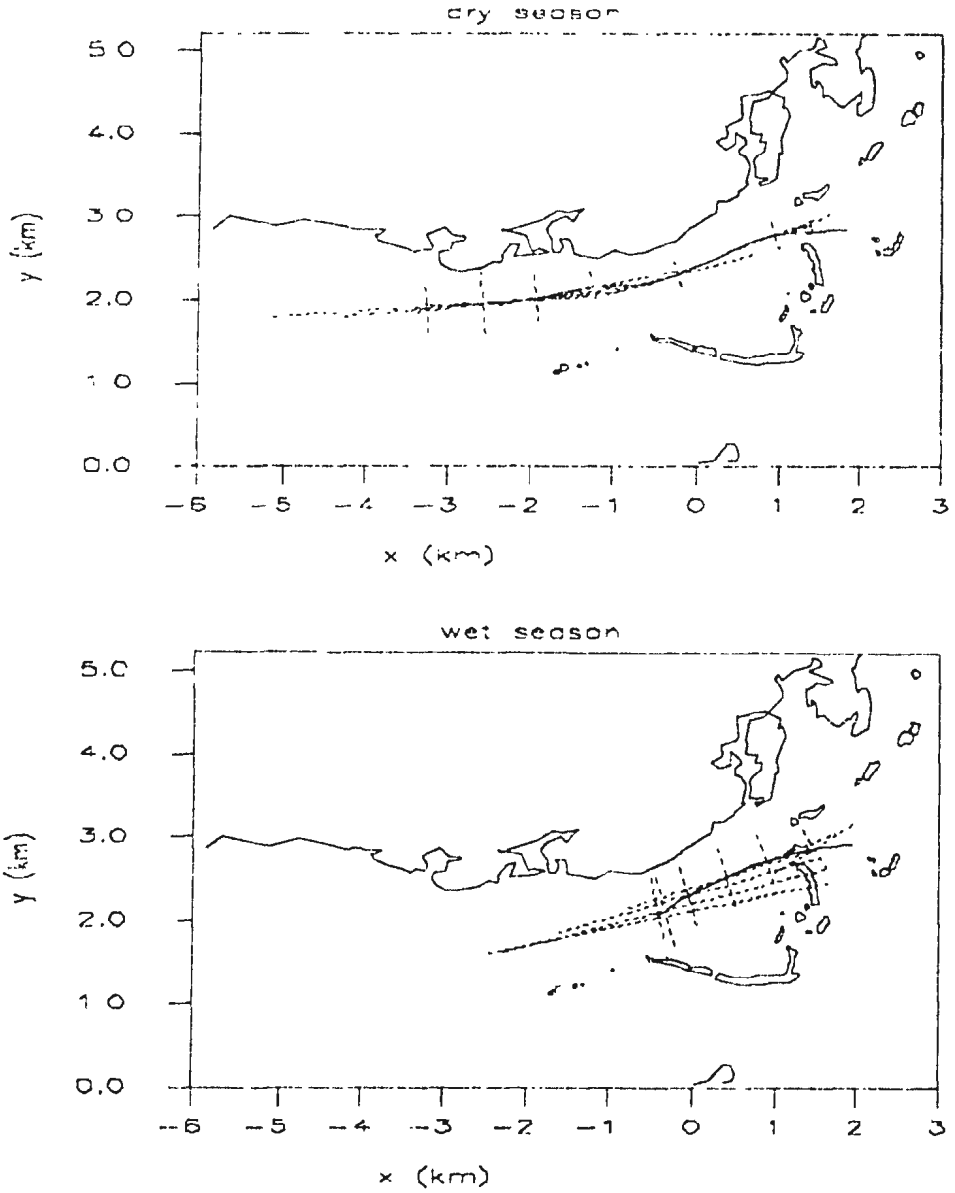

Figure 4-9: *The single particle dispersion (i.e., variance var-X along the major axis of dispersion, var-Y along the minor axis of dispersion and orientation of the major axis of dispersion) as a function of time since drifter release during the wet season (left) and the dry season (right).*

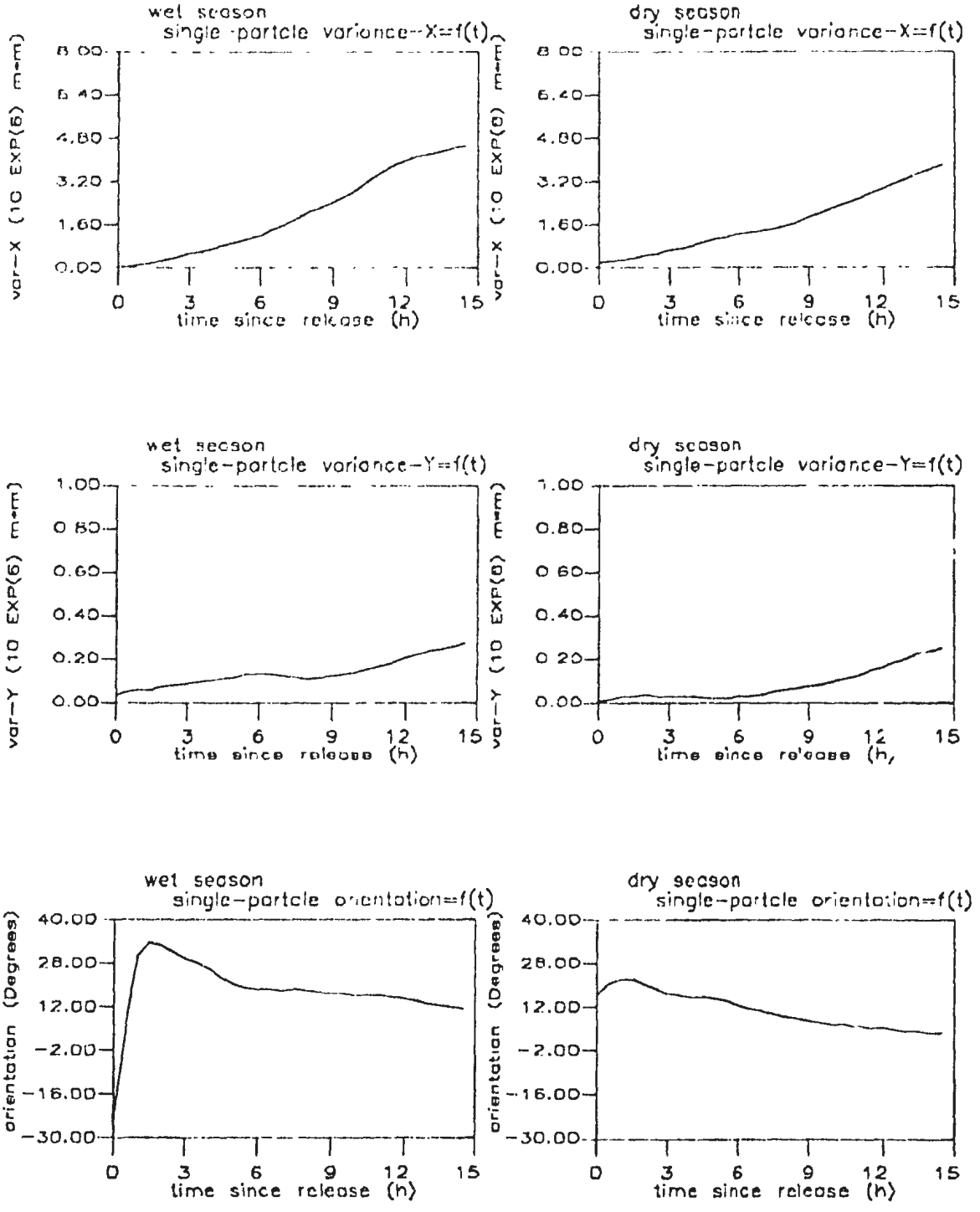

4.2.4. Dependence of the single particle statistics on the release time.

The study species is observed to spawn only at around noon (1200 *h* to 1400 *h*). Thus we did drifter deployments at around 1300 *h*. Another ensemble of deployments at a nonspawning time (0700 *h*) was also made. In chapter 3 we obtained the mean wind velocity as a function of the hour of the day, over each of the three available time series of wind velocity,"P", "O", and "M" (Figures 3-4, 3-5). The "O" wind velocity data have been considered as the most reliable wind data (see page 26 for the reason) and we could see in Figure 3-4 that the "O" wind achieves a peak x-component (approximately along-shore) between 1200 *h* and 1600 *h*. The y component of the "O" wind is similar in magnitude to x component of wind during the most of the day, except from the time interval between 0900 *h* and 1800 *h*, during which the x component of wind is four to five times larger than the y component. In chapter 3 we saw that the currents were correlated to the wind. Thus we expect the currents and drifter trajectories to be a function of the time of drifter deployment.

Figure 4-10 shows the ensemble averaged drifter velocity, as a function of time since release, for spawning time (70 trajectories) and nonspawning time deployments (42 trajectories). The along-shore component of velocity for nonspawning time deployments lags that of the spawning time deployments by 5 *h*. Apart from this time lag, which corresponds to the difference in deployment times, the along-shore component of velocity does not differ significantly between nonspawning time deployments and spawning time deployments.

The across-shore velocity partly depends on the wind, but it also depends on the orientation of channels and reefs. Thus the across-shore velocity from nonspawning time releases differs from that of spawning time releases in a way that does not just amount to a 5 *h* lag. We see that the across-shore velocity for both the spawning time and the nonspawning time deployments tends to have

an off-shore (negative) direction. However, the absolute value of the off-shore (negative) velocity for the spawning time deployments is generally larger than absolute value of the off-shore velocity for nonspawning time deployments, especially at the first five hours since release. This difference between the off-shore mean velocities of the two categories of deployments results in the mean trajectory for nonspawning time deployment going closer to the shore than the mean trajectory for the spawning time deployment as can be seen in Figure 4-11. There is more shallow reef close to shore. Also, the near shore zone has mangroves, which make a good habitat for species that might prey on eggs. Eggs released at nonspawning time would, therefore be subject to more predation than eggs released at spawning time. The standard deviation of drifter positions is also plotted in figure 4-11, in the form of crosses centered at the mean position, for every $2.5h$ since release. Clearly some releases at spawning time might go as close to shore as some of the nonspawning time releases. On average, however, the spawning time releases do not have trajectories as near to the coastline as the nonspawning time releases.

Figure 4-12 shows that the dispersion of the drifters is slightly greater for the nonspawning time deployment than for the spawning time deployment. This might be of some biological importance if predation is dependent upon the egg density. The principal axes of dispersion are oriented similarly for nonspawning time and spawning time deployments, except for the first half hour of the trajectory.

Figure 4-10: ***The ensemble averaged drifter velocity as a function of time since release at the spawning time deployment (left) and the nonspawning time deployment (right).***

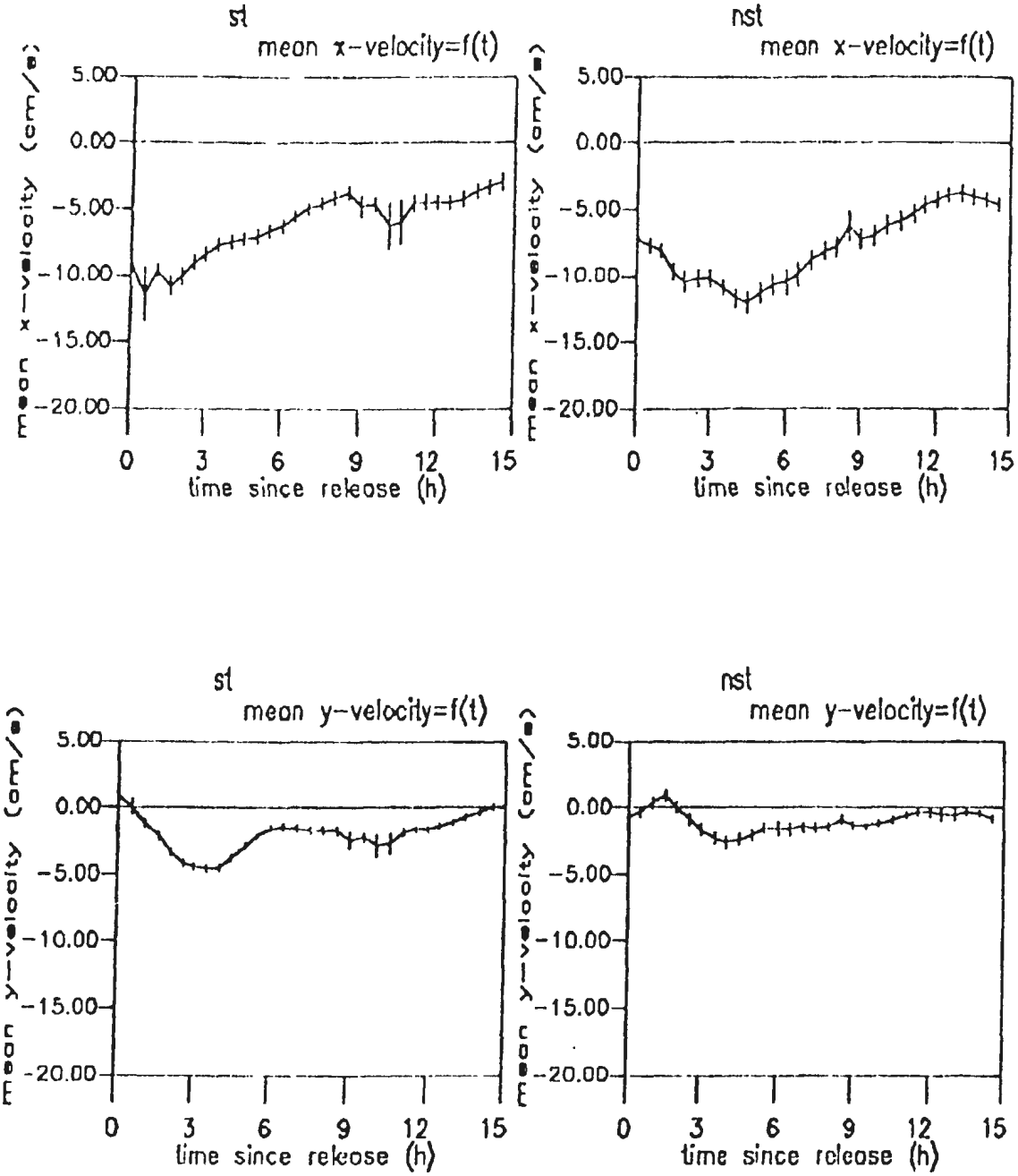

Figure 4-11: *The nonspawning time (top) and spawning time (bottom) ensemble averaged trajectories.The standard deviations about the mean drifter position along the major and minor axes of dispersion are plotted for every 2.5 hours since release. They are in the form of crosses centered at the mean position.*

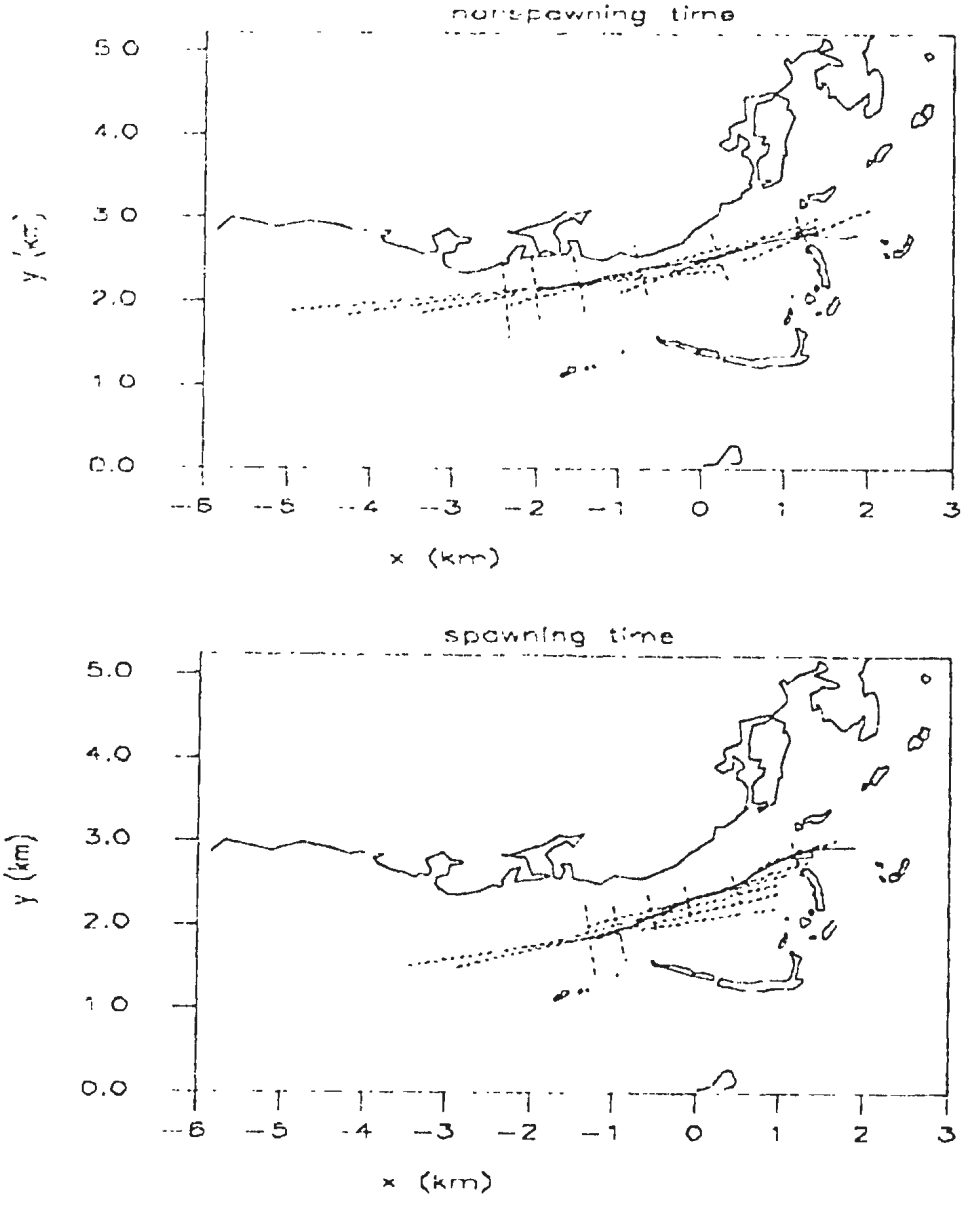

Figure 4-12: *The single particle dispersion (i.e., variance var-X along the major axis of dispersion, var-Y along the minor axis of dispersion and orientation of the major axis of dispersion) as a function of time since drifter release, at the spawning time (left) and the nonspawning time (right).*

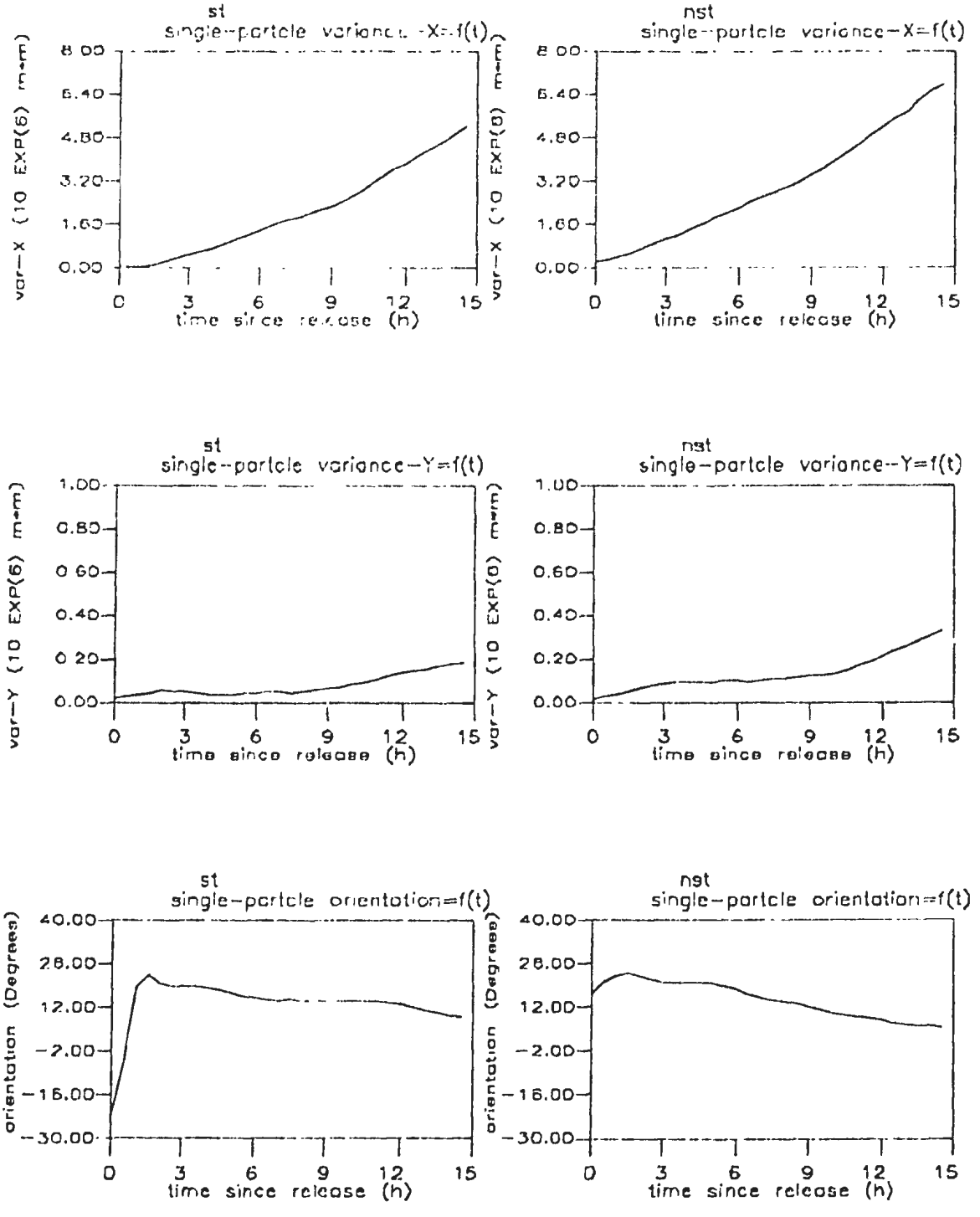

4.2.5. Dependence of the single particle statistics on the release site

Each experiment was initiated by the release of dye at the actual spawning / nonspawning sites and times. The dye was tracked for approximately 1 h, and then replaced by a cluster of drifters. We do not have the dye data, and so can not determine if the dye tracks and dispersion were dependent upon release site. We do, however, have initial drifter positions corresponding to the first trisponder fix, which are typically located near the drifter release positions (there is a slight deviation between the drifter release positions and the initial drifter positions). The drifters were released in a configuration that represented the shape and the location of the dye patch.

As already mentioned, (see page 21) we used two times for dye releases, the spawning and nonspawning time, and we also used two spawning sites ("S1", "S2") and two nonspawning sites ("NS1", "NS2"), yielding a total of eight categories of initial conditions for dye - drifter trajectories. We calculated the mean initial position of the drifters and the standard deviation about this mean, over all the drifters of each of the 8 above categories. The results are plotted in Figures 4-13, 4-14. In these Figures, the standard deviations of the drifter release position along the x and y axes are plotted in the form of crosses centered at the mean drifter release position, and the drifter release positions are also plotted in the form of dots. We can see that, at spawning time, the release position of drifters corresponding to spawning site "S1" is statistically distinct from the release position of drifters corresponding to spawning site "S2", in the sense that, the crosses illustrating the mean drifter release position and the standard deviation of it for the two categories, do not overlap. Apart from this, the crosses corresponding to the other six categories do overlap. We can therefore conclude that, generally, the initial drifter release positions, corresponding to the eight categories of initial conditions of dye release, are not statistically distinct.

The mean drifter trajectories for each of the eight categories are plotted in Figures 4-15, 4-16, 4-17, 4-18. Again we see that deployments at spawning times are different from deployments at nonspawning times, in that the nonspawning time trajectories tend to be closer to the shore. It is not clear that deployments at spawning sites are different from deployments at nonspawning sites. However, the spawning time release at nonspawning site 2 shows less dispersion and mean motion than the other cases. As a final check we divided the drifter trajectories into an ensemble that originated with dye releases from a spawning site and another ensemble that originated with dye releases from a nonspawning site. Figures 4-19 and 4-20 show that the mean velocity and single particle dispersion are largely independent of whether the release site was a spawning site or a nonspawning site. There may, however, be a slight tendency for spawning site releases to disperse more quickly than nonspawning site releases.

Figure 4-13: *The mean drifter release positions for each of the four dye release sites (indicated by stars) at spawning time. The little blobs indicate drifter release positions. The crosses are centered at the mean drifter release position and the cross-arms have lengths equal to the standard deviation σ_x, σ_y of the drifter release position about the mean drifter release position.*

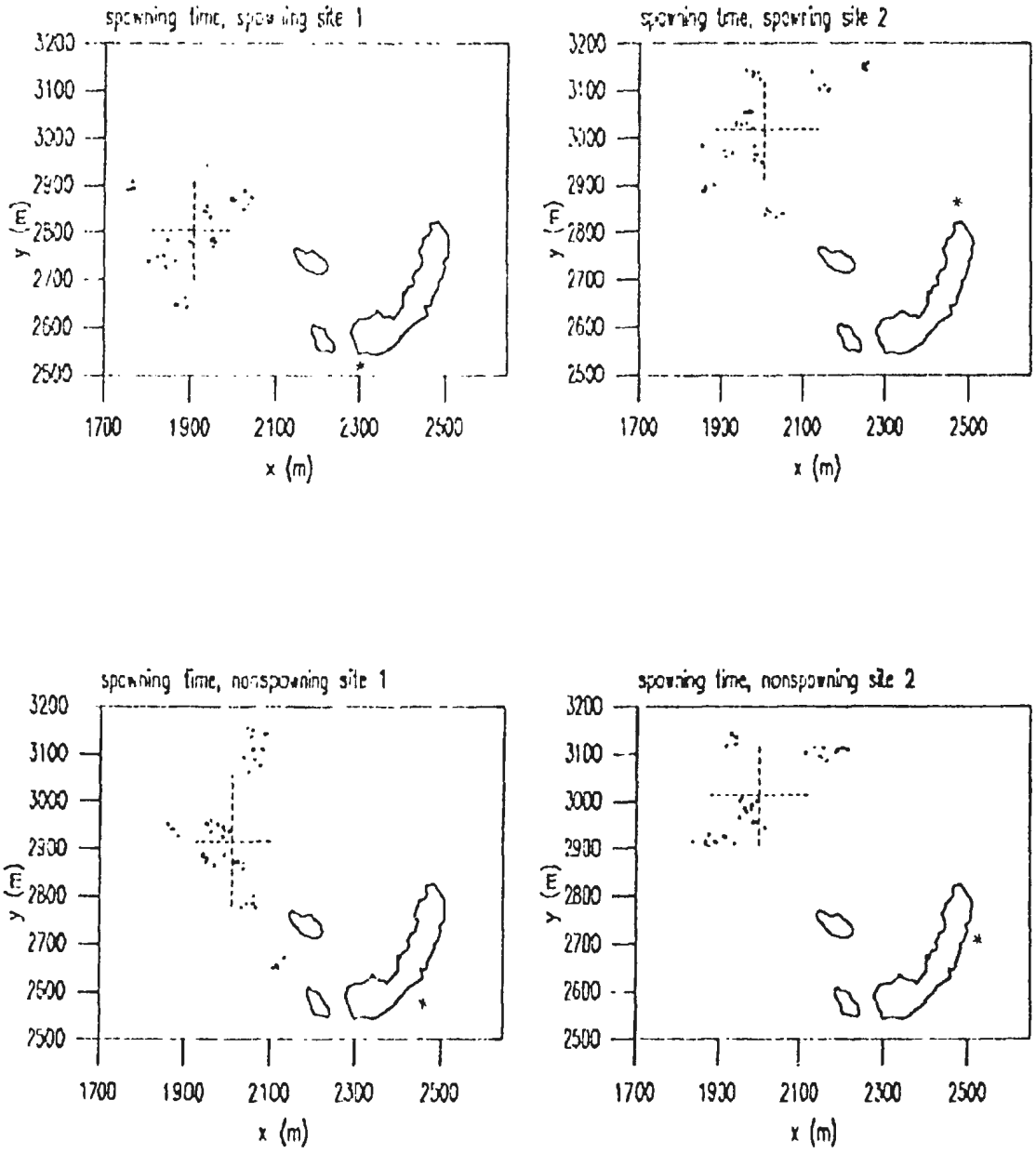

Figure 4-14: *The mean drifter release positions for each of the four dye release sites (indicated by stars>) at nonspawning time. The little blobs indicate drifter release positions. The crosses are centered at the mean drifter release position and the cross-arms have lengths equal to the standard deviation σ_x, σ_y of the drifter release position about the mean drifter release position.*

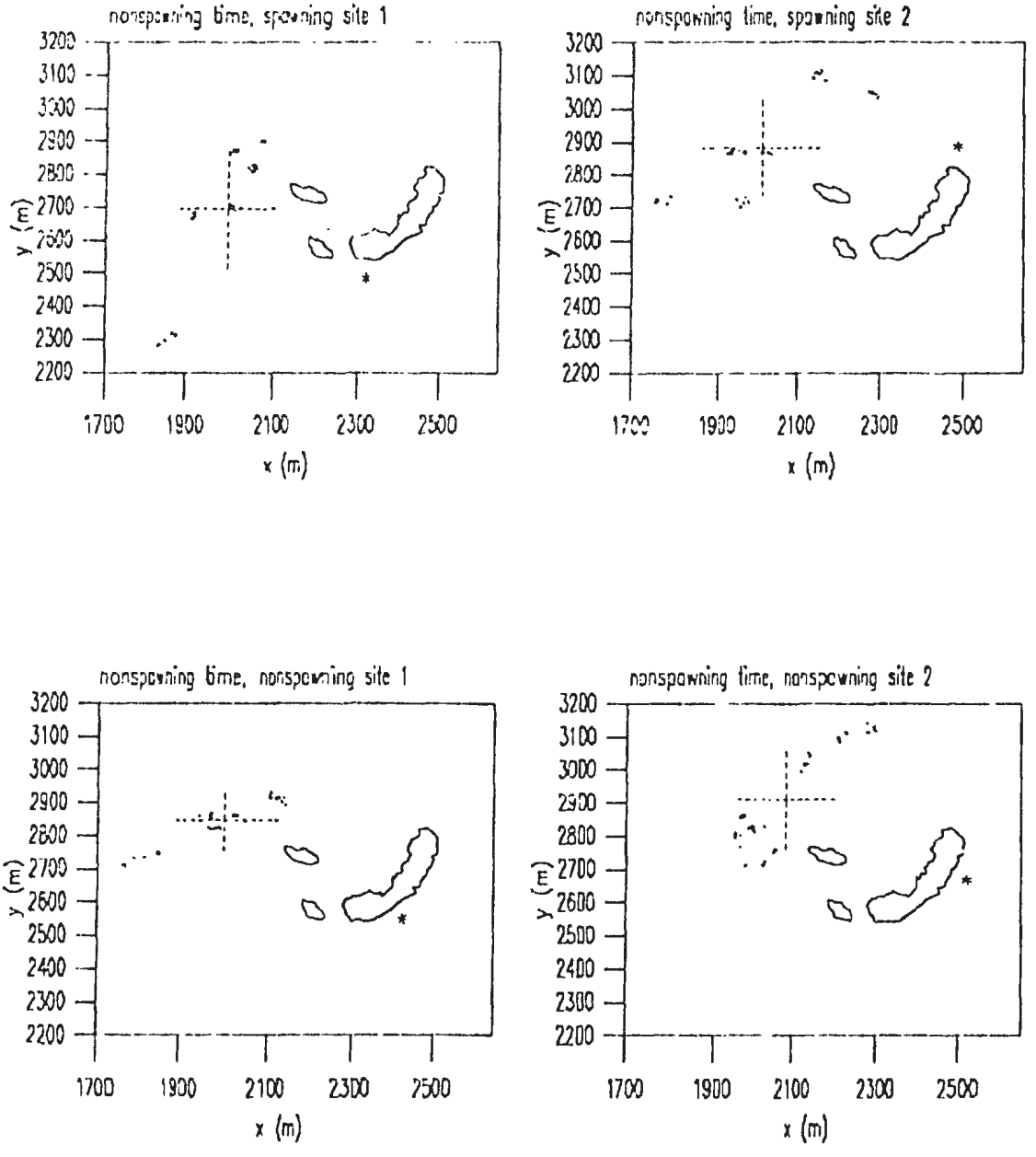

Figure 4-15: *The mean trajectories for the spawning sites at spawning time. The standard deviations about the mean drifter position along the major and minor axes of dispersion are plotted for every 2.5 hours since release. They are in the form of crosses centered at the mean position.*

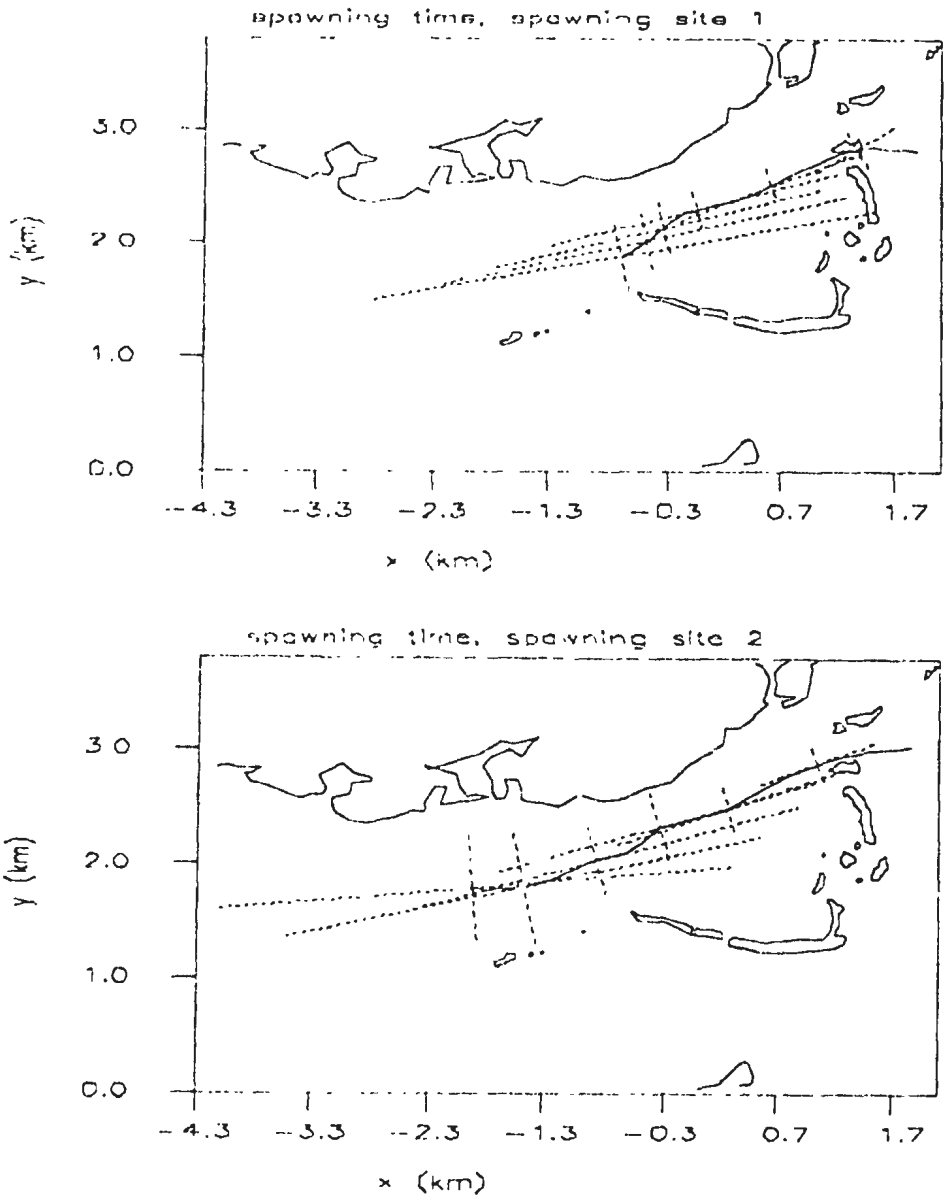

Figure 4-16: *The mean trajectories for the nonspawning sites at spawning time. The standard deviations about the mean drifter position along the major and minor axes of dispersion are plotted for every 2.5 hours since release. They are in the form of crosses centered at the mean position.*

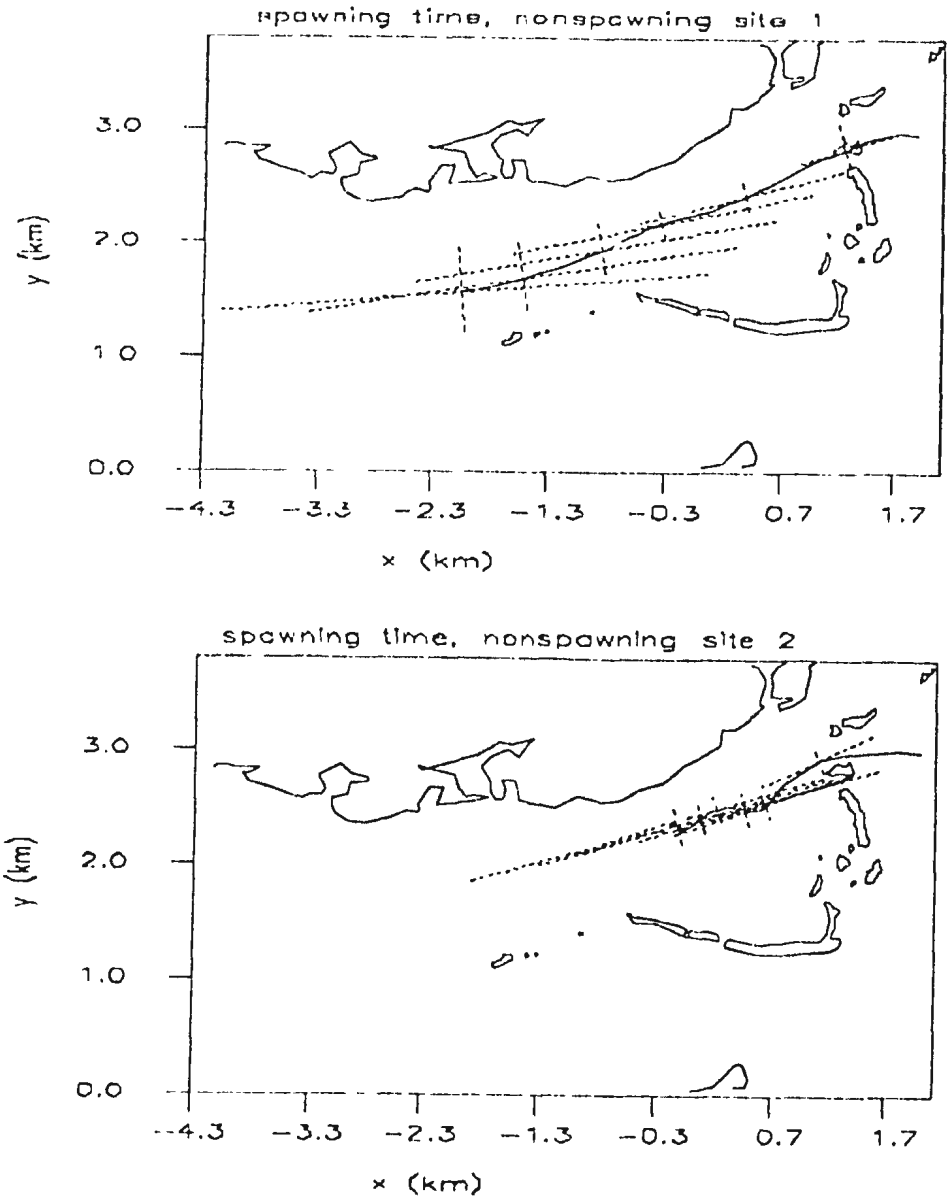

Figure 4-17: *The mean trajectories for the spawning sites at nonspawning time. The standard deviations about the mean drifter position along the major and minor axes of dispersion are plotted for every 2.5 hours since release. They are in the form of crosses centered at the mean position.*

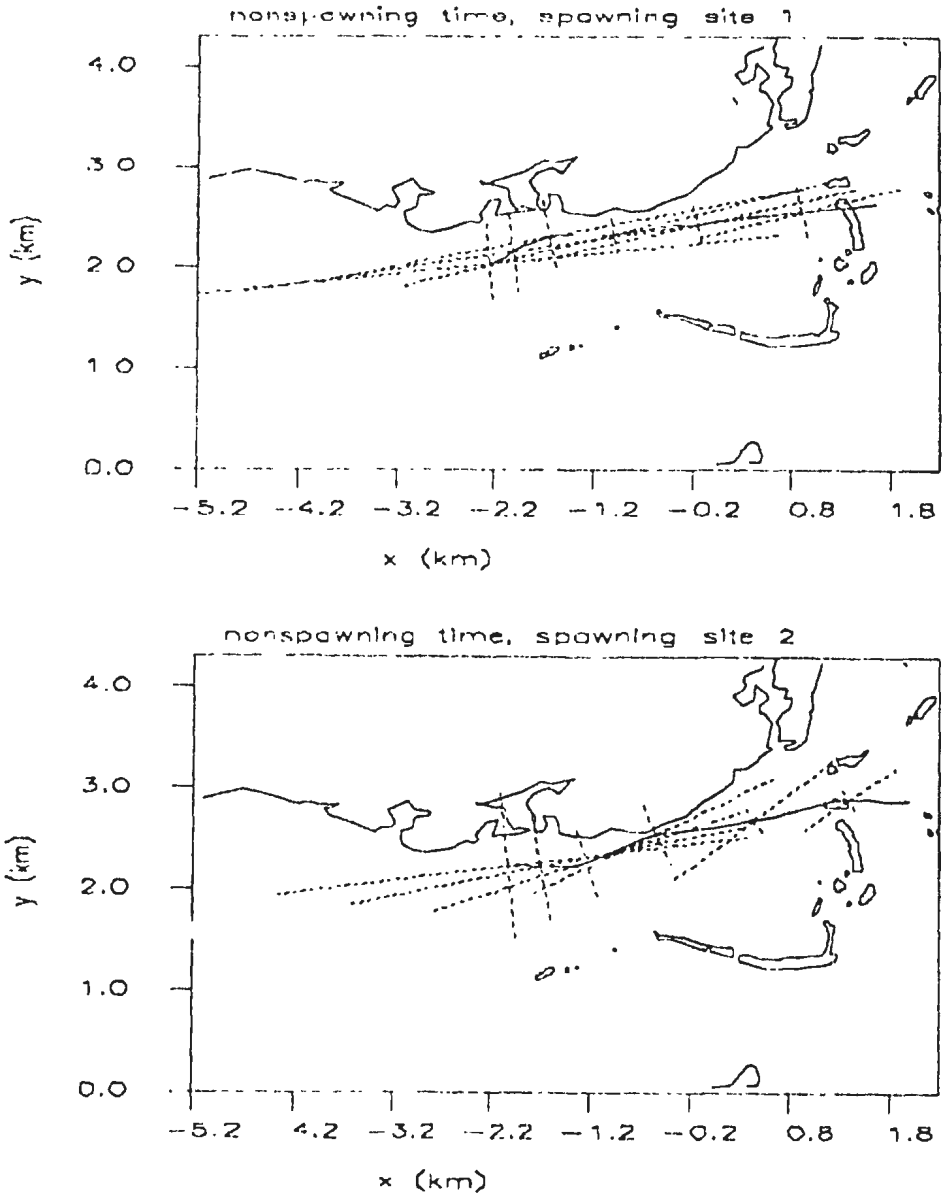

Figure 4-18: *The mean trajectories for the nonspawning sites at nonspawning time. The standard deviations about the mean drifter position along the major and minor axes of dispersion are plotted for every 2.5 hours since release. They are in the form of crosses centered at the mean position.*

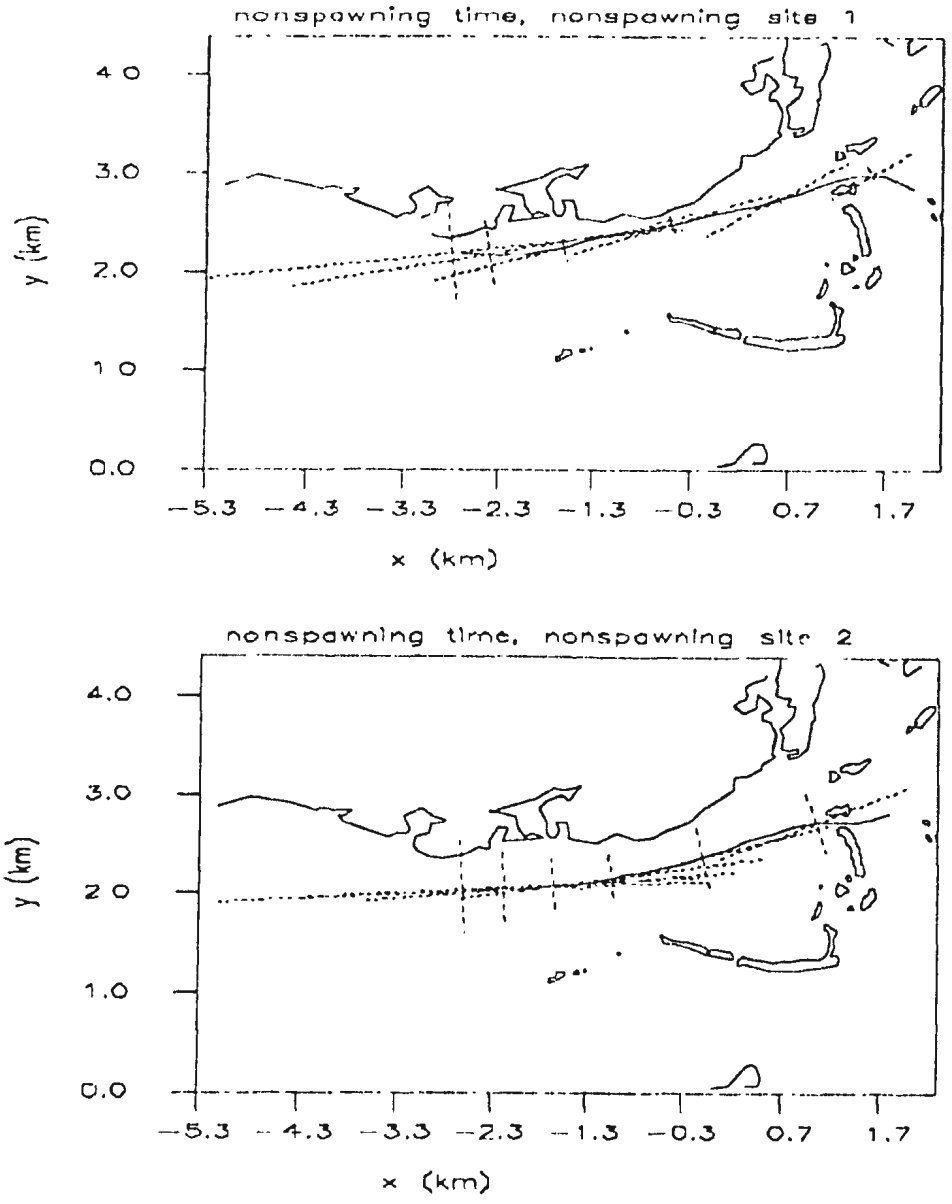

Figure 4-19: ***The ensemble averaged drifter velocity as a function of time since drifter release, from the spawning site (left) and the nonspawning site (right).***

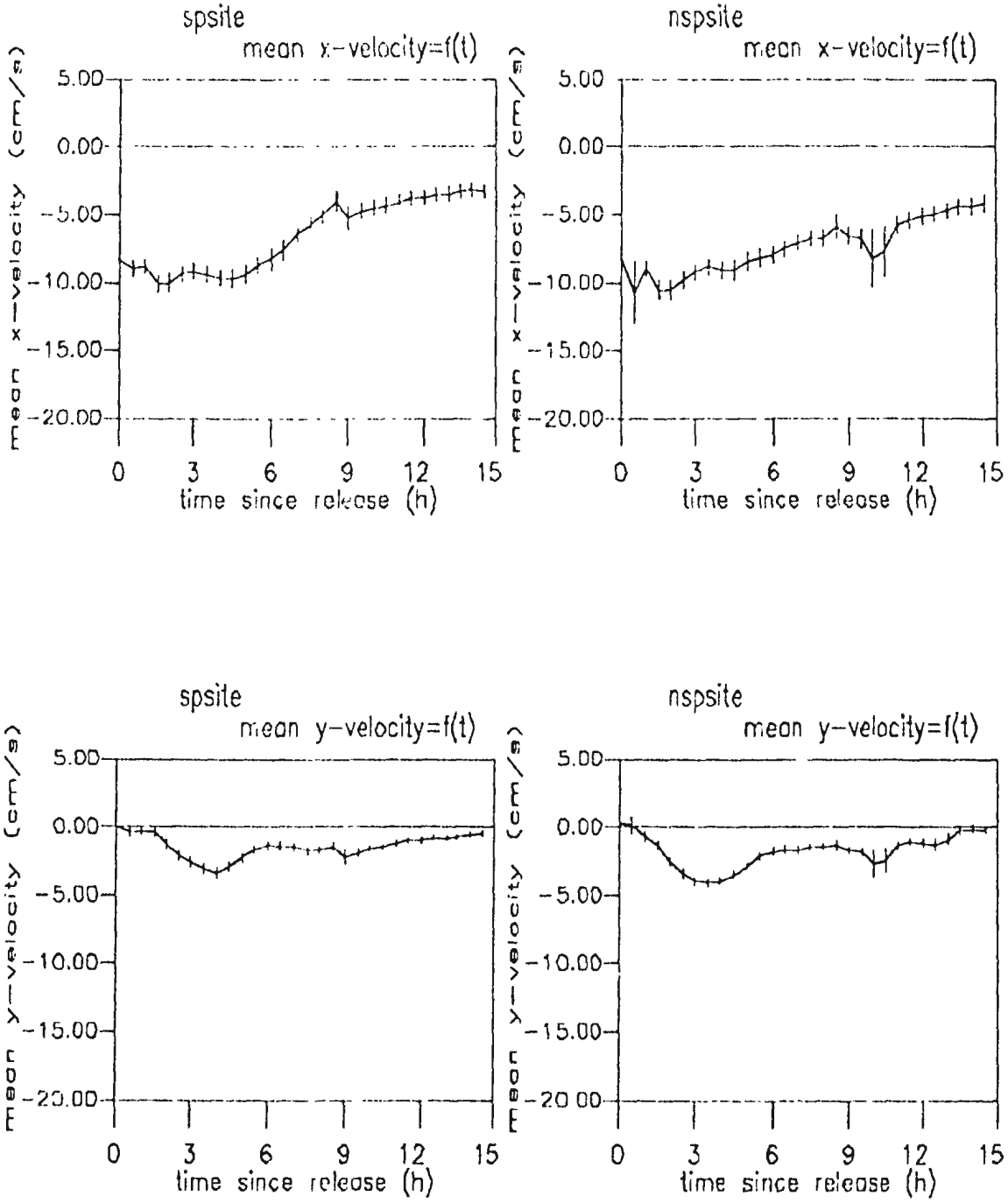

Figure 4-20: ***The single particle dispersion (i.e., variance var-X along the major axis of dispersion, var-Y along the minor axis of dispersion and orientation of the major axis of dispersion) as a function of time since drifter release, from the spawning site (left) and the nonspawning site (right).***

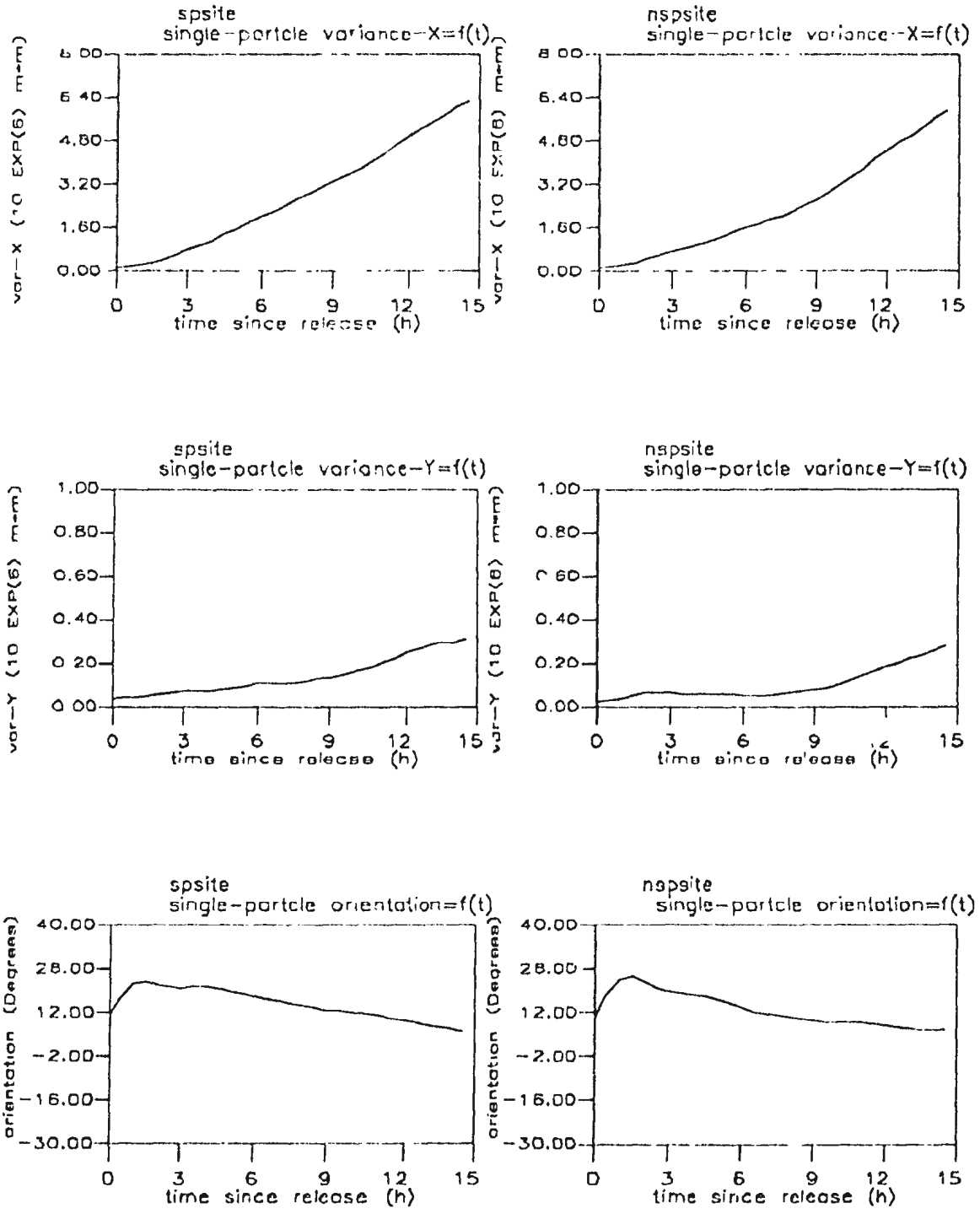

4.3. The cluster statistics.

4.3.1. Introduction

The cluster statistics consist of calculating the statistical parameters related to the diffusion of a cluster of drifters with respect to the cluster's centroid (cluster diffusion) as functions of time since release (Lagrangian time). We have conducted an ensemble of 36 biologically useful cluster release experiments (72 clusters of five drifters each) and another eight (Summer 1988) cluster release experiments, (16 clusters of five drifters each), that were only physically useful (see page 21 for more explanation). We will calculate the diffusion relative to the cluster centroid for the ensemble of all 64+16=82 clusters. Note that the cluster statistics differ from the single particle statistics. The cluster statistics describe the variability of the drifter positions within a cluster of drifters that were released simultaneously, i.e., the variance of the drifter positions with respect to the cluster centroid. This variance, as well as other diffusion characteristics are averaged over the ensemble of the cluster release experiments. Since in the cluster statistics the cluster centroid position is extracted, no information can be obtained for the variability from experiment to experiment of the cluster motion as a whole. This kind of information is obtained with the single particle statistics, in which, for our case especially, we resolve the ensemble of the five drifter cluster releases into an ensemble of single (one drifter) releases. We then examine the variability of the drifter position within this ensemble. At some Lagrangian time t, the theoretical mean centroid position over the ensemble of cluster centroids is equal to the theoretical mean position of the single particle statistics at the same Lagrangian time. The difference lies in the variance, which is larger for the single particle statistics. We will assume that the cluster statistics are stationary and homogeneous, just as in the case of the single particle statistics. To ensure that the number of the degrees of freedom (i.e., number of drifters) remained

steady as the Lagrangian time progressed, we only averaged over clusters that had five drifters until the 15th hour. Finally, the calculations were done for only the first 15 hours since release time. The above restrictions resulted in the decrease of the statistically useful population of the ensemble from 82 to 48 clusters. All the ensemble averaged parameters plotted as function of Lagrangian time are accompanied with error bars indicating ± 1 standard deviation of the mean value at half hour intervals. Finally, we also obtained cluster diffusion statistics for clusters with specific release site, release time, or flow conditions. All but the Summer 1988 experiments were included in these statistics.

4.3.2. The cluster statistics for all the clusters

Figure 4-21 shows the ensemble averaged cluster dispersion over all the 48 drifter clusters. In this Figure we have plotted cluster averaged quantities related to dispersion, i.e., the variance of the drifter position relative to the cluster centroid position along the major (X) and minor (Y) axes of dispersion, the cluster elongation, the angle the major axis of dispersion in an anticlockwise sense from the x axis, and the cluster area as functions of time since release. We see that, neither the variance along the major axis of dispersion, nor the variance along the minor axis of dispersion increase continuously with time. This indicates the existence of stretching deformation in the mean flow. Nevertheless, we see that the variance in both the major and minor axes of dispersion and the cluster area generally increase with time. The angle of orientation fluctuates between -6^o and 10^o, and the elongation fluctuates about 8 at all the times. Clearly, the cluster dispersion is principally along the x axis and about eight times greater in the x direction than in the y direction at all the times. We see that at t=0 the elongation is 8. The time t=0 corresponds to the first trisponder measurement of

the drifter position, which was usually conducted $10min$ to $0.5h$ after the cluster was released. Measurements of each drifter position immediately after their release were in many occasions impossible. We had to wait until the cluster dispersed adequately for the boat to be able to maneuver through it. In this period the cluster of drifters might have been elongated.

Clearly, the diffusion processes in the area are not caused by isotropic turbulence. The velocity gradients of the mean flow are seemingly important in causing stretching deformation and perhaps some divergence as will be shown in the following paragraph.

The velocity gradients $\frac{\partial u}{\partial x}$, $\frac{\partial u}{\partial y}$, $\frac{\partial v}{\partial x}$, $\frac{\partial v}{\partial z}$ of the flow within the area of the cluster were estimated using the cluster method of Okubo and Ebbesmeyer, (1976) (here u is the velocity component along the x axis which has an approximately along-shore direction). The method uses a first order Taylor expansion of the drifter velocity with respect to distance from cluster centroid. Assuming that the velocity gradients are uniform within the cluster, the above expansion results in the relative drifter velocities (with respect to the cluster centroid velocity) being linear functions of the relative drifter positions (with respect to the cluster centroid position). One then linearly regresses the relative velocities against the relative positions, to derive the velocity gradients. Having calculated the velocity gradients, one can then easily calculate the differential kinematic properties "dkp" i.e., the shearing and stretching deformations, the vorticity and the divergence (see page 11). We calculated the velocity gradients and dkp for each drifter cluster that had five drifters for a $15h$ period. The velocity gradients and "dkp" were calculated at each half hour interval since the cluster was deployed. We then averaged over all these drifter clusters at all the times. The mean velocity gradients and the mean "dkp" are summarized in Table 4-1. We also calculated the average gradients as functions of time since release (Figure 4-22).

Table 4-1: ***The mean velocity gradients and differential kinematic properties.***

Variable	Mean	std
$\frac{\partial u}{\partial x}(s^{-1})$	1.1×10^{-5}	1.9×10^{-5}
$\frac{\partial u}{\partial y}(s^{-1})$	7.7×10^{-5}	6.8×10^{-5}
$\frac{\partial v}{\partial x}(s^{-1})$	6.8×10^{-6}	1.1×10^{-5}
$\frac{\partial v}{\partial y}(s^{-1})$	2.6×10^{-5}	2.0×10^{-5}
stretching deformation (s^{-1})	-1.4×10^{-5}	2.0×10^{-5}
shearing deformation (s^{-1})	8.4×10^{-5}	6.9×10^{-5}
vorticity (s^{-1})	-7.0×10^{-5}	6.9×10^{-5}
divergence (s^{-1})	3.7×10^{-5}	2.8×10^{-5}

In Table 4-1 we see that the largest of the velocity gradients is the across-shore gradient of the along-shore velocity component, which is equal to $\frac{\partial u}{\partial y} = 7.7 \times 10^{-5} s^{-1}$. This gradient tends to dominate the other ones and is expected to cause elongation of the cluster in the along-shore direction, due to the "shear dispersion effect" as described in section 1.2.2. A clearer idea of what causes the along-shore elongation can be obtained if we observe Figure 4-22 of the mean velocity gradients as functions of time since release. It is clear from this Figure that the mean velocity gradient $\Omega_h = \frac{\partial u}{\partial y}$ achieves much larger values than the other three gradients for the first $1.5h$ of the trajectory, and subsequently achieves values comparable in magnitude with the values of the other three. The very large values of Ω_h at the first $1.5h$ since release are probably a result of the interaction of the mean flow, which is mainly along-shore, with the complicated topography (reefs, channels, see Figure 2-2) at the beginning of the experiment. For the first $1.5h$ therefore, we can assume that $\Omega_h \approx 15 \times 10^{-5} s^{-1} = constant$ (this value being the time average over the first $1.5h$) and that $\Omega_a = \Omega_c = \Omega_d = 0$ (see caption of Figure 4-22 for definitions and symbols

of gradients). We can thus use equation (1.21) to derive the approximate value of elongation due to the shear dispersion effect at $t=1.5h$, i.e., $\varepsilon(t=1.5h) \approx \Omega_h t \approx 15\times10^{-4}s^{-1}\times1.5h\times3600s/h\approx8$. Having in mind that the measured elongation fluctuates about 8 at all the times, the above calculation indicates that the cluster has already achieved its final value of elongation, at $1.5h$ after the drifter release. The cluster elongates rapidly at the first $1.5h$, but subsequently there is no considerable increase in its elongation. This is not in contradiction with our discussion in page 104, about the elongation being equal to 8 at $t=0$, if we hypothesise that the above described "shear dispersion" effect starts before the time corresponding to $t=0$ and continues being significant until $t=1.5h$. Also, the fact that $\Omega_h t\sim 8$ at $t=1.5h$, indicates that, according to (1.20), the shear elongation is eight times larger than the length scale $\sqrt{Kt}$ of the longitudinal eddy diffusion. Of course, the high value of $\Omega_h=\frac{\partial u}{\partial y}$ during the first $1.5h$ of the experiment, would cause along-shore elongation even in the absence of isotropic eddy diffusivity. This is because a nonnegligible value of Ω_h within a cluster implies that drifters within the cluster separated by Δy in the across-shore direction, will move with different along-shore velocities. This shearing would occur after the elapse of some time interval Δt, in the increase by Δx of the drifter along-shore separation according to $\Delta x=\Delta y\Omega_h\Delta t$. Taking as typical value of the across-shore drifter separation during the first $1.5h$ of the experiment, the typical across-shore standard deviation σ_y of the drifter position with respect to the cluster centroid during that time interval, i.e., $\Delta y=\sigma_y\approx10m$; $\Omega_h\approx15\times10^{-4}s^{-1}$; $\Delta t=1.5h\times3600s/h$, we derive an along-shore stretching $\Delta x\approx10m\times15\times10^{-4}\times1.5\times3600\approx81m$, and thus an along-shore elongation $\varepsilon=\Delta x/\sigma_y=81/10=8.1$. It seems that both mechanisms, of the horizontal shear diffusion on the one side and of the pure straining motion on the other side contribute almost equally to the along-shore elongation. This along-shore elongation is probably imposed by the topography near the area of the experiment, and therefore it might be possible to scale Ω_h as $\Omega_h=O(\frac{U}{Y})$,

where U is an along-shore velocity and Y' an across-shore length scale, imposed by the local topography. This in turn would result in Ω_h, the along-shore dispersion and the elongation fluctuating with the along-shore wind, since U is fluctuating with the along-shore wind, but Y' remains constant.

Finally, we see in Table 4-1 that the average divergence is positive, which indicates that the velocity field tends to diverge. This is in agreement with the observed increase with time of the cluster area (Figure 4-21).

An additional insight into the cluster diffusion processes of the area can be gained if we calculate the autocorrelation function $R_c(\tau)$ of the velocity (u_c, v_c) relative to the cluster centroid. The autocorrelation function for relative motion, can be related to the variance of positions about the centroid via *Taylor's theorem*. Note however that *Taylor's theorem* is strictly appropriate for single particle motion in a stationary turbulent field of no mean motion. The motion of drifters relative to their cluster centroid is not stationary, since the dispersion rate increases with time since release (Csanady, 1973), and therefore R_c is a function of time since release, t. In our computational method of R_c however, we implicitly assume that R_c is independent of t, since we average over the duration of an experiment. This is done in order to increase the degrees of freedom of the statistical estimate of R_c. The computational method is very similar to the one implemented for the calculation of the autocorrelation function of the single particle motion, and can be outlined as follows. Each drifter trajectory had $N=30$ positions at half hour time steps. We discretize time and use j to indicate lag and i to indicate time since release. In order to calculate the autocorrelation function $R^c(j)$ at the j^{th} lag, we then used the following formula

$$R^c(j)=[\sum_{m=1}^{M}\sum_{l=1}^{L}\sum_{i=1}^{N-j} u_c(i,l,m)\, u_c(i+j,l,m)\,]/MNL \qquad (4.10)$$

where $u_c(i,l,m)$ is the residual velocity of the m^{th} trajectory of the l^{th} cluster at the i^{th} time step since release. We averaged over the $M=5$ drifter

trajectories per cluster, the $N=30$ time steps per trajectory, and the $L=48$ clusters. The residual velocity was calculated relative to the cluster centroid.

$$u_r(i,l,m)=u(i,l,m)-\bar{u}(i,l). \tag{4.11}$$

Here $\bar{u}(i,l)$ is the velocity of the centroid of the l^{th} cluster at the i^{th} time step, that is

$$\bar{u}(i,l)=[\sum_{m=1}^{M} u(i,l,m)]/M \tag{4.12}$$

where $u(i,l,m)$ is the velocity at the i^{th} time step of the m^{th} drifter in the l^{th} cluster. In (4.10), we divided by MNL, instead of $M(N-j)L$ to correct for the bias at large lags (Beauchamp and Yuen, 1979; p 186).

The autocorrelations R_x^r, R_y^r of the x and y components of the drifter velocity relative to the centroid velocity, are plotted as functions of lag in Figures 4-23 and 4-24 respectively. We see that both R_x^r and R_y^r drop rapidly with increasing lag, and that R_y^r has a small negative lobe. It is reasonable to integrate the area under these autocorrelation functions to obtain integral time scales $\tau_x^r=0.8h$ and $\tau_y^r=0.9h$ for the x and y components of motion relative to the cluster centroid. The mean square value of relative velocity is $\langle u_r^2\rangle=0.0031 m^2/s^2$ in the x direction and $\langle v_r^2\rangle=0.00075 m^2/s^2$ in the y direction. This gives cluster diffusivities calculated by use of equation (1.14), i.e., $K_x^r=\langle u_r^2\rangle\times\tau_x^r=8.9 m^2/s$ and $K_y^r=\langle v_r^2\rangle\times\tau_y^r=2.4 m^2/s$ in the x and y directions respectively. Gross diffusivities G^r can be defined from changes in variance $(\sigma_x^r,\ \sigma_y^r)$ of the drifter position relative to the cluster centroid over the duration T of the experiment, as follows

$$G_x^r=\frac{1}{2}\frac{(\sigma_x^r)^2(t=T)-(\sigma_x^r)^2(t=0)}{T} \tag{4.13}$$

$$G_y^r=\frac{1}{2}\frac{(\sigma_y^r)^2(t=T)-(\sigma_y^r)^2(t=0)}{T}$$

Note that in (4.13), $(\sigma_x^r)^2(t=0)=1181 m^2$ and $(\sigma_y^r)^2(t=0)=1093 m^2$. In an instantaneous point release the above values would be equal to zero. The time $t=0$ corresponds in our case to the time when the first drifter position fix was

taken, when the cluster was already slightly spread (see page 104 for more explanation). From the values in Figure 4-21 these diffusivities are $G_x^c = 0.46 m^2/s$ and $G_y^c = 0.23 m^2/s$. The gross diffusivities G^c are one order of magnitude smaller than the eddy diffusivities K^c of the cluster diffusion. This is probably because the statistics of the cluster diffusion are assumed to be homogeneous and stationary, in order to calculate K^c, R^c. These assumptions are not completely valid for this data. Single particle diffusivities are factors 7 and 2 greater than cluster diffusivities for the x and y components of dispersion respectively. Also, the mean square values of the single particle residual velocities for the two axes are larger by a factor of 2 than the mean square values of the drifter velocities with respect to the cluster centroid velocity. Thus there is more variability in the paths of clusters than in the paths of drifters within a cluster. This is exactly as might be expected considering the variable nature of the wind-driven flow. Finally, the integral time scale of the single particle diffusion along the x axis is three times larger than the integral time scale of the cluster diffusion along the same axis (this is not true for the y axis however, where the integral time scales of the single particle and cluster diffusion have similar magnitude). The along-shore component (along x axis) drifter velocity decorrelates faster if it is considered relative to the cluster centroid, rather than if it is considered with respect to the mean flow (averaged over all the experiments). This was expected, since the mean flow does not change with Lagrangian time as fast as the velocity of the cluster centroid in an experiment does. The mean flow is equal to the average cluster centroid velocity over all the experiments and the fluctuations with Lagrangian time of the cluster centroid are largely smoothed out when we average over all the experiments.

Figures 4-25 and 4-26 show how the variance of the x and y components of position relative to the centroid vary as a functions of time since cluster deployment. The plots are on a log-log scale to investigate power laws. We see

that the variance along both x and y axes approximately increases proportional to t (i.e., is fitted by a line of slope equal to 1 in the log-log scale), when we average over the duration of the experiment. Thus in this gross sense the eddy diffusion is Fickian.

Figure 4-21: *The averaged (over all clusters) cluster dispersion (i.e., variance var-X along the major axis of dispersion, var-Y along the minor axis of dispersion, cluster area, orientation of the major axis of dispersion, and elongation) as functions of time since release.*

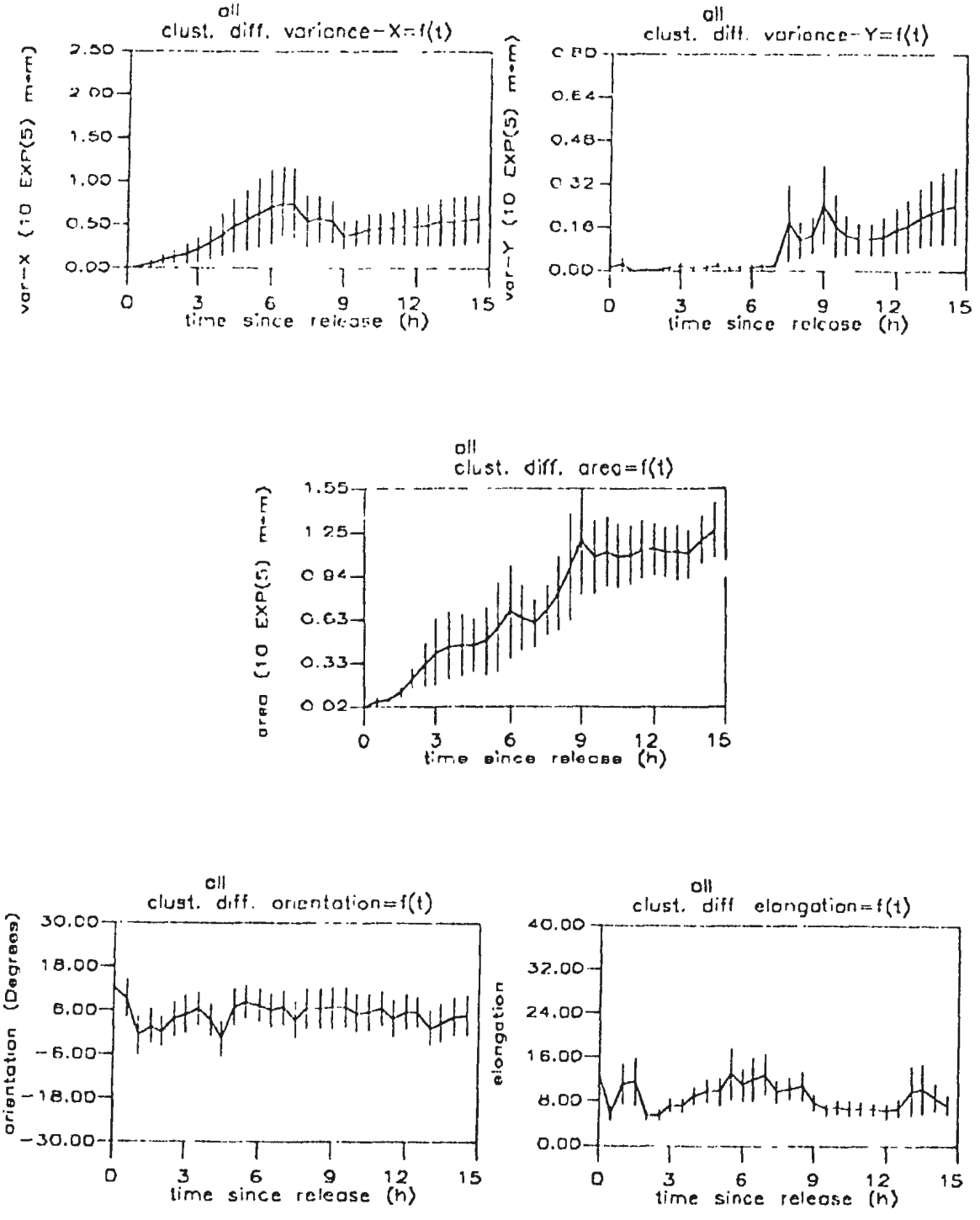

Figure 4-22: ***The mean velocity gradients,*** $\Omega_a=\frac{\partial u}{\partial x}$, $\Omega_b=\frac{\partial u}{\partial y}$, $\Omega_c=\frac{\partial v}{\partial x}$, $\Omega_d=\frac{\partial v}{\partial y}$ ***as functions of time since release. The value of zero gradient is indicated by a line parallel to the*** x ***axis.***

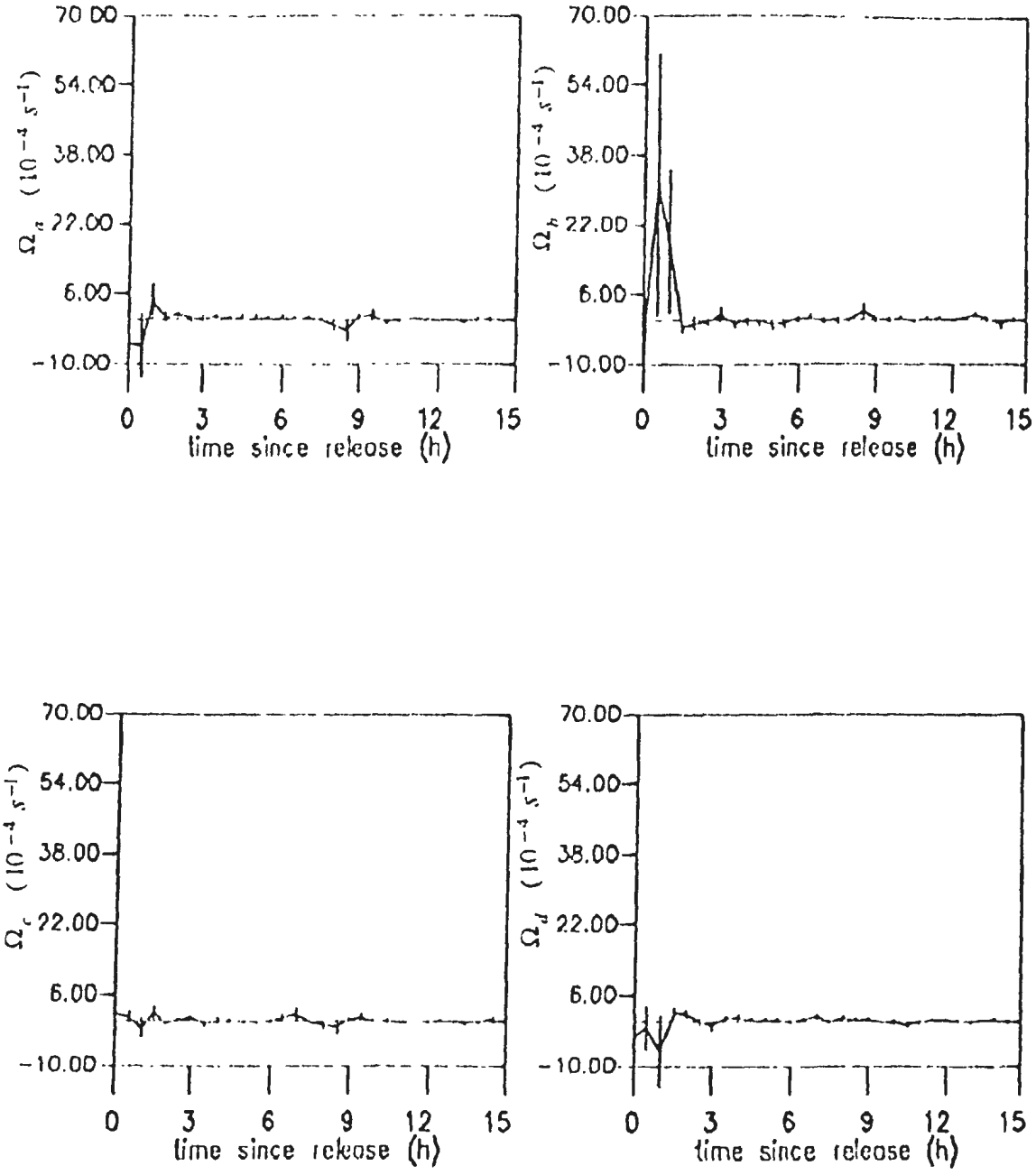

Figure 4-23: ***The autocorrelation function of the x component of the relative (to the cluster centroid velocity) drifter velocity versus lag (solid line), and its best fit exponentially dropping function (dashed line).***

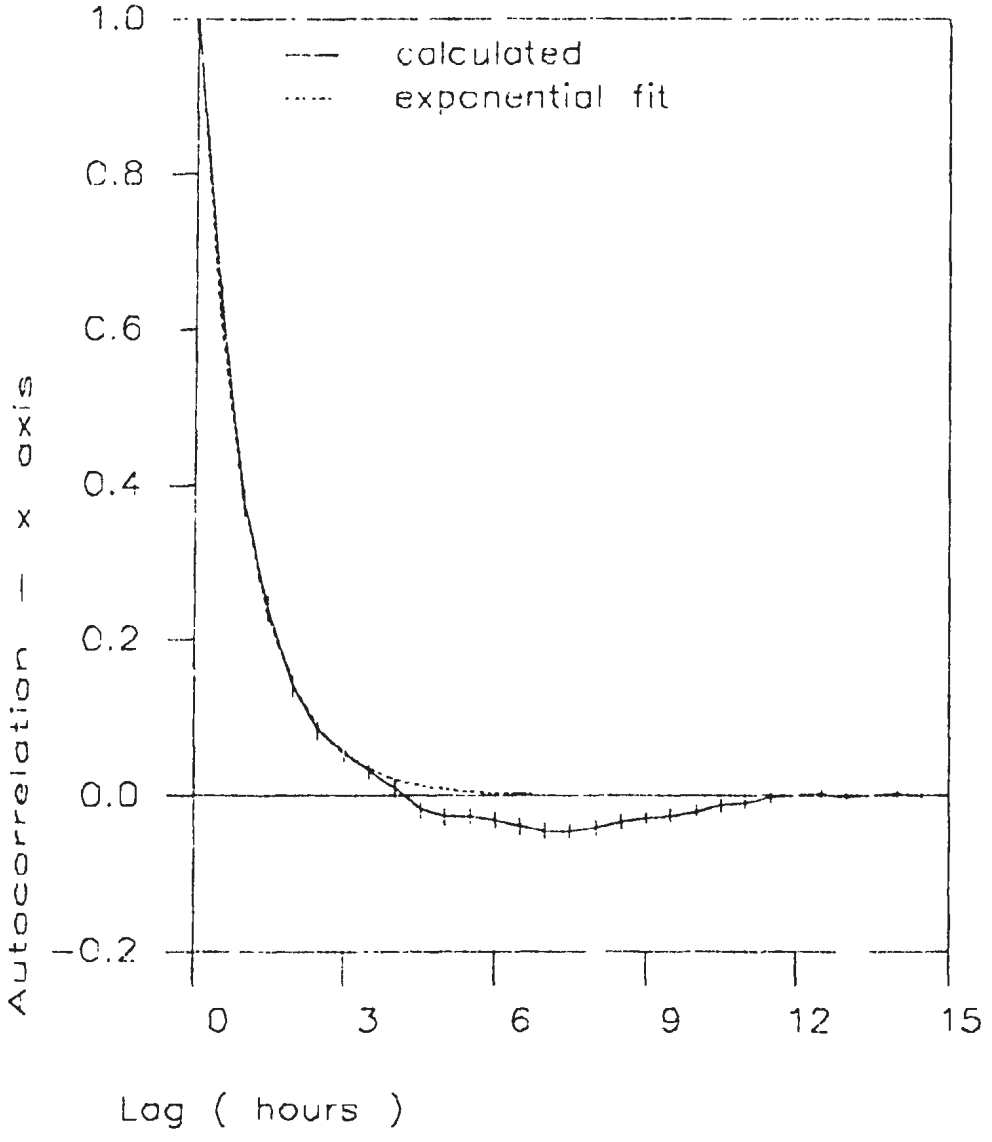

Figure 4-24: ***The autocorrelation function of the y component of the relative (to the cluster centroid velocity) drifter velocity versus lag (solid line), and its best fit exponentially dropping function (dashed line).***

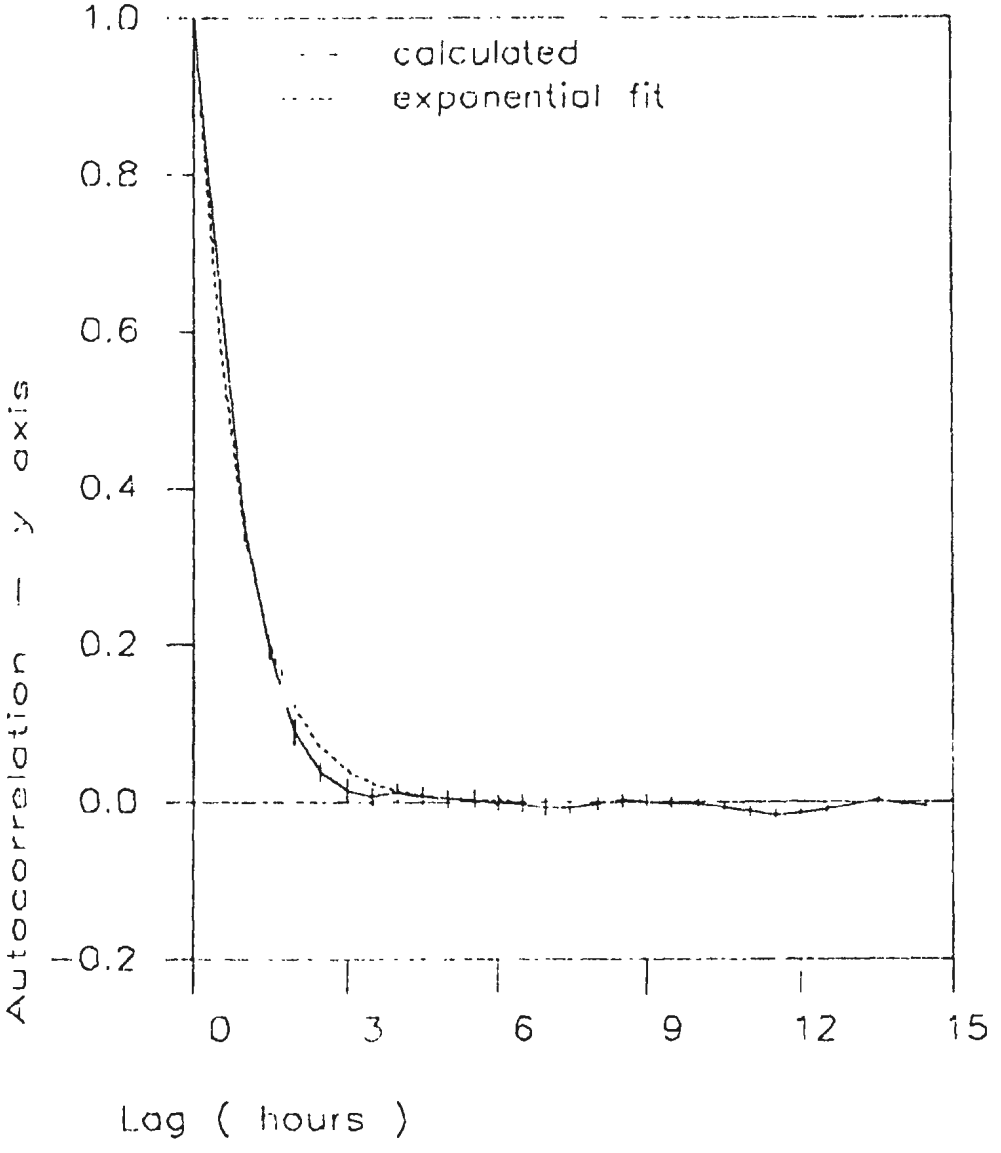

Figure 4-25: *The variance (stars) along the x axis of the relative (to the position of the cluster centroid) drifter position versus lag, plotted in a log-log scale. The solid straight line of slope 1 is the one that best fits the variance, and indicates that the variance grows as time raised to the power of 1*

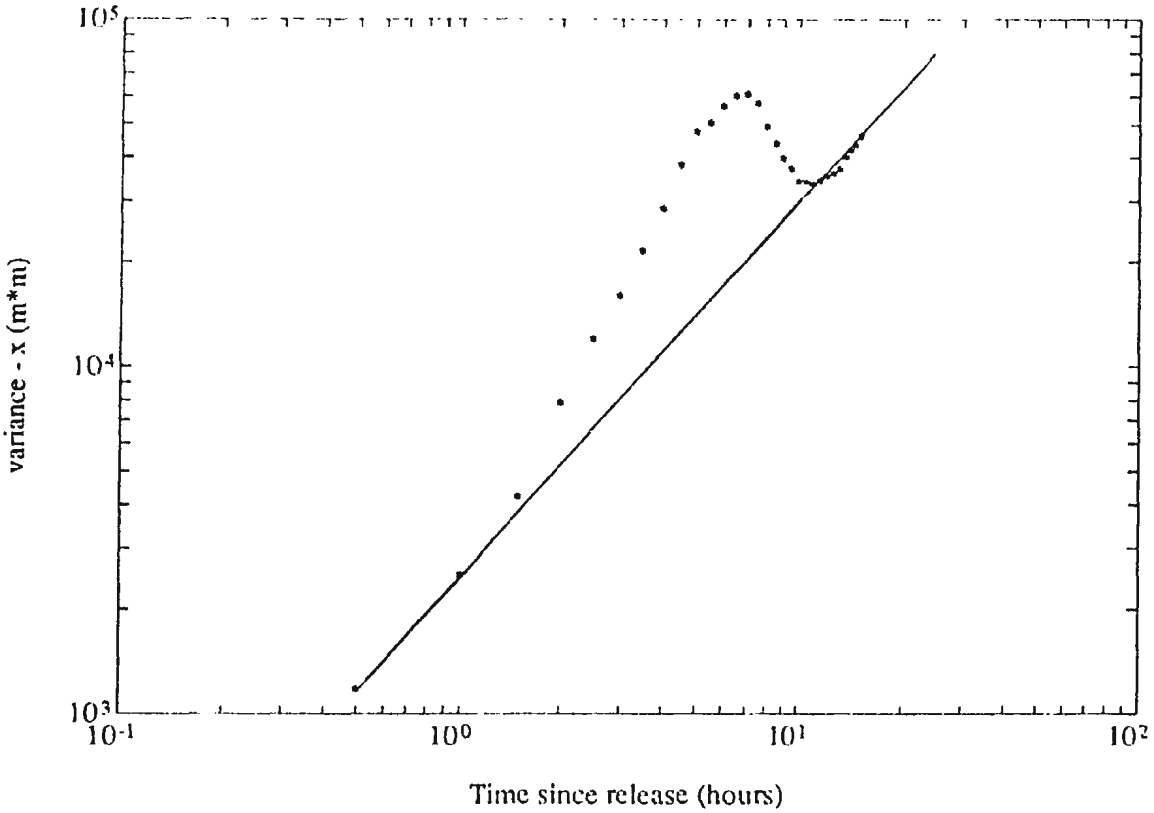

Figure 4-26: *The variance (stars) along the y axis of the relative (to the position of the cluster centroid) drifter position versus lag, plotted in a log-log scale. The solid straight line of slope 1 is the one that best fits the variance, and indicates that the variance grows as time raised to the power of 1*

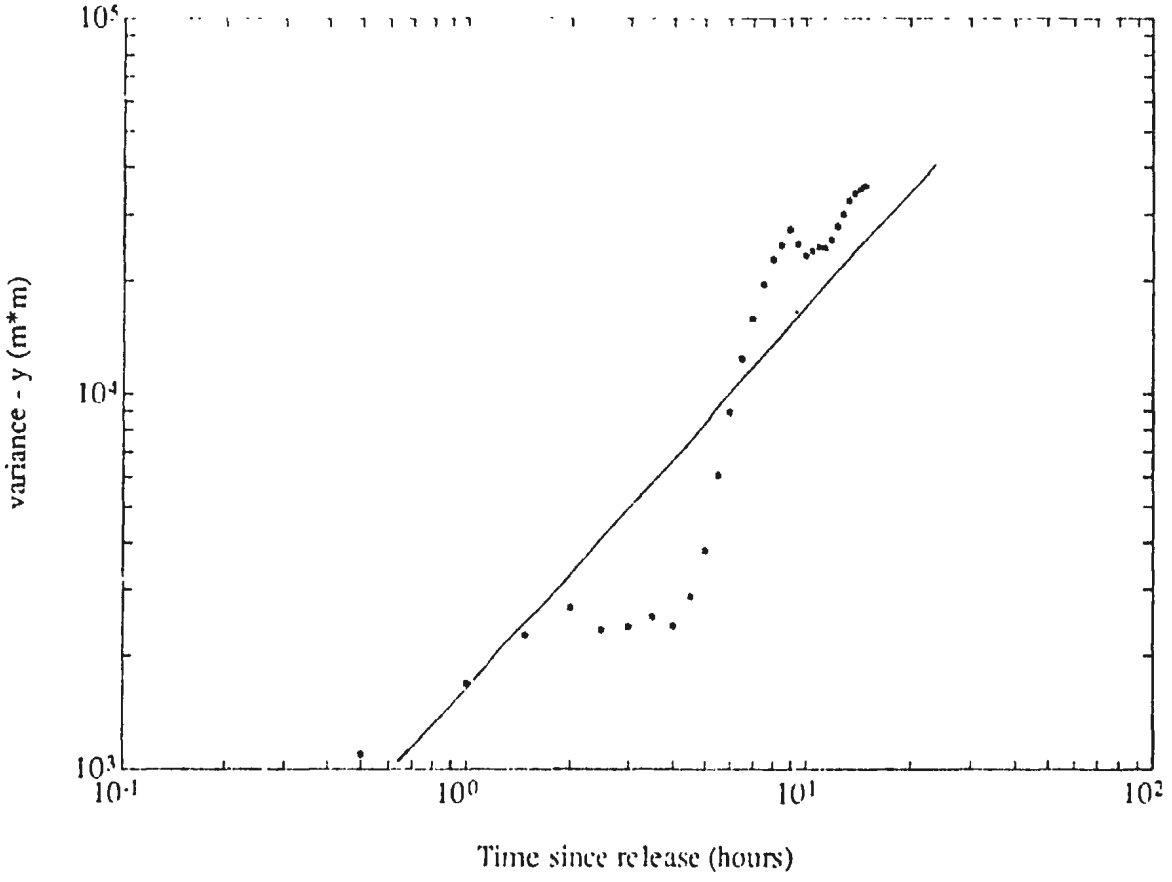

4.3.3. Cluster dispersion during the wet and dry seasons

The dry season and wet season cluster averaged dispersion characteristics (variance of drifter position with respect to the cluster centroid along the major and minor axes of dispersion, the cluster elongation and the angle of orientation anticlockwise from the x axis) are plotted in Figure 4-27 as functions of time since release. We see that for both seasons the cluster is elongated (elongation fluctuates around the value of 8). The wet season cluster elongation is slightly smaller than the dry season cluster elongation. The angle of the major axis with the x axis (anticlockwise) fluctuates between -6^o and 6^o for the wet season and between -6^o and 18^o for the dry season. The typical values of the angle of orientation of the cluster are small enough in both seasons to lead to the conclusion that the cluster tends to elongate in an along-shore direction throughout the year. The variance in the along-shore direction (major axis) achieves larger values during the dry season than during the wet season in contrast to single particle statistics where the along-shore variance is slightly larger in the wet season. The across-shore (minor axis) variance achieves the largest values during the wet season, something that also happens with the across-shore variance of the single particle statistics.

Figure 4-27: *The cluster dispersion (i.e., variance var-X along the major axis of dispersion, var-Y along the minor axis of dispersion, orientation of the major axis of dispersion, and elongation) as function of time since release, during the wet season (left) and the dry season (right).*

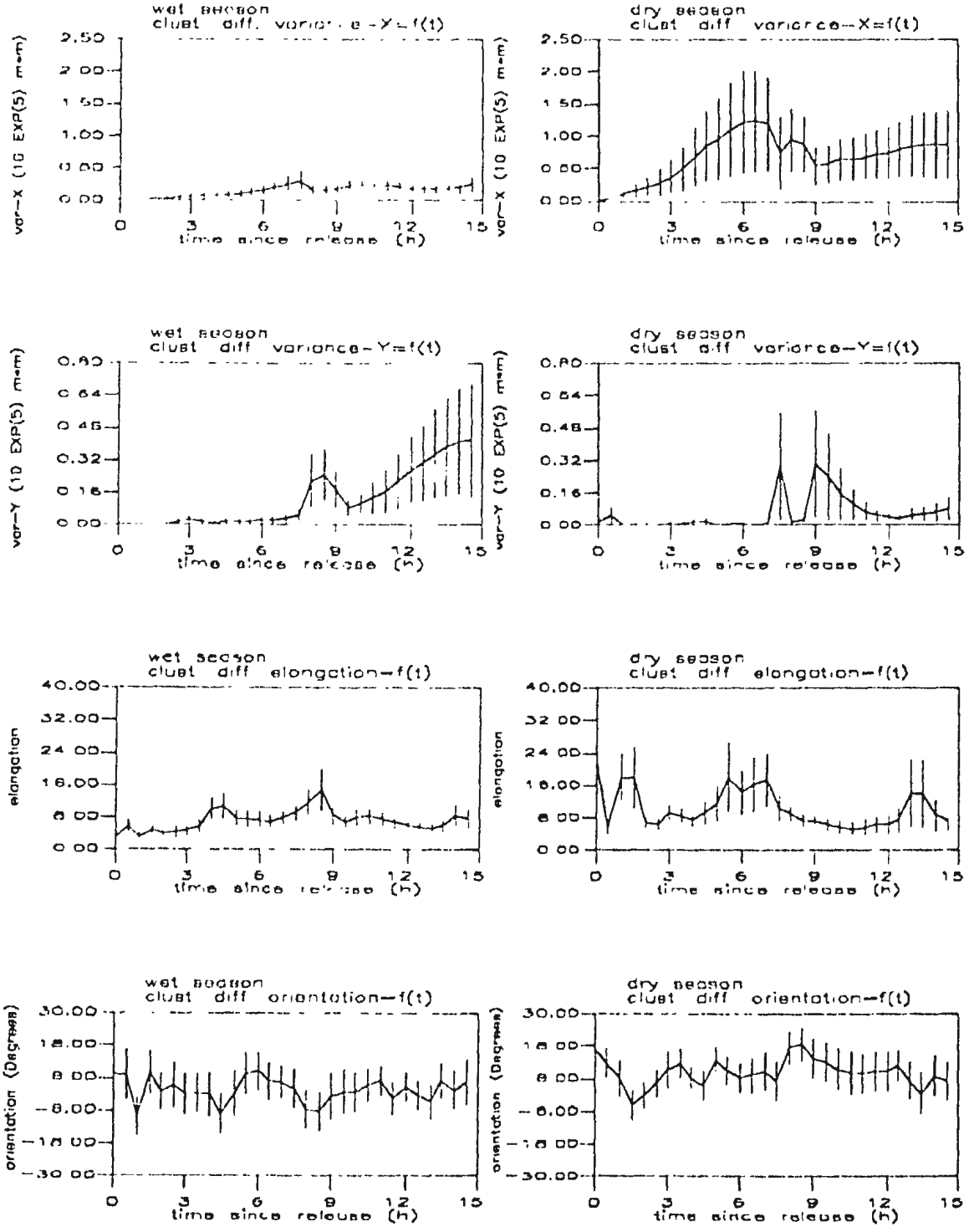

4.3.4. Dispersion of clusters at spawning and nonspawning times.

The cluster averaged dispersion characteristics for the spawning time and the nonspawning time are plotted in Figure 4-28 as functions of time since release. The spawning time and the nonspawning time ensembles have cluster averaged variances along the major axis of dispersion that vary with time . Regarding the major axis of dispersion, we see that the spawning time ensemble has a cluster variance along this axis that generally increases with time, except for a brief decrease at about the 9^{th} hour. The spawning time ensemble is not greatly variable from cluster to cluster. The nonspawning time ensemble has a relatively rapid initial increase of cluster variance followed by a sharp decrease in variance. Also the cluster dispersion is much more variable (see standard deviation bars on the plots) for the nonspawning time ensemble than for the spawning time ensemble. The variance along the minor axis increases much more rapidly for the spawning time ensemble than for the nonspawning time ensemble. Clearly, the cluster dispersion of the spawning time ensemble is larger than that of the nonspawning time ensemble, and this might be of some biological significance. The spawning time ensemble has a cluster elongation that is more variable than the nonspawning time ensemble. Also, the spawning time cluster elongation tends to slightly increase with time, in contrast to the nonspawning time elongation that tends to slightly decrease with time. The angle of orientation of the principal axis of dispersion varies faster with time for the spawning time releases than for the nonspawning time releases.

Figure 4-28: *Cluster dispersion (i.e., variance var-X along the major axis of dispersion, var-Y along the minor axis of dispersion , orientation of the major axis of dispersion, and elongation) as function of time since release at the spawning time (left) and the nonspawning time (right).*

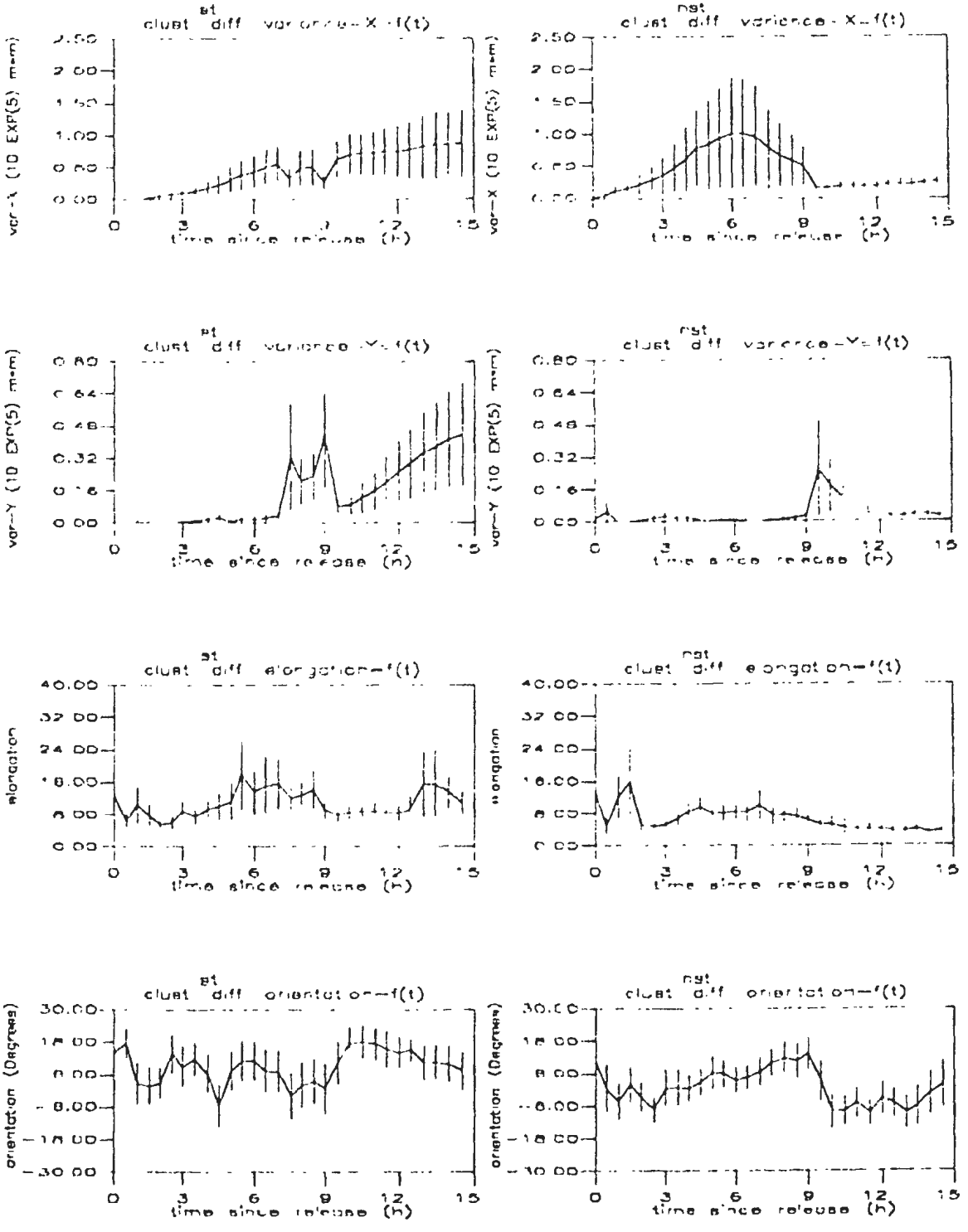

4.3.5. Dispersion of clusters released from spawning and nonspawning sites.

In Figure 4-29 we have plotted the cluster averaged dispersion characteristics of the spawning site and the nonspawning site ensembles. The spawning site cluster seems to disperse more than the nonspawning site cluster, and this again might be of some biological significance. The spawning site cluster is more variable with time since release, and also more variable from experiment to experiment, than the nonspawning site cluster. The cluster elongation for spawning site releases is not significantly different from the cluster elongation for nonspawning site releases. The angle of orientation varies considerably with time for the nonspawning site ensemble, but it stays nearly constant for the spawning site ensemble.

Figure 4-29: *Cluster dispersion (i.e., variance var-X along the major axis of dispersion, var-Y along the minor axis of dispersion , orientation of the major axis of dispersion, and elongation) as function of time since release from the spawning site (left) and the nonspawning site (right).*

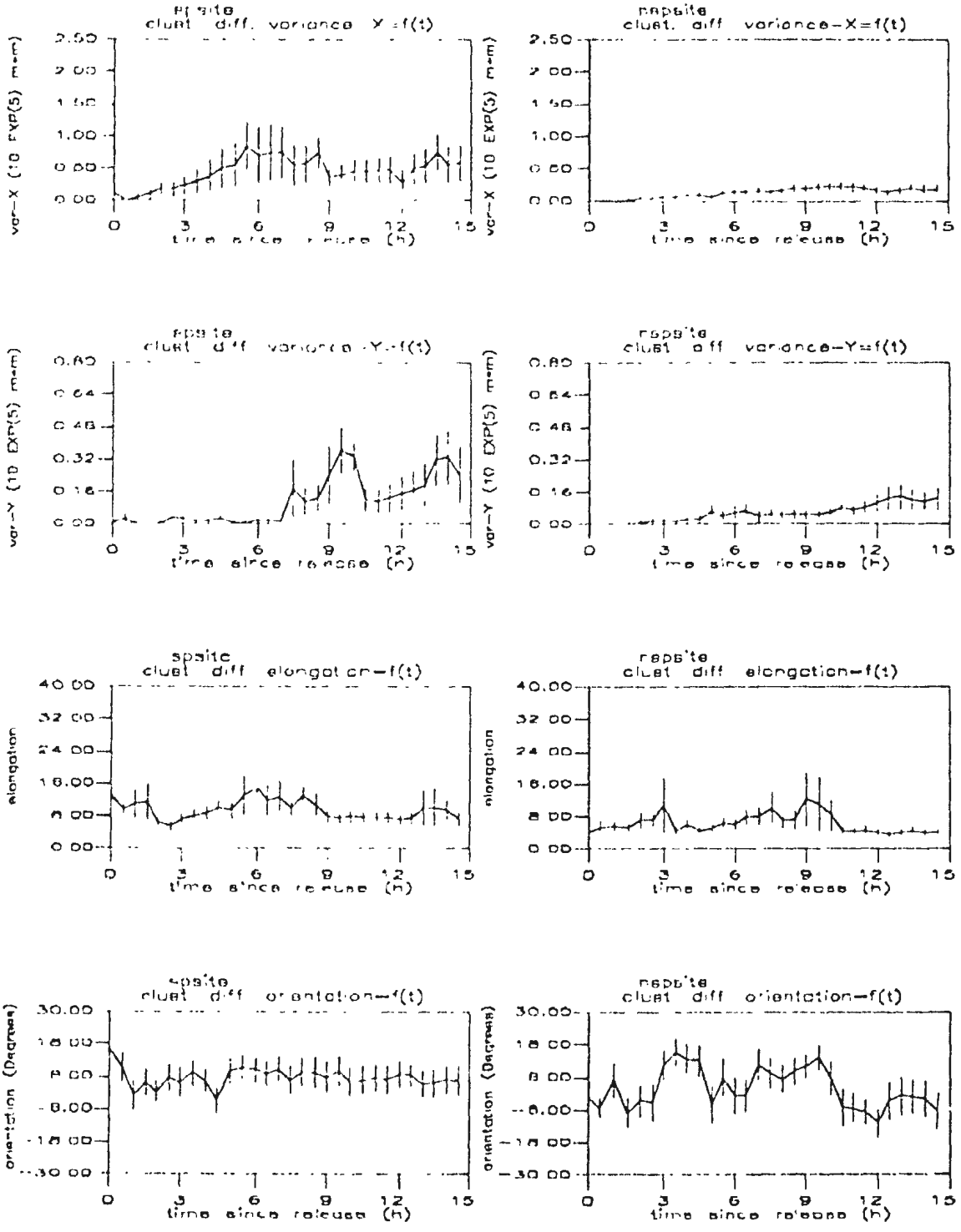

4.3.6. The distinctness

In all our inshore experiments we tracked two clusters simultaneously. One cluster was released at a spawning site, another one at a nonspawning site. We are interested to know when, if ever, the spreading of these clusters results in them mixing together and no longer being distinct. We therefore introduced the parameter of distinctness, Di, which can be defined as:

$$Di = \frac{d_c}{\sigma_p} \tag{4.14}$$

where d_c is the distance between the centroids of the two clusters, and σ_p is the sum of the projections of the standard deviations of the two clusters onto the line joining the centroids. For each cluster we chose the biggest projection, whether it is the projection of the major or of the minor axis standard deviation. If Di has a value larger than 1, then the two clusters are distinct, otherwise the clusters have merged. For the case when the two cluster ellipses are close to each other, then it might happen that $Di < 1$ without the ellipses really intersecting, i.e., without the clusters being merged (see Figure 4-30 for an illustrative example). Therefore, if and when Di was less than 1 we additionally examined if the the two ellipses did intersect. If the ellipses did not intersect but still $Di < 1$ then we considered this value of Di as false and did not include it in our statistical estimations. We calculated Di for all the combinations of S, NS clusters. The distance between an S site (S1 or S2) and an NS site (NS1 or NS2) was typically $300-400m$ for the actual dye release sites and $300-600m$ for the corresponding drifter release sites (see Figure 2-3).

The ensemble averaged distinctness over all the inshore experiments for which the two clusters had five drifters until the 15^{th} hour since release, is plotted as function of time since release in Figure 4-31. In this Figure we see that the distinctness decreases with time, as expected, since the two clusters were released from nearby sites, and their area grows with time. The criterion for judging when the two clusters merge was as to when the lower confidence

limit of the mean distinctness becomes equal to 1. The spawning site cluster remains distinct from the nonspawning site for approximately 15 *h*. However, different release sites do not result in different mean trajectories (averaged over longer periods of time), as was pointed out in section 4.2.4.

Figure 4-32 shows the ensemble averaged distinctness over the spawning time and the nonspawning time experiments. We can see that initially (first 3 *h* since release) the two clusters approach each other more rapidly for nonspawning time deployments than for spawning time deployments. After the 3rd *h* the distinctness is independent of deployment time.

Figure 4-33 shows the mean distinctness for the wet and dry season ensembles. Clearly, the clusters approach each other much more rapidly in the dry season. In particular, the clusters merge (on average) at around the 3rd *h* since release during the dry season. During the wet season, the clusters remain distinct until the 15th *h* since release.

Figure 4-30: *A case where the distinctness Di is smaller than 1 but the two clusters are not merged. The major and minor axes of the two clusters are the solid lines. Dashed lines indicate distances. The elongation of both clusters is eight, which is the typical cluster elongation value in the area of the experiment.*

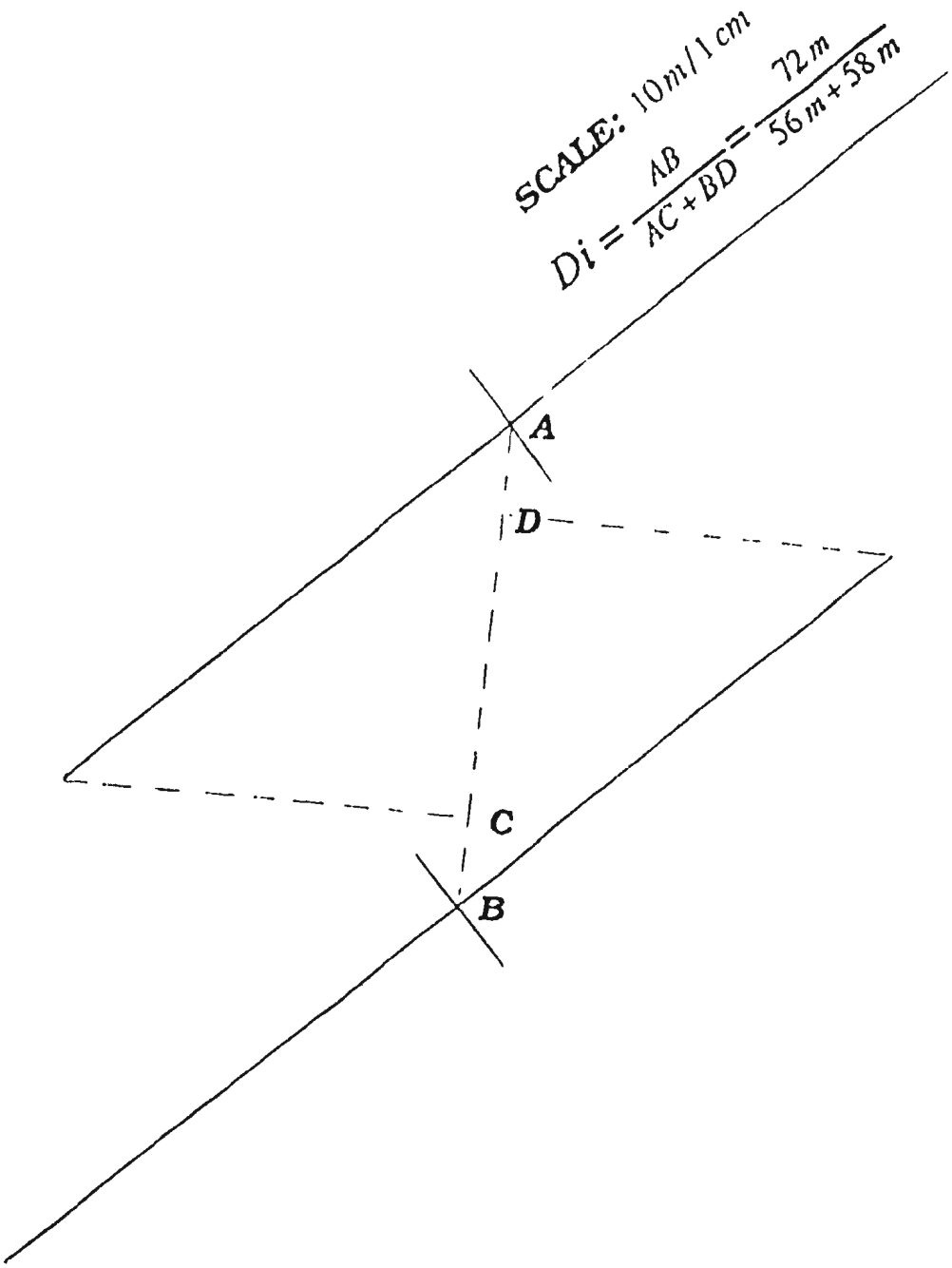

Figure 4-31: ***The ensemble averaged (over all the experiments) distinctness as a function of time since release.***

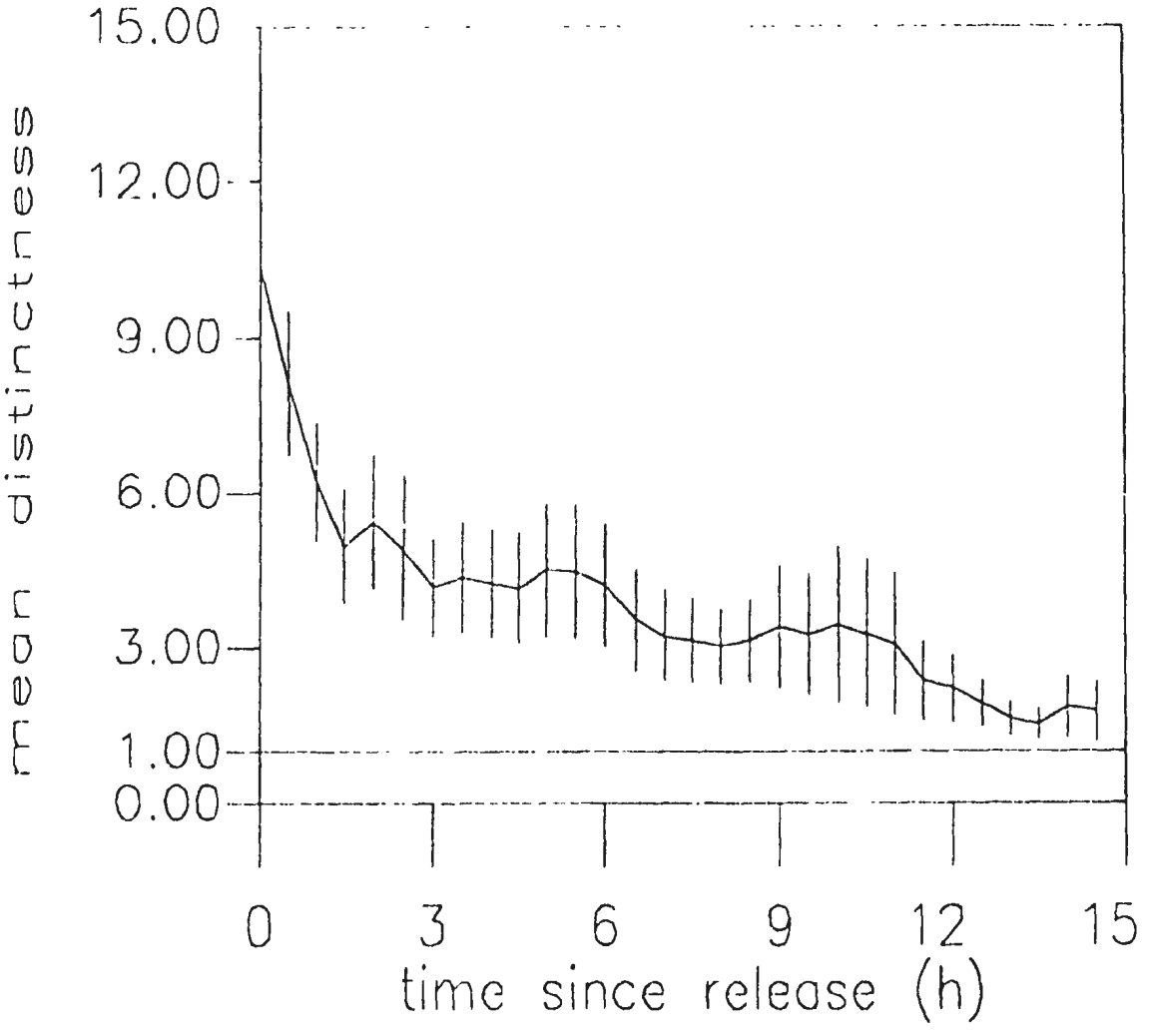

Figure 4-32: ***The ensemble averaged distinctness as a function of time since release, at the nonspawning time (top) and the spawning time (bottom).***

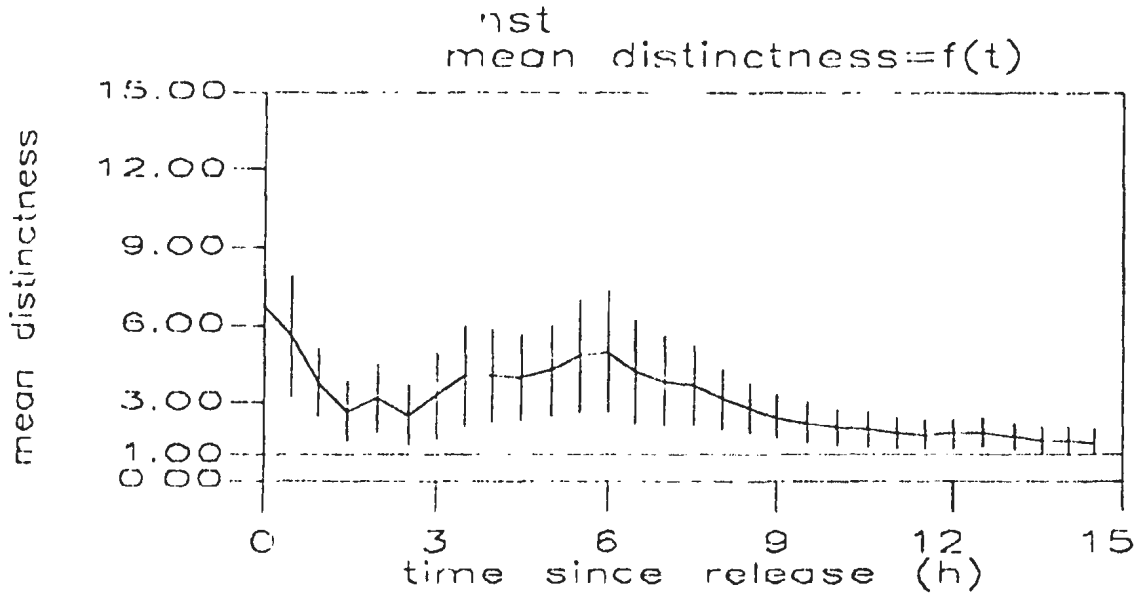

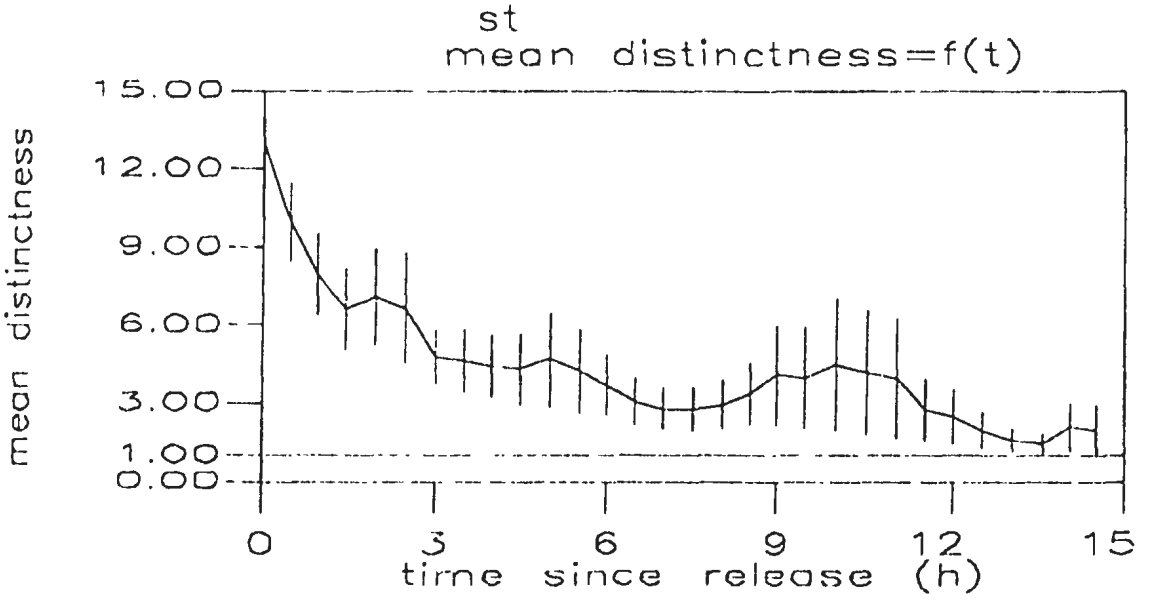

Figure 4-33: ***The ensemble averaged distinctness as a function of time since release, during the dry season (top) and the wet season (bottom).***

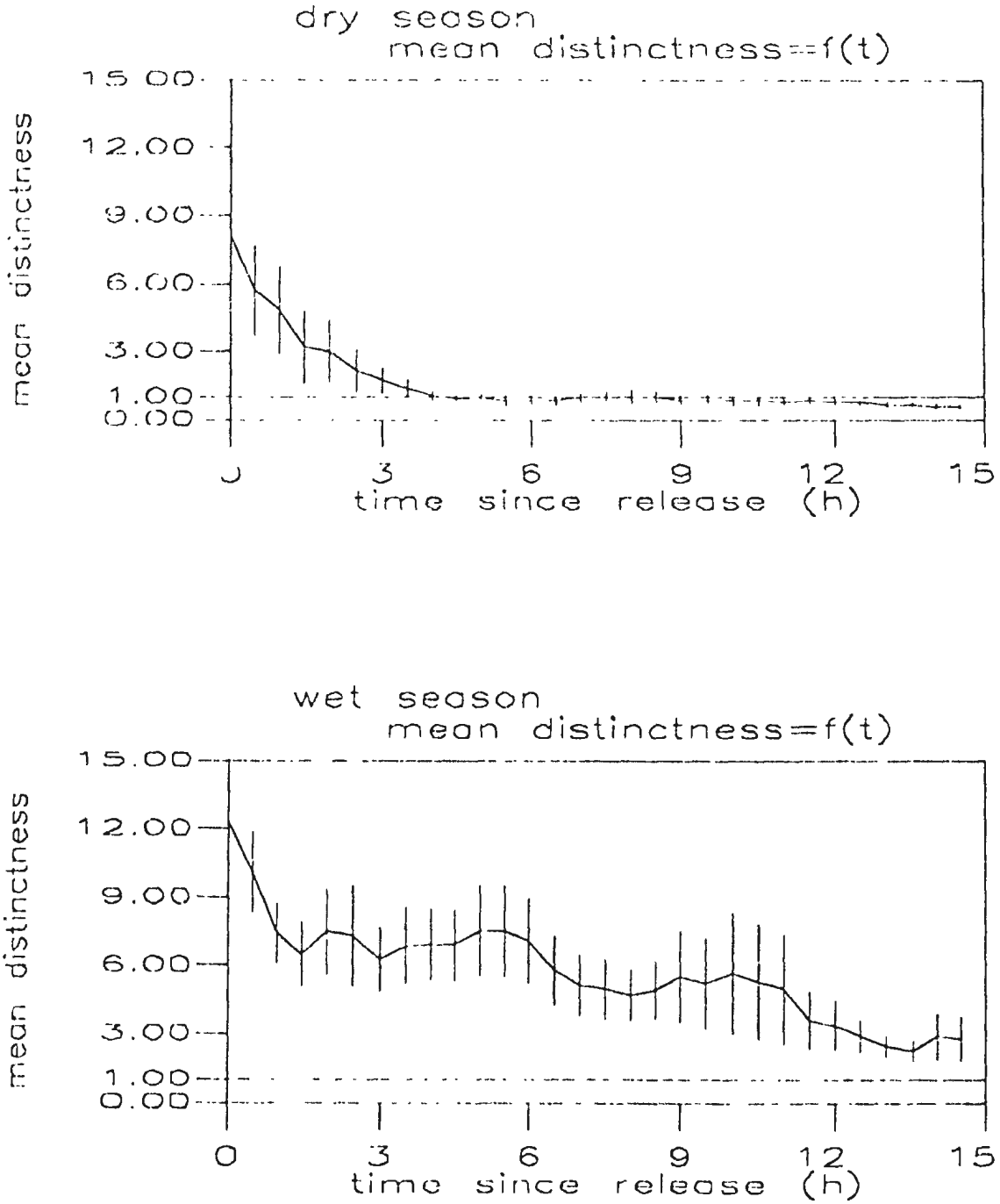

Chapter 5

The Fall 1989 experiments

5.1. The bead experiments

We are ultimately interested in the dispersion of fish eggs, rather than the dispersion of drifters. Polystyrine beads were designed to match the size and buoyancy of the eggs. Thus the beads had a radius $r_b \approx 2.7 \times 10^{-4} m$ and density $\rho_b = 1013 kg/m^3$. In the Fall 1989 experiments, a patch of $N_{tot} = 5 \times 10^6$ beads was released, along with the dye patch, at the spawning site and time. Net tows were conducted in the area around the drifter cluster $24\,h$ after the release, to measure the number $N = N(x,y)$ of beads per tow as a function of position (x,y) at the end of the experiment. The measured bead distribution N could then be compared with the predicted bead distribution N_p. The predicted bead distribution is based on the drifter data $24\,h$ after release and is given by

$$N_p = S C_b \tag{5.1}$$

where C_b is the predicted horizontal concentration of the beads (based on the drifter data $24\,h$ after release) and S is the area of the water sampled during a tow conduction. The bead concentration was estimated as

$$C_b = \frac{N_{tot}}{S_d} \tag{5.2}$$

where S_d the predicted horizontal area that the beads covered at the time of sampling. We assumed that $S_d = S_{el}$, where $S_{el} = 4\pi\sigma_X\sigma_Y$ is the area covered by an ellipse having major and minor axis lengths equal to twice the cluster standard deviations (σ_X, σ_Y) along major and minor axes respectively. This formula assumes that the positions of the beads have a Gaussian distribution. It also assumes that the transport and eddy-diffusion of drogues are the same

as for beads. In a Gaussian distribution 88% of beads are located inside the above ellipse. Equation (5.2) only gives an order of magnitude of C_b since it assumes that the density of beads is homogeneous within the cluster ellipse (this is also the reason that we did not correct (5.2) for the fact that only 88% of the beads, and not all of them are inside the above mentioned ellipse).

The beads were sampled with a net tow. The sampling took place around nine positions on a rectangular grid (see Figure 5-1, where the nine positions are numbered from 1 to 9). The grid centre was located at the centre of the drogue cluster (position 5 in Figure 5-1). The positions were $l=3\,km$ apart. The sampling was done with our boat in a circle about each position. It would take about $t_b=600\,s$ to complete a sampling circle at a boat speed $u_b=2\,knots\approx 1\,m/s$. The mouth of the net had dimensions of $1\,m$ by $1\,m$. The area of the net's mouth was, therefore, $S_t=1\,m^2$. For the purpose of our calculations we can assume that the eggs are uniformly distributed over the top layer of the sea of width $d=1\,m$. The horizontal area S of the water sampled during a tow is then

$$S=\frac{0.7\,u_b t_b S_t}{d} \tag{5.3}$$

where the coefficient 0.7 accounts for the fact that 30% of beads was expected to go through the net's mesh. The cluster characteristics and values of N_p at the 24^{th} hour were calculated for the two of the four inshore experiments (7 December 1989, 2 November 1989). In the other two experiments we had trisponder failure. On 7 December $\sigma_X=1309$, $\sigma_Y=837$ which give $N_p=154$. Out of the nine tows of this experiment, one had $N=5$ beads, two other tows had $N=1$ bead and the remaining six tows had no beads. On 2 November $\sigma_X=1120$, $\sigma_Y=500$ which give $N_p=302$. Out of the nine tows of this experiment, two tows had $N=1$ bead, one tow had $N=2$ beads and the remaining six tows had no beads. In both experiments, N_p is two orders of magnitude larger than N. This probably happens because the different positions of the sampling grid were too far apart ($l=3km$), whereas our cluster is distributed over an area of only

$1km \times 0.5km$. This fact though, does not explain why also at the center of the cluster N was too small. Obviously, the centre of the cluster was not the same as the centre of the beads. This might be attributed to the effect of the wind on the part of the drogues above the sea surface. In section 2.2.1, page 32 in particular, we saw that the wind drag on the drifter part above the sea surface results in the drifter velocity being larger than the bead velocity by $\Delta u = \frac{0.4 \times w}{100}$, where w is the typical along-shore "O" wind, and that this effect is mostly in the along-shore direction, since both the wind and current tend to be along-shore. The drifters therefore will, over a time interval Δt, outdistance downstream the beads by $\Delta S = \Delta u \Delta t = \frac{0.4 \times w}{100} \Delta t$. For $\Delta t = 24h = 86400s$, i.e., the duration of the experiments, and for $w = 5m/s$, i.e., the "O" typical along-shore wind for either of the experiments, the above formula gives $\Delta S = 1700m$. This means that the center of the patch of beads, was approximately located $1700m$ upstream from the center of the cluster of drogues, around which the tow 5 was conducted, and also $1300m$ downstream from the position of tow 2, as can be seen in Figure 5-1. Assuming that the patch was distributed over along-shore and across-shore scales equal to $\sigma_X = 1000m$, and $\sigma_Y = 500m$ respectively, consistent with 66% of the beads being distributed over these scales in a Gaussian bead distribution, we expect that the majority of the beads (66%) were distributed in the elliptical area between tows 2 and 5, as can be seen in Figure 5-1. In the above speculations, which explain reasonably well the deviation of N_p from N, we did not consider the effect of vertical shear dispersion of the beads. In section 2.2.2 we saw that the vertical shear dispersion results in the horizontal diffusion rate of a patch of eggs or beads being generally larger than horizontal diffusion rate of a cluster of drogues, given that both beads and drogues have the same initial conditions of release. Our scale analysis showed that in our case, there is probably no significant difference between the diffusion rates of the drogues and the beads, because the apparent diffusivity K_{ex}, induced by the vertical shear diffusion, is negligible if compared with the along-shore eddy

diffusivity of the cluster diffusion $K_x^c = 8.9 m^2/s$. However, it was also shown that K_{ex} is very sensitive to uncertainties of the vertical eddy diffusivity K_z, and thus an increase of K_z by a factor of 4 (i.e., from $10 \times 10^{-4} m^2/s$, used in our scale calculations to $40 \times 10^{-4} m^2/s$) would result in K_{ex} being of the same order of magnitude as K_x^c. It is reasonable to assume such an increase of K_z for the area, since we do not have any data that would enable precise estimation of K_z, and the value of $K_z = 10 \times 10^{-4} m^2/s$ gives only an order of magnitude typical for shallow areas (Okubo, pers. comm.). A value therefore of $K_z = 40 \times 10^{-4} m^2/s$ would result in $K_{ex} = O(10 m^2/s)$. Such a value of K_{ex} would result in an along-shore bead dispersion X, after $T = 24h$ since release, of the order of $X = \sqrt{K_{ex} T} = \sqrt{10 \times 24 \times 3600} m \approx 900 m$. The beads would be distributed over an along-shore length scale that would be larger than the along-shore length scale of the the cluster by approximately $1 km$. Even if this would be the case, most of the beads would be located between the tows 2 and 5, in view of the fact that in a Gaussian distribution the concentration of particles falls very rapidly with the distance from the patch center (see equation (1.8)).

5.2. The coupled inshore/shelf-edge experiments

Each of the Fall 89 inshore experiments was coupled with a shelf-edge one, in order to enable comparison of the inshore kinematics with the shelf-edge kinematics. In one pair of experiments (30 October 89 - 2 November 89) both the inshore and the shelf edge clusters drifted westwards. In two pairs of experiments (23 October 89 - 26 October 89 and 30 November 89 - 4 December 89), reversals to the East happened during both the inshore and shelf edge experiments. Finally, in one of the pairs (7 December 89 - 11 December 89), the inshore cluster reversed its westwards course to the East but the the shelf edge cluster moved westwards throughout the experiment. Figures 5-2, 5-3 show the drifter trajectories of the four pairs of experiments. In these Figures the diamonds show the position of the first trisponder fix of the experiment.

Normally, the first trisponder fix of a drifter position was taken a little later after the release of the cluster of drifters. The diamonds therefore indicate fairly well the area of the release of the cluster as well. In some occasions however we had trisponder failure at the beginning of the experiment, and only a couple of hours later did the trisponder give a signal again. In this case the diamond does not indicate the area of the cluster release, but some area downstream of it, corresponding to the first recorded drifter position after the trisponder started working. A good example of this case is the inshore experiment of 26 October 89 in Figure 5-3. Only a small portion of only one drifter trajectory (out of the 10) could be plotted, since the trisponder malfunctioned for the biggest part of this experiment. The fact that an eastwards reversal happened at that day is based merely on the observations rather than on data. Speaking of trisponder malfunction, we see that the trajectories of the experiment at the 30^{th} November 1989, seem to partly fall on land. The calibration constants on which the triangulation algorithm is based, for calculating the x and y coordinates, were probably mistakenly changed by the trisponder operator during that experiment, and this might be the reason why the real trajectories are shifted towards the land. A reversal to the East was observed during that experiment too.

Whenever westwards drifter motion happened, during either the inshore or the shelf edge experiments, the wind was strong westwards (typically $5 m/s$). Inshore or shelf edge eastwards drifter motion only happened during periods of very light winds (less than $2 m/s$). The hypothesis of a westwards wind stress and an opposing eastwards pressure gradient, as described in section 3.4, seems to be valid at the shelf edge too.

Figure 5-1: *The method of the beads sampling. The tows were conducted with a boat in circles around the positions 1 to 9. The X indicate positions of the 10 drifters. The ellipse indicates the area within which 66% of the beads would be located, assuming they followed a Gaussian distribution.*

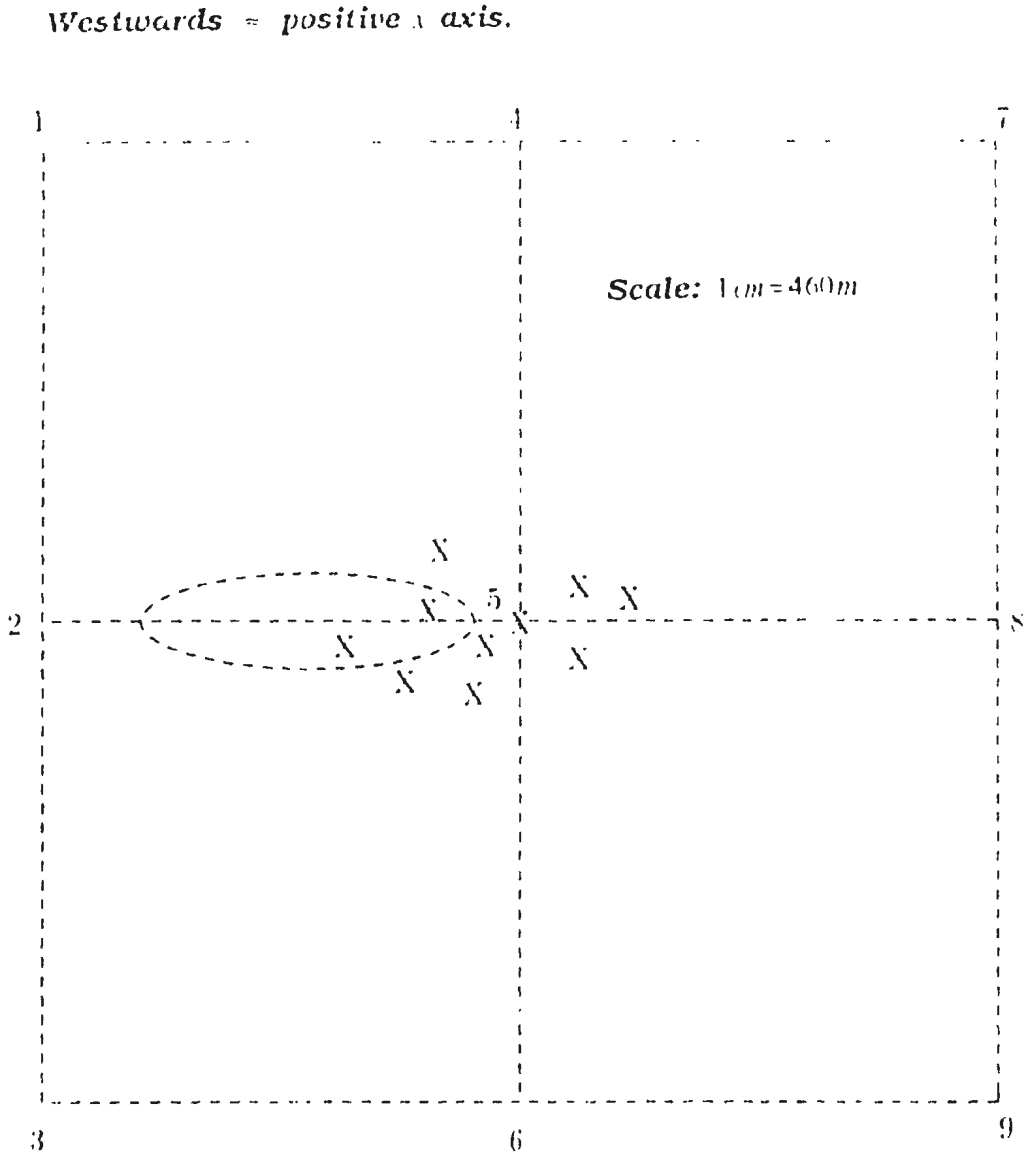

Figure 5-2: *The drifter trajectories of the coupled inshore/shelf-edge experiments, part I. Diamonds indicate positions of first trisponder fix, i.e., drifter release sites (approximately). The coast and the coral reefs are shaded. The positive x axis points towards the East (approximately), and the positive y axis points towards the North (approximately).*

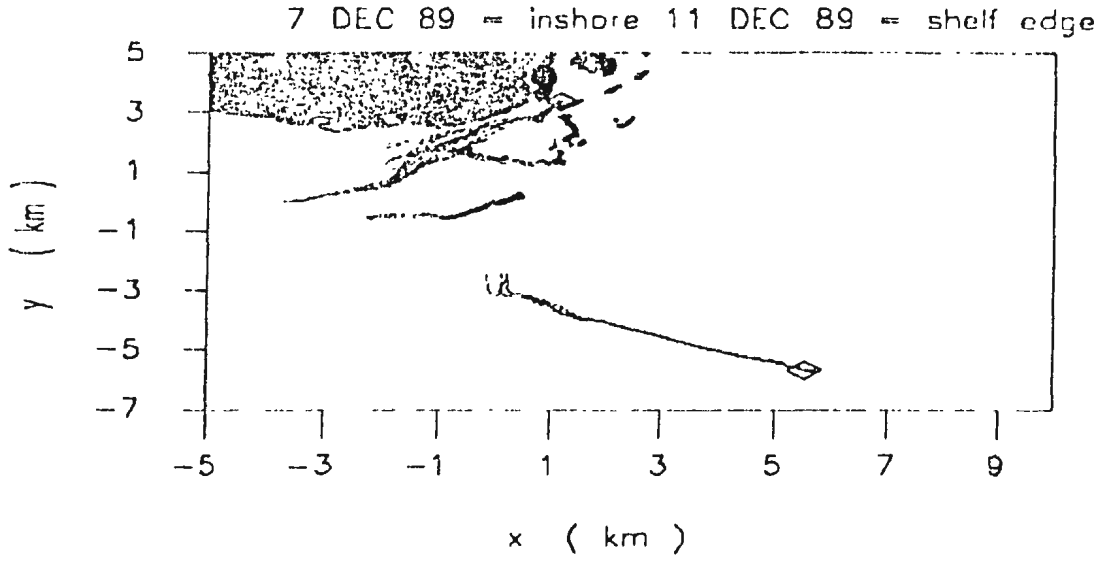

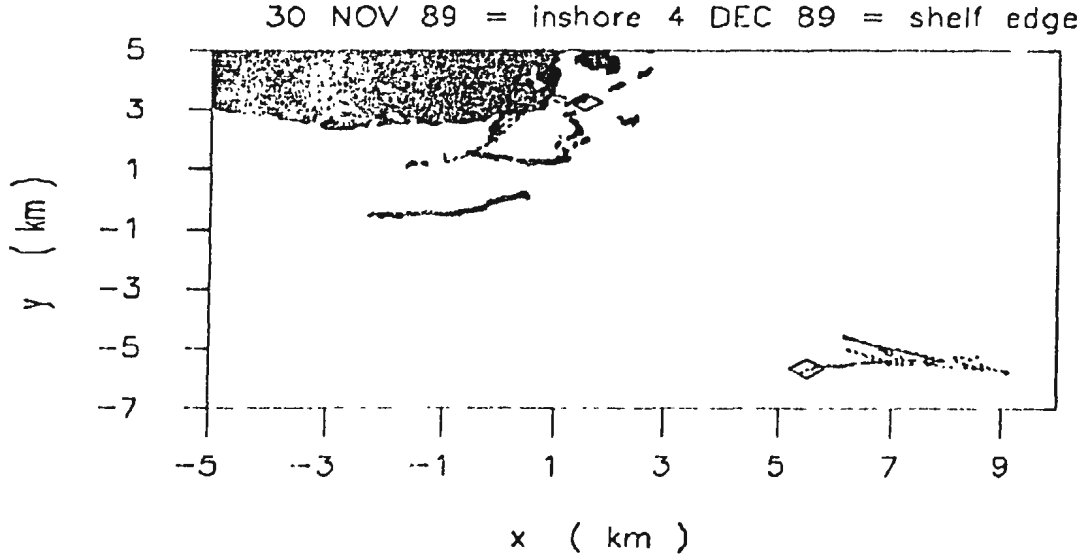

Figure 5-3: *The drifter trajectories of the coupled inshore/shelf-edge experiments, part II. Diamonds indicate positions of first trisponder fix, i.e., drifter release sites (approximately). The coast and the coral reefs are shaded. The positive x axis points towards the East (approximately), and the positive y axis points towards the North (approximately).*

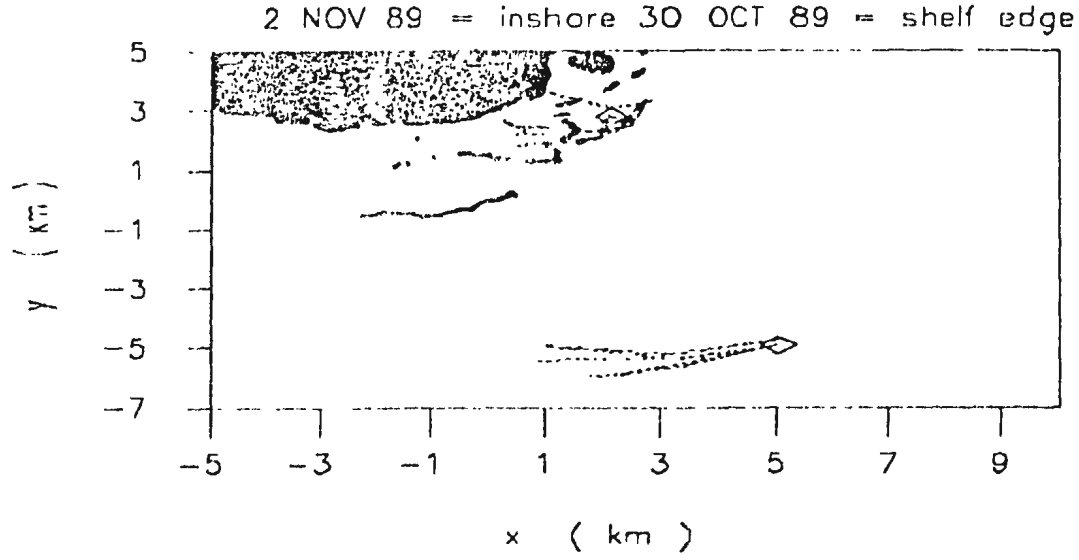

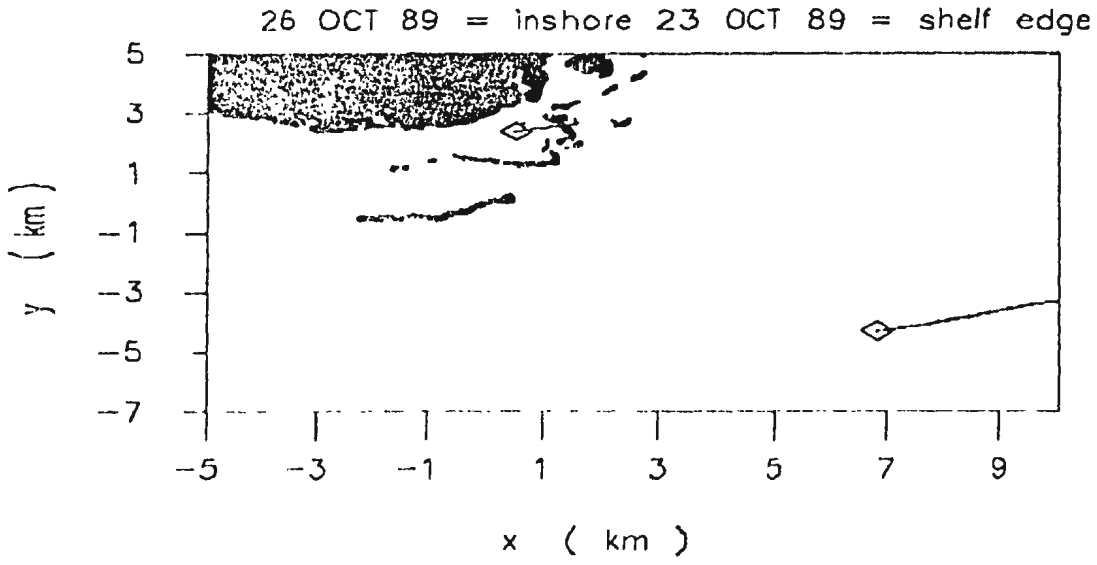

Chapter 6

Conclusions

The drifter tracking experiments on the Southwestern Puerto Rican shelf were conducted to investigate the dependence of the transport and diffusion of a cluster on the initial conditions of the cluster release. This information is needed to understand the spawning strategy of coral-reef fish. We were also interested in the dynamical processes that drive the flow in the area of the experiment.

The area of the experiments is shallow ($5-10m$). The wind tends to blow along shore in a westwards direction and drives an along-shore (westwards) current as is evident by the high along-shore wind current correlation. This correlation is highest at lags $\tau=0h$ to $\tau=3h$, in accordance with the predictions of a one-dimensional along-shore model for the response of the wind to the current. The predominant tides in the area are the diurnal and the semidiurnal. The diurnal tide has an amplitude of $10cm$ and can be modelled as an across-shelf standing wave forced at the shelf edge. The associated across-shore diurnal tidal velocity is one order of magnitude smaller than the across-shore component of the typical currents in the area. The semidiurnal tide has an amplitude of $1cm$ and can also be modelled as an across-shelf progressive wave. The associated across-shelf semidiurnal velocity amplitude is much smaller than the across-shore component of the typical currents. When the wind pauses, flow reversals to the East have been observed, and the maximum observed eastwards velocity is $10cm/s$. We hypothesized that the reversals might be caused by a pressure gradient opposing the wind. To examine the validity of this assumption we assumed that the along-shore steady state can

be described by a balance between the wind stress, the bottom stress and the pressure gradient. Linear regression of the wind stress versus the bottom stress revealed that the pressure gradient should point eastwards and have an approximate magnitude of $0.01 Pa$. Such a pressure gradient would drive an eastwards flow of about $10 cm/s$, in accordance with the measured maximum eastwards current.

The single particle statistics of the drifter trajectories revealed that the flow variability is mostly in the along-shore direction. This happens because in the along-shore direction the currents fluctuate with the winds. The large scale on/offshore flow variability is restricted by the coastal boundary. The on/offshore single particle velocity residual decorrelates after $1 h$, so that for time scales much larger than one hour, the evolution of the velocity residual can be described by a random walk model and the eddy dispersion can be described by the classical diffusion equation. The along-shore single particle velocity residual has a larger decorrelation time ($2.5 h$) since it fluctuates with the winds. The variance grows proportional to time raised to the power of 1.5. Thus the along-shore dispersion is faster than a random walk (or Fickian diffusion) and can be modelled as fractional Brownian motion. We also found that, the mean flow during the dry season is greater than the mean flow during the wet season. The single particle dispersion during the wet season is greater than the single particle dispersion during the dry season. Single particle statistics of the ensemble of the drifter trajectories released at the spawning time were compared with the nonspawning time single particle statistics. The nonspawning time deployment results in trajectories that, on the average, go closer to the shore and have slightly larger variability than the drifter trajectories deployed at spawning time. Eggs released at nonspawning time would, therefore, be subject to more predation. The release site (spawning / nonspawning site) does not affect the mean trajectory and single particle dispersion. This can partially be explained by the fact that the drifter release

positions corresponding to different initial conditions of dye release, are generally not statistically different from each other.

The cluster statistics of the drifter data revealed that a cluster of drifters is elongated at all the times, in a direction parallel to the coast. The cluster elongation is approximately constant during the experiment, and can be ascribed to a strong along-shore shearing of the mean flow at the first $1.5h$ of the cluster trajectory. This along-shore shearing interacts with the across-shore eddy diffusion ("shear dispersion"), and as result the cluster elongates rapidly (scale calculations also showed that the along-shore shearing would result in rapid along-shore elongation even in the absence of eddy diffusion). Subsequently the shearing becomes weak and the cluster does not elongate anymore. The cluster dispersion does not grow continuously with time but it is Fickian on average. The across-shore variance of the drifter position relative to the cluster centroid alternatively increases and decreases with time. The fact that the cluster diffusion diffusivities are factors of 7 and 2 smaller than the single particle diffusivities for the x and y components of dispersion, indicates that there is more variability in the paths of the clusters than in the paths of the drifters within a cluster. The dependence of the single particle statistics on the site / time and season of drifter release is therefore much more important than the dependence of the cluster statistics on the above initial conditions. Nevertheless, we compared the cluster statistics of the various drifter ensembles (spawning time and site / nonspawning time and site ensembles, wet / dry season ensembles). We found that the along-shore cluster dispersion in the dry season is greater than in the wet season. The wet season ensemble has greater across-shore variance than the dry season. Also we found that the cluster dispersion is higher for the ensemble of clusters that were deployed at spawning time / sites as opposed to the ensemble of the clusters that were deployed at nonspawning time / sites.

Finally, the cluster averaged distinctness was calculated as function of time since release. The distinctness quantifies the separation between two clusters that were synchronously released in an experiment. We found that the cluster of drifters released at a spawning site remains separate from the cluster released at a nearby nonspawning site ($400m$ apart), for at least the first $15\,h$ after release. Although clusters released from spawning/nonspawning sites remain separate in a particular day, and for the largest portion of the experiment, the mean trajectories corresponding to the two sites are not statistically different as was shown by the single particle statistics. This contradiction between the spawning and nonspawning site trajectories remaining separate on a particular experiment on the one hand, and the mean trajectories corresponding to the spawning and nonspawning sites not being distinct on the other hand, can be attributed to the large flow variability from experiment to experiment. In the wet season the two clusters remain further apart than in the dry season. If the clusters are released at a spawning time, they also remain farther apart as compared to clusters released at a nonspawning time.

The diffusion and transport of the eggs is not exactly the same as the diffusion and transport of the drifters. The shear at the top layer of the water interacts with the vertical eddy diffusion, resulting in the egg diffusion being larger (vertical shear diffusion effect) as compared to the cluster diffusion. Scale analysis showed that the apparent diffusivity K, induced by the vertical shear effect, is one order of magnitude less than the cluster diffusivity. However, this does not necessarily lead to the conclusion that the vertical shear diffusion of the eggs is negligible as opposed to the cluster diffusion, since it is also evident from our scale analysis that K is very sensitive to uncertainties of the vertical turbulent diffusivity K_z, the buoyancy velocity w_b, and the vertical shear of the horizontal flow velocity Ω, according to the equation $K = \frac{\Omega^2 K_z^3}{w_b^4}$. For example,

an increase in K_x by a factor of 4 results in K being of the same order of magnitude as the cluster diffusivity. Finally, the wind drag on the part of the drifters above the sea surface was shown to result in the currents of the area being overestimated by 18%, so that the drifters would slightly outdistance the eggs downstream.

In the Fall 1989 experiments, we sought to compare drifter trajectories released at shelf-edge spawning sites with drifter trajectories released at inshore (San Cristobal reef) spawning sites. It seems that the hypothesis of a balance between the wind stress, the bottom stress and an opposing alongshore pressure gradient in the steady state is also valid at the shelf edge. We also compared the transport-diffusion of clusters of drifters with the transport-diffusion of patches of beads matching the size and buoyancy of fish eggs, by releasing both the beads and the drifters at the same site and time. The measured bead distribution could not be predicted by the drifter distribution, probably because the drifters outdistanced the beads, due to the effect of the wind on the part of the drifters above the sea surface.

Chapter 7

Bibliography

Amorocho, J., and J. J. Devries. 1980. A new evaluation of the wind stress coefficient over water surfaces. *J. Geophys. Res.* 85: 433 - 442.

Baker, L. G., and J. Gollub. 1990. Chaotic Dynamics. An Introduction. Cambridge University press, 180 pp.

Beauchamp, K., and C. Yuen. 1979. Digital Methods for Signal Analysis. GEORGE ALLEN & UNWIN LTD, 316 pp.

Bowden, K. F. 1965. Horizontal mixing in the sea due to a shearing current. *J. Fluid Mechanics.* 21: 83-95.

Csanady, G. T. 1973. Turbulent Diffusion in the Environment. D. Reidel publishing company, 248 pp.

Csanady, G. T. 1982. Circulation in the Coastal Ocean. D. Reidel Publishing Company. 279 pp.

Fancher, J.E. 1971. M.Sc Thesis. Seasonal Changes of Sea Level of the Caribbean as Examined at a Single Station. Department of Marine Sciences, Univ. of Puerto Rico Mayaguez. 55 pp.

Giese, G. S.; Hollander, R. B.; J. E. Fancher, and B. S. Giese. 1982. Evidence of coastal seiche excitation by tide generated internal solitary waves. *Geophysical Research Letters.* 9: 1305 - 1308.

Gill, A. 1982. Atmosphere Ocean Dynamics. Academic Press, Inc. 662 pp.

Hoerner, S. F. 1958. Fluid Dynamic Drag. 2nd Ed. Midland Park, N.Y. 610 pp.

Kirwan, A. D.: Mcnally G.; Chang, M. S, and R. Molinary. 1975. The Effect of Wind and Surface Currents on Drifters. *J. Phys. Oceanogr.* 5: 361 -369.

Kjerfve, B. 1981. Tides of the Carribbean Sea. *J. Geoph. Res.* 86: c5: 4243 - 4247.

Large, W. G., and S. Pond. 1981. Ocean Momentum Flux Measurements in Moderate to Strong Winds. *J. Phys. Oceanogr.* 11: 324 - 336.

Mandelbrot, B. B., and Van Ness, J. W. 1968. Fractional Brownian motions, fractional noises and applications. SIAM review. 10: 422 - 437.

Monin, A. S., and Yaglom, A. M., 1975. Statistical Fluid Mechanics II. The MIT Press. 872 pp.

Okubo, A. 1962. A Review of Theoretical Models for Turbulent Diffusion in the Sea. *J. Oceanogr. Soc. Japan.* 20th Anniversary Volume: 286 - 320.

Okubo, A. 1966. A Note on Horizontal Diffusion from an Instantaneous Source in a Nonuniform Flow. *J. Oceanogr. Soc. Japan.* 22: 2: 35 - 40.

Okubo, A. 1971. Oceanic Diffusion diagrams. *Deep Sea Res.* 18: 789 - 802.

Okubo, A., and C. C Ebbesmeyer. 1976. Determination of vorticity, divergence and deformation rates from analysis of drogue observations. *Deep Sea Res.* 23: 349 - 352.

Reynolds, O. 1895. On the dynamical theory of incompressible viscous fluids and the determination of the criterion. *Phil. Trans. Roy. Soc. London.* A186: 123

Richardson, L. F. 1926. Atmospheric diffusion shown on a distance neighbour graph. *Proc. Roy. Soc. London.* A110: 709

Sanderson, B. G., and A. Okubo. 1987. Comments on the "Shear Effect" and Diffusion in the Lagrangian Framework. *J. Oceanogr. Soc. Japan.* 43: 183 - 196

Sanderson, B. G., and D. A Booth. 1991. The fractal dimension of drifter trajectories and estimates of horizontal eddy diffusivity. *Tellus.* A43: 334 - 349.

Saucier, W., J. 1953. Horizontal deformation in atmospheric motion. *Transactions, American Geophysical Union.* 34:45 709 - 719.

Shapiro, D. Y.; D. A. Hensley and R. S. Appeldorn. 1988. Pelagic spawning and egg transport in coral-reef fishes: a skeptical overview. *Environmental Biology of Fishes.* 22:1: 3 - 14.

Stommel, H. 1948. Horizontal diffusion due to oceanic turbulence. *J. Mar. Res.* 8:199.

Taylor, G. I. 1922. Diffusion by continuous movements. Proc. London Math. Soc. A20:196

Tennekes, H. and J. L. Lumley. 1972. *A First Course in Turbulence.* The Massachusetts Institute of Technology Press, 300 pp.

Tyler, R. 1992. M.Sc Thesis. The Wind-Driven Pressure and Flow Fields around a Cylindrical Island in a 1.5-Layer Ocean: Comparison with Observations from the Island of Puerto Rico. Department of Marine Sciences, Univ. of Puerto Rico Mayaguez. 208 pp.

Vachon, W. 1975. Understanding drogue performance by instrumental tests. *Exposure, (a newsletter for Technologists).* 2, No. 6) Zimmerman, J. T. F. 1978. On the Euler-Lagrange transformation and the Stokes' drift in the presence of oscillatory and residual currents. *Deep-Sea Res.* 26A: 505 - 520.